

Image-Based Feature Tracking Algorithms for Real-Time Clad Height Detection in Laser Cladding

by

Mehrdad Iravani-Tabrizipour

A thesis
presented to the University of Waterloo
in fulfillment of the
thesis requirement for the degree of
Master of Applied Science
in
Mechanical Engineering

Waterloo, Ontario, Canada 2007

©Mehrdad Iravani-Tabrizipour, 2007

**AUTHOR'S DECLARATION FOR ELECTRONIC SUBMISSION OF A
THESIS**

I hereby declare that I am the sole author of this thesis. This is a true copy of the thesis, including any required final revisions, as accepted by my examiners.

I understand that my thesis may be made electronically available to the public.

Mehrdad Iravani-Tabrizipour

Abstract

In laser cladding, a material, usually in the form of powder, is deposited on a substrate. Powder particles are intermingled with inert gas and fed by a powder feeder system on the substrate. Laser is employed to melt the additive material and a small layer of surface of the substrate simultaneously. While the powder is being deposited, the laser melts the powder particles and the melted powder particles join the melt pool on the substrate beneath the laser beam. Generating relative motion between the laser focal point and the substrate will result in moving melt pool on the substrate. This will lead to addition of a desired material to the substrate with desired thickness and good bonding as well as minimum dilution. In addition, by producing clads beside and on the top of each other a functional component can be built in a layer by layer fashion.

Despite many advantages of laser cladding, it is highly sensitive to internal and external disturbances. This makes a closed-loop control system for laser cladding inevitable. Utilizing a closed-loop control system in laser cladding makes the system insensitive to external and internal disturbances. Having a closed-loop control system for laser cladding would contribute to substantial improvement in clad quality and cost reduction. Feedback sensor is an essential part in a closed-loop control system. Among different parameters that can be used as feedback signals in a closed-loop control of laser cladding, melt pool geometry and in particular clad height is of great importance specifically for the purpose of rapid prototyping.

This thesis presents novel algorithms for real-time detection of clad height in laser cladding. This is accomplished by the following:

Tackling the issues pertinent to image acquisition in the presence of harsh and intensive light is scrutinized. Important parameters of digital cameras related to selection of proper type of CCD cameras in order to overcome the existent harsh condition are presented. Also, the existent light in laser cladding arisen from different sources is analyzed and based upon that proper bandpass filters and neutral filters are selected. All these lead to capture relatively sharp and clear images of the melt pool. Capturing good quality pictures potentially would provide valuable information about the process. This information could include, but is not limited to, melt pool geometry (i.e., melt pool height, width, melt

pool profile, and wet angle), angle of solidification, melt pool temperature, and melt pool temperature distribution. Furthermore, the issues regarding path dependency of the melt pool image are addressed by using a trinocular cameras configuration. By utilizing this, always two cameras monitor the front end of the melt pool regardless of the direction of the clad.

Image analysis of the grabbed images is also discussed. Image thresholding is one of the most formidable tasks in image processing and this difficulty is intensified due to characteristics of the grabbed images of the melt pool (e.g., surrounding hazy area around the melt pool). Applying hard partitioning thresholding method did not lead to detection of the melt pool accurately. As a result, fuzzy thresholding by minimizing of the measure of fuzziness is developed and its performance is investigated. The effect of three important membership functions, triangular, Gaussian, and generalized Bell on the performance of the thresholding method is investigated. Also, Image thresholding by utilizing fuzzy c-means clustering is developed. Applying the developed thresholding methods show promising results. Among the developed thresholding methods, fuzzy thresholding with minimizing the measure of fuzziness with Gaussian membership function is selected for the implementation in the algorithm.

Finally, Image feature tracking module is presented. The detected borders of the melt pool images are transformed from image plane to the world plane by using a perspective transformation. Four features of the elliptical features of the projected melt pool borders are selected. These four features along with the angle of tangential path vector with respect to the corresponding right hand side camera's axis are fed into an Elman recurrent neural network. The proposed algorithms and the trained neural network are utilized in the process resulting in acceptable detection of the clad height in deposition of straight clads for a specific direction. It is concluded that the system can detect the clad height with about ± 0.15 mm maximum error.

Acknowledgments

I would like to thank my supervisor professor Toyserkani who with great energy and devotion led me during the last two years. Special thanks to professor Khajepour whom this would have not been accomplished without his support. Also, I want to thank my colleague, Matthew Asselin, who was a source of help and constructive suggestions. I also benefited from help and support of my other colleagues, including but not limited to: Christ P. Paul, Jeff MacIsaac, Masoud Alimardani, Alireza Fathi, and Hamidreza Alemohammad. Last but not least, I would like to dedicate this thesis to my parents who taught me how to live.

Contents

| | | |
|----------|--|-----------|
| 1 | Introduction | 1 |
| 1.1 | Laser | 1 |
| 1.2 | Laser Cladding | 3 |
| 1.3 | Laser Cladding Configuration | 6 |
| 1.4 | Laser Cladding Parameters | 7 |
| 1.5 | Objective Statement | 11 |
| 1.6 | Looking Ahead | 11 |
| 2 | Literature Review and Background | 13 |
| 2.1 | Laser Cladding | 13 |
| 2.2 | Control of Laser Cladding | 14 |
| 2.2.1 | Powder Feed-Rate as a Feedback Signal | 15 |
| 2.2.2 | Melt Pool Temperature as a Feedback | 17 |
| 2.2.3 | Melt Pool Geometry as a Feedback | 18 |
| 2.3 | Conclusion | 26 |
| 3 | Experimental Setup | 28 |
| 3.1 | Introduction | 28 |
| 3.2 | Experimental Setup | 28 |
| 3.3 | Image Acquisition Device | 31 |
| 3.4 | Filter Selection | 37 |
| 3.4.1 | Spectral Response (Quantum Efficiency) | 37 |

| | | |
|----------|---|-----------|
| 3.4.2 | Black Body Radiation | 38 |
| 3.5 | Trinocular cameras | 39 |
| 4 | Image Processing | 43 |
| 4.1 | Introduction | 43 |
| 4.2 | Image Thresholding | 44 |
| 4.3 | Application of Fuzzy Set Theory to Image Thresholding | 52 |
| 4.4 | Determination of Optimal Threshold by Minimizing the Measure of Fuzziness | 52 |
| 4.4.1 | Entropy | 54 |
| 4.4.2 | Membership Distribution Using Gaussian Membership Function . . | 56 |
| 4.4.3 | Membership Distribution Using Generalized Bell Membership Function | 58 |
| 4.4.4 | Employment of Look Up Table | 61 |
| 4.5 | Determination of Optimal Threshold by Fuzzy C-Means Clustering | 62 |
| 4.5.1 | Fuzzy C-Means Clustering (FCM) | 64 |
| 4.5.2 | Computation of Optimal Threshold by FCM | 65 |
| 4.6 | Results and Discussion | 67 |
| 5 | Feature Tracking Algorithms | 74 |
| 5.1 | Image Transformation | 74 |
| 5.2 | Image Feature Tracking Module | 78 |
| 5.2.1 | Extracting the ellipse major and minor diameters and α from the projected borders | 78 |
| 5.2.2 | Features Selection | 81 |
| 5.3 | Recurrent Neural Network | 83 |
| 5.4 | Experimental Verification | 84 |
| 5.4.1 | Training and Simulation of RNN | 88 |
| 5.4.2 | Verification of RNN and Discussion | 88 |
| 6 | Conclusion and Recommendations | 90 |
| 6.1 | Conclusion | 90 |
| 6.2 | Recommendations | 93 |

List of Tables

| | | |
|-----|--|----|
| 1.1 | TIG versus Laser Cladding [1] | 6 |
| 1.2 | Types of lasers utilized in laser cladding and their specification [2] | 9 |
| 3.1 | Specification of exploited cameras | 36 |
| 5.1 | Specification of the conducted tests | 86 |

List of Figures

| | | |
|-----|--|----|
| 1.1 | Some laser applications [1] | 2 |
| 1.2 | Schematic view of laser cladding | 4 |
| 1.3 | Laser cladding: Moving head by robot and moving substrate along with coaxial nozzle | 8 |
| 1.4 | Clad geometry | 10 |
| 2.1 | Schematic view of developed sensor for powder feed rate adapted from Hu and Kovacevic [9] | 16 |
| 2.2 | Schematic view of developed sensor for melt pool size [9] | 19 |
| 2.3 | Schematic view of triangulation sensor | 21 |
| 2.4 | Utilizing CMOS camera for monitoring of processing zone in laser beam welding adapted from [31, 32, 33, 34] | 24 |
| 2.5 | Melt pool visualization in laser welding adapted from [42] | 26 |
| 3.1 | Schematic view of the laser cladding system at the University of Waterloo . | 29 |
| 3.2 | UW Powder feeder | 30 |
| 3.3 | 4 axes CNC table used in the laser cladding | 31 |
| 3.4 | Lateral nozzle and laser head | 32 |
| 3.5 | a) Coaxial nozzle designed at UW b) Powder stream from the coaxial nozzle when the carrying gas is at 5 SCFH, powder feedrate is 1.5 g/min, and 3 SCFH shaping gas | 32 |
| 3.6 | a) An image of the melt pool, b) An image of the melt pool when the CCD sensor saturated | 35 |

| | | |
|------|--|----|
| 3.7 | Spectral response of UNIQ UP-600CL extracted from manufacturer's manual | 38 |
| 3.8 | Planck's law: black body radiation | 40 |
| 3.9 | Tangential path vector's direction changes during a sinusoidal path and it places in different regions generated by trinocular cameras | 41 |
| 3.10 | Trinocular cameras installed on the system | 42 |
| 4.1 | Typical types of images taken from the melt pool (part 1). a) & b) melt pool images. c) & d) corresponding surface plots of the images. e) & f) corresponding histograms along with the related statistical data of the images | 46 |
| 4.2 | Typical types of images taken from the melt pool (part 2). a) & b) melt pool images. c) & d) corresponding surface plots of the images. e) & f) corresponding histograms along with the related statistical data of the images | 47 |
| 4.3 | Typical types of images taken from the melt pool (part 3). a) & b) melt pool images. c) & d) corresponding surface plots of the images. e) & f) corresponding histograms along with the related statistical data of the images | 48 |
| 4.4 | Thresholded image by applying Otsu method : Only the flare has been detected, and the melt pool completely eliminated. | 51 |
| 4.5 | Membership distribution in typical image using triangular membership . . | 55 |
| 4.6 | Applying minimizing the measure of fuzziness with triangular membership function to an image | 56 |
| 4.7 | Membership distribution in a typical histogram using Gaussian membership | 57 |
| 4.8 | Applying minimizing the measure of fuzziness with Gaussian membership function to an image | 58 |
| 4.9 | Membership distribution using generalized bell curve membership function | 60 |
| 4.10 | Applying minimizing the measure of fuzziness with generalized bell membership function to an image | 60 |
| 4.11 | Membership distributions in a histogram by applying FCM method | 68 |
| 4.12 | Application of FCM thresholding to one image | 68 |
| 4.13 | A comparison of threshold levels obtained through the aforementioned algorithms for 100 of the aquired images during the experiments | 69 |

| | | |
|------|--|----|
| 4.14 | Obtained thresholded images through the aforementioned algorithms for 5 images selected through many images as a sample (first part). Circled results show the better outputs among the four results. | 71 |
| 4.15 | Obtained thresholded images through the aforementioned algorithms for 5 images selected through many images as a sample (second part). Circled results show the better outputs among the four results. | 72 |
| 5.1 | Perspective transformation: transformation of coordinates from the image plane to the world plane | 75 |
| 5.2 | Typical projected images on the reference plane: a) Typical images from camera 1 and 2, b) Binarized images, c) Detected border of the melt in each image, d)The projected melt pool border images on the work plane | 77 |
| 5.3 | A schematic view of projection of the melt pool on the reference plane . . . | 78 |
| 5.4 | Selected features in the images after fitting ellipses | 79 |
| 5.5 | Typical projected meltpool borders for different angles of the tangential path vector | 82 |
| 5.6 | Input and the output of the recurrent neural network | 83 |
| 5.7 | Structure of the selected Elman neural network adapted from Neural Network Toolbox of Matlab | 84 |
| 5.8 | Top view of direction of conducted tests for collecting data | 85 |
| 5.9 | Offline picture of the clad track of test 7 | 86 |
| 5.10 | Deviation of elliptical features during the test 3 | 87 |
| 5.11 | Clad height predicted by model versus real height for $\theta = 60^0$ | 89 |
| 6.1 | A Pattern recognition algorithm | 91 |

Chapter 1

Introduction

1.1 Laser

The invention of the laser, which stands for light amplification by stimulated emission of radiation, in 1958 with the publication of the scientific paper, Infrared and Optical Masers, by Arthur L. Schawlow and Charles H. Townes opened a new door to science. Lasers have multibillion markets and are vastly used in different applications such as Manufacturing, Measurement Techniques, Traffic, Education and Entertainment, Energy and Environment, Communication, Trade and Industry and Medicine. Our modern life does not seem feasible without lasers nowadays. Introduction of lasers has created many applications as shown in Figure 1.1 [1].

In manufacturing, huge amount of effort has taken place in order to integrate lasers. Nowadays lasers are used in welding, cutting, drilling and various surface treatments of metals and alloys, plastics, ceramics, composites, wood, glass and rubber. Aerospace, automotive, marine, rail are only a few examples that laser largely is being used. Utilizing lasers in manufacturing leads to production of components with better dimensional accuracy and surface quality compare to those which have been produced with conventional methods. Exploiting of laser as a manufacturing method has many advantages over conventional manufacturing methods [1]:

- Lasers can be employed as a high precision machine tool for cutting, welding surface

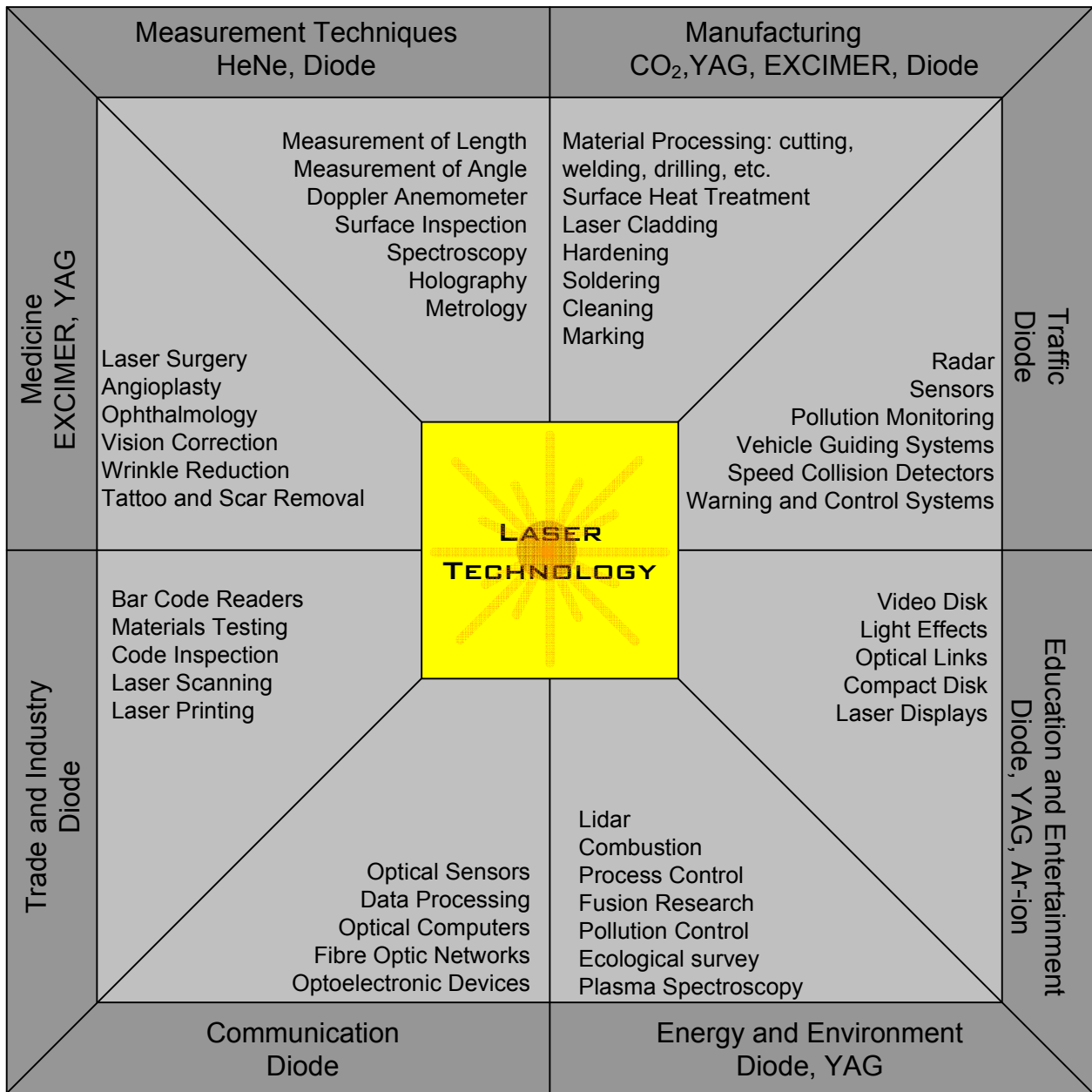


Figure 1.1: Some laser applications [1]

treatment and host of other material processing applications.

- Complex component shapes can be treated.
- Remote non-contact processing is usually possible.
- It does not have to work in a vacuum area, unlike electron beam heaters, Physical Vapour Deposition (PVD), ion implantation or plating.
- Treatment can be localised to a small area.
- Treatment of inaccessible areas of components by fibres or mirrors.
- Treatments are rapid.

Among the applications, lasers have shown promising results in the area of laser material processing. One of the techniques which has been widely used by industry is laser cladding which receives benefits from unique features of the emitted laser light.

1.2 Laser Cladding

In laser cladding, a material usually in form of powder is deposited on a substrate. Powder particles are intermingled with inert gas and fed by a powder feeder system on the substrate. Laser is employed to melt the additive material and a small layer of surface of the substrate simultaneously. While the powder is being deposited, the laser heats the powder particles and the heated powder particles join the melt pool on the substrate beneath the laser beam. Generating relative motion between the laser focal point and the substrate will result in moving melt pool on the substrate. This will lead to addition of a desired material to the substrate with desired thickness and good bonding and the same time with the minimum dilution. In addition, by producing clads beside and on the top of each other a functional component can be made in a layer by layer fashion. Figure 1.2 shows schematic view of laser cladding. Thickness of a clad is ranging from 0.1 to 2 mm.

Additive material will be deposited by various approaches. The method (laser cladding by powder injection) which was elucidated earlier is more common and in this thesis laser

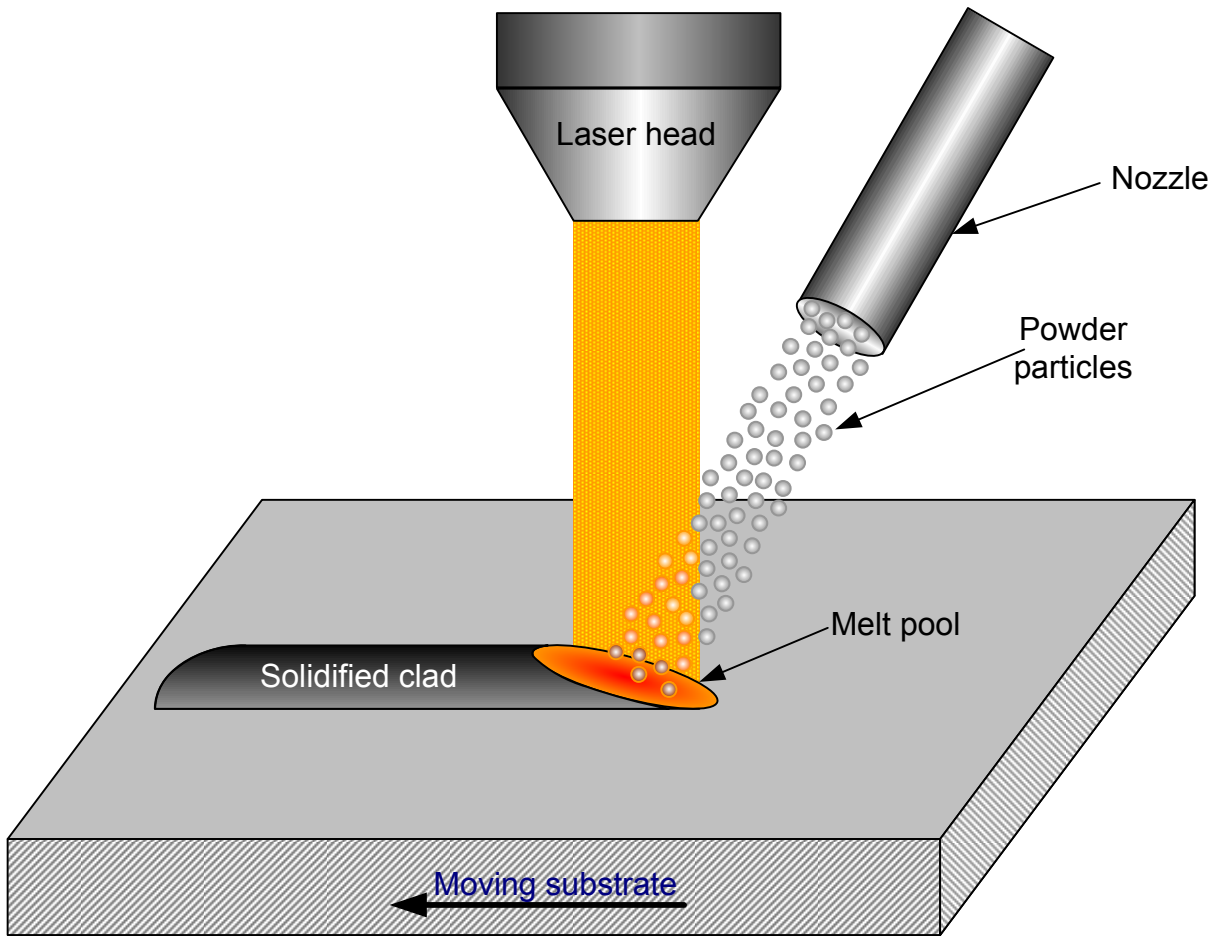


Figure 1.2: Schematic view of laser cladding

cladding refers to this method unless otherwise stated. The additive material can be deposited in form of paste (Laser cladding by Paste) or in form of wire (laser cladding by wire feeding). In the other approach which usually named two-step laser cladding the material powder is preplaced on the substrate and then laser is utilized to melt the additive material and the surface of the substrate.

In laser cladding, one part can be made from 3D CAD model. Hence, laser cladding is considered as an effective way of Rapid Prototyping. A 3D CAD model created by one of various CAD soft wares is exploited to build a part layer by layer. Production of a mechanical component in a layer-by-layer fashion allows industry to fabricate a part with features that may be unique to the laser cladding technique. These features include a homogeneous structure, enhanced mechanical properties, deposition of multiple materials, making heterogeneous materials and production of complex geometries. Due to having these features, the technology has been considered to be one of the potential manufacturing techniques in 21st century.

Laser cladding is a versatile technology which has been exploited in manufacturing, part repair, rapid prototyping of functional components (RP), rapid tooling (RT), and coating for a decade [2]. This is just the tip of the iceberg and this technology is permeating into vast range of applications. Laser cladding has been employed for coating which leads to conserve expensive materials by coating surface of bulk materials with enhanced wear or corrosion resistant materials such as superalloys, tool steel, Ni-base alloys and Co-base alloys. This will increase lifespan of a component by several times only by covering exterior surface which is subject to hostile conditions. Exploiting TIG welding or plasma spaying instead, would distort the component because of excessive heat. Moreover cooling rate during laser cladding is more rapid and this enhances mechanical properties of the component. In part repair, laser cladding has many applications such as repair of turbine blades [1]. Turbine blades are produced of superalloys which are expensive. Repairing these parts by conventional methods (e.g., by welding) is subject to thermal distortion and residual stress accumulation. Employing of laser cladding for this task will result in decrease the dependency of process on expert manpower, lessen of post processing and enhance the mechanical properties by improving microstructure. All these factors in return

Table 1.1: TIG versus Laser Cladding [1]

| | TIG | Laser |
|------------------------|---|--|
| Dilution Rate | Approx. 10-40% | Less than 5% |
| Use of Filler Material | More and non-uniform deposition | Less and uniform deposition |
| Hardness Value | Relatively low | Relatively high |
| Heat effected zone | Large and wide | Low and narrow |
| Finish | Rough surface, less durable | Good surface, long life |
| Pre and Post Treatment | Many | Few |
| Dendritic Structure | Course | Fine |
| Automation | Difficult, low production rate hence costly | Easy, high production rate, cost effective |

will lead to save in cost and time drastically.

Laser cladding has many advantages over conventional techniques in its applications. Table 1.1 compares laser cladding to TIG welding as an example [1].

As it is apparent in Table 1.1, laser cladding offers enhancing mechanical properties and microstructure of component due to high and controllable cooling rate, low and narrow heat effected zone and low dilution.

1.3 Laser Cladding Configuration

Laser cladding process comprises, laser, computer-aided design (CAD), robotics, sensors, control, and powder metallurgy. The central processing unit communicate with all involved elements in order to make the system fully automated. Various configurations have been arranged for laser cladding process based on these features:

Laser: Among different types of lasers CO₂, lamp-pumped Nd:YAG, diode-pumped Nd:YAG, and high power diode lasers (HPDL) are widely utilized in laser cladding process. Table 1.2 shows specifications of these lasers [2]. Selecting the proper type of laser highly depends upon the type of the application. Pulsed and continuous wave lasers are applicable in laser cladding, although for pulsed lasers, the peak power of each

pulse should not surpass a specific value otherwise it results in vaporization of the powder particles before reaching the process zone.

Powder feeder: There are several different powder feeders utilized in laser cladding by powder injection process. The powder feeders used in laser cladding, can be categorized into: fluidized-bed, gravity-based, and wheel-based metering feeder.

Powder nozzle: Some configurations employ lateral nozzles as opposed to others which they exploit co-axial nozzle. Coaxial nozzle has the advantage of being independent of direction of motion, however wasted powder which means the powder is not absorbed to the melt pool is higher than lateral nozzle.

Motion: Various configurations have been designed for generation of relative motion between the substrate and the laser head. In some configurations the laser head is stationary and the substrate moves by a multi-axis CNC machine. In others, the substrate is stationary and the laser head and powder feeder system is moving by a robot with several degrees of freedom. There are cases in which both the laser head and the substrate move. Figure 1.3 illustrate a system in which both substrate and laser head move. The laser head which is integrated in a coaxial nozzle moves by a robot and the substrate rotates by a motor. Many algorithms exist for providing appropriate relative velocity and acceleration.

1.4 Laser Cladding Parameters

There are many parameters involved in laser cladding making laser cladding a complex process. The output of laser cladding is composed of many factors such as microstructure, hardness, clad geometry including clad height, width, angle of wetting, and cross sectional profile, cracks, pores, residual stresses and dilution [2]. The way that these input parameters affect the output parameters is not comprehensively known although efforts have been performed to investigate these effects by modeling and analysis of the process. The input parameters can be categorized into 5 groups [2]:

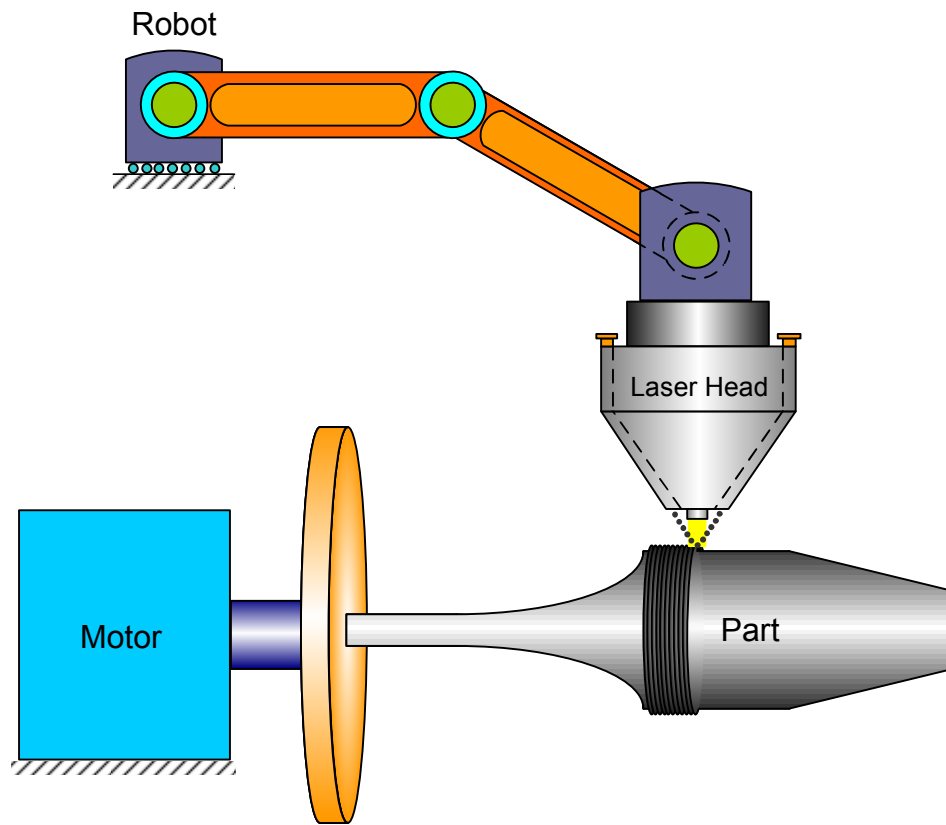


Figure 1.3: Laser cladding: Moving head by robot and moving substrate along with coaxial nozzle

Table 1.2: Types of lasers utilized in laser cladding and their specification [2]

| Characteristics | CO ₂ | Nd:YAG lamp- pumped | Nd:YAG diode- pumped | HPDL |
|---|-----------------|---------------------------|----------------------------|--------------|
| Wavelength [μm] | 10.06 | 1.06 | 1.06 | 0.65 – 0.94 |
| Efficiency [%] | 5 – 10 | 1 – 4 | 10 – 12 | 30 – 50 |
| Maximum power [kW] | 45 | 4 | 5 | 6 |
| Average power density [W/cm^2] | 10^{6-8} | 10^{5-7} | 10^{6-9} | 10^{3-5} |
| Service period [hour] | 1000 – 2000 | 200 | 5000 – 10000 | 5000 – 10000 |
| Beam Parameter Product (BPP) [$mm \times mrad$] | 12 | 25 – 45 | 12 | 100 – 1000 |
| Fiber coupling | No | Yes | Yes | Yes |

Laser: Average power, spot size, wavelength, pulsed or continuous wave, beam profile, and laser pulse shaping.

Motion device: relative velocity, relative acceleration, and system accuracy.

Material: substrate geometry, composition, metallurgical, thermo physical and optical properties, powder size, and surface tension.

Powder feeder: powder feed-rate, inert gas flow rate, nozzle specification, and powder stream profile.

Ambient properties: preheating, shield gas velocity, and type of shield gas.

In addition, many physical phenomena are involved during the process including [2]: absorption, conduction, diffusion, melt pool dynamics, fluid convection, gas/melt pool interaction, laser attenuation by powder and solidification. Small change in any of input parameters would result in output parameters variation. Moreover, sometimes without any change in input parameters, the result is different. This arises probably from these factors:

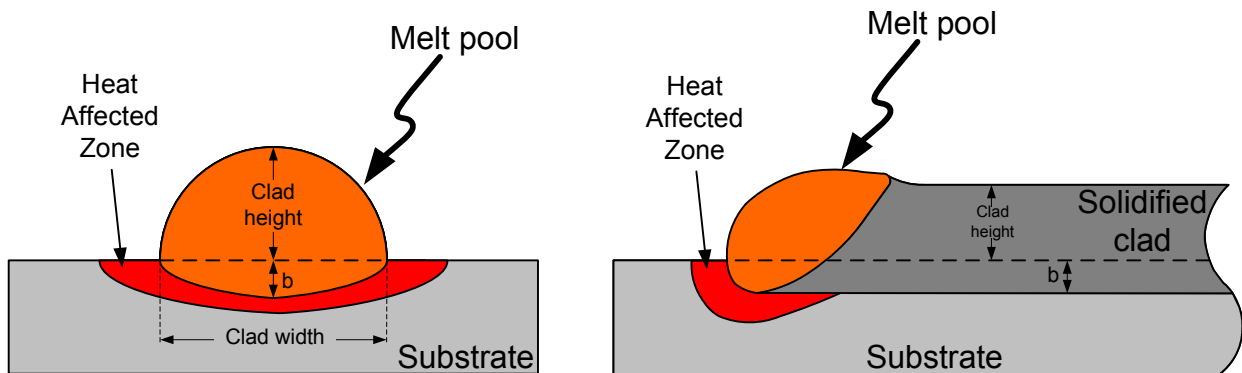


Figure 1.4: Clad geometry

- Lack of observation on several input and output parameters,
- External disturbances such as change in humidity of the environment or amount of Oxygen in the process zone,
- Temperature dependency of thermo-physical and optical parameters.

As a result, the designation of proper input parameters for obtaining desired output parameters is very challenging. In an automated fashion, the system should figure out changes in the output parameters and in real-time, change the input parameters in order to maintain the output parameters constant. In addition, in many processes adaptively altering process parameters is imperative in order to make complex parts. This makes a closed-loop control system for laser cladding inevitable for these processes. Utilizing a closed-loop control system in laser cladding makes the system less sensitive to external and internal disturbances. Having a closed-loop control system for laser cladding would contribute to huge improvement in clad quality and reduction in cost. Any closed-loop control system consists of feedback, and feedback comes through sensors. Hence, a feedback sensor is an essential device in a closed-loop control system. Candidates for feedback parameters are powder feed-rate, melt pool temperature, melt pool geometry, and rate of solidification. Figure 1.4 depicts the clad geometry characterization which can be used as a feedback signal. In this figure, b shows the depth of the clad penetration into the substrate.

The measurement of these parameters can directly or indirectly indicate the clad quality. A controller can be designed to close the control loop, when the correlations of the feedback signals with the input parameters are identified. Among different input parameters, laser power, laser beam diameter, powder mass flow rate and relative velocity of melt pool seem to have major effect on the outcome; therefore, mostly they are considered as the control variable.

1.5 Objective Statement

As mentioned before, a closed-loop control system can contribute drastically to the progress of laser cladding. The clad height is one of the output parameters which can be used as a feedback signal in closed-loop control of the process. The clad height is of great importance especially when laser cladding is utilized in fabrication of parts in layer by layer fashion (e.g., RP). Having control over the clad height leads to a more accurate geometry. The measurement of the clad height in real-time in non contact fashion can be done in several ways which will be discussed in Chapter 2. Utilizing CCD cameras in order to measure the clad height in the real-time fashion has several advantages over other methods, including low cost integration, high resolution, high accuracy, and providing additional information which could be used for identification of other important geometrical parameters such as the clad width and the angle of solidification. In this thesis, the measurement of the clad height in real-time by using CCD cameras will be described. The major objective of this thesis is to develop image-based feature tracking algorithms to be used in real-time clad height detection in laser cladding.

1.6 Looking Ahead

The rest of this thesis is arranged in the following order: In Chapter 2, a literature survey and background on using several output parameters as feedback in closed-loop control of laser cladding will be represented. Experimental set up and data acquisition associated matters will be provided in Chapter 3. Image processing of the melt pool images in order

to extract the border of the melt pool can be found in Chapter 4. Chapter 5 describes image feature tracking algorithms and experimental results. Chapter 6 offers conclusion and recommendations.

Chapter 2

Literature Review and Background

This chapter represents background of laser cladding technology with particular focus on sensing, monitoring and real-time control of the process.

2.1 Laser Cladding

Laser cladding has been introduced in the mid 70's [3, 4]. Steen and Courtney [5] and Weerasinghe and Steen [6] depicted the process in early 80's. Rolls Royce[©] reported utilizing the process in production in 1981 [7, 8]. Since then many research groups participated in the research, development and improvement of the process. Some of these research groups from which, most of the available literature comes, along with the name they are employing for laser cladding and the country of origin are:

- Albrecht Roders GmbH & Co KG, GERMANY, Controlled Metal Buildup (CMB),
- Electrolux Rapid Development, FINLAND, Direct Metal Laser Sintering (DMLS),
- Fraunhofer Institute for Production Technology, GERMANY, Controlled Metal Build-up (CMB),
- Los Alamos National Laboratory, USA, Direct Light Fabrication,

- National Research Center (Affiliated company: Accufusion), CANADA, Freeform Laser Consolidation (FLC),
- Penn State University (Affiliated company: AeroMet), USA, Laser Additive Manufacturing (LAM),
- Raja Ramanna Center For Advanced Technology, INDIA, Laser Rapid Manufacturing (LRM),
- Sandia National Laboratory (Affiliated company: Optomec Design Company), USA, Laser Engineering Net ShapingTM (LENS), Direct Metal Deposition SystemsTM (DMDS),
- University of Illinois, USA, Center for Laser Assisted Material Processing (CLAMP),
- University of Liverpool, ENGLAND, Laser Cladding and Direct Fabrication, Direct Laser Fabrication (DLF),
- University of Manchester, ENGLAND, laser direct metal deposition, laser additive manufacture,
- University of Michigan (Affiliated company: Precision Optical Manufacturing), USA, Direct Metal DepositionTM (DMD),
- University of Purdue, USA, Laser Cladding,
- University of Waterloo (Affiliated company: Smart Fabrication), CANADA, Laser Cladding, Laser Powder Deposition, Laser Freeform Fabrication.

2.2 Control of Laser Cladding

Control of laser cladding has a great impact on the improvement of the produced clad and, in turn, of the final part. Several research pursuits have been conducted in order to integrate the laser cladding process in a closed-loop feedback control system, however,

little progress has been reported. As mentioned before, this arises from the fact that the process is vastly complex and numerous input and output parameters are involved. Furthermore, quite a few of them are coupled. Besides, the process is extremely sensitive to small changes in the operational conditions. Additionally, some of the parameters are not inherently measurable or the measurement is not practical. One of the factors that matters greatly in the control of laser cladding, is selecting of a proper parameter as the feedback signal. The following criteria can help to choose the right parameter:

- The parameter should be practically measurable with high frequency,
- The measured value for the parameter should be an indicator of the features of the produced clad,
- The measurement of the parameter should not disturb the process or put any obstacle in the way of the process,
- The measurement of the parameter should be cost effective.

Different research groups have used different parameters as the feedback signal such as, powder feed-rate, melt pool size, and melt pool temperature.

2.2.1 Powder Feed-Rate as a Feedback Signal

Some researchers utilized powder feed-rate as a feedback signal. Closed-loop control of powder feed-rate leads to supply the melt pool with a constant powder feed-rate which, in turn, provide consistent melt pool size while other parameters remain unchanged. This improves laser cladding process and specially is important for producing functionally graded materials in which several powder feeders are employed to supply the melt pool with different kinds of powder materials. The available powder feeder in the market use sensors to continuously monitor the remained powder weight inside the hopper as a signal to control the powder feed rate by changing the rotational speed of a feed screw [9]. In general, the time delay between sampling and obtaining desired feed-rate is long. Furthermore, these powder feeders are not capable of supplying low feed-rates required in laser cladding.

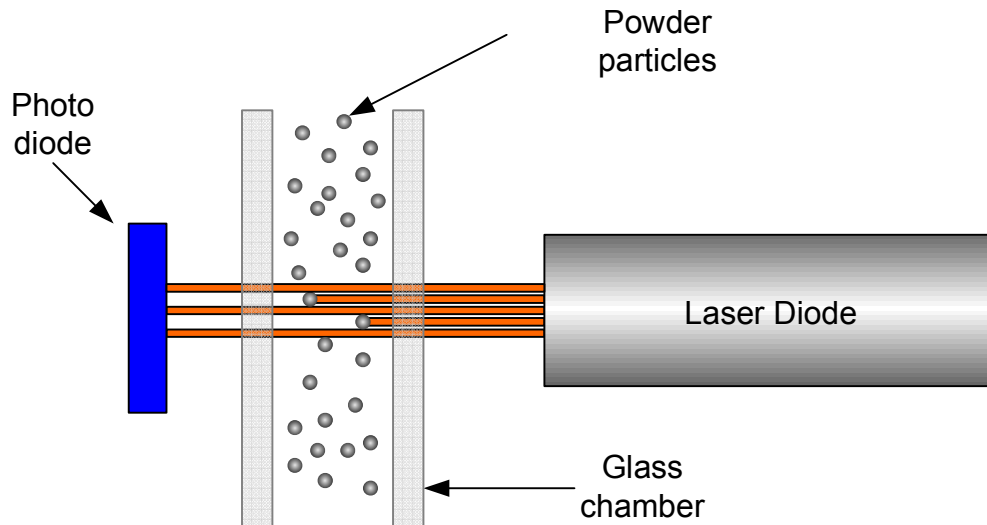


Figure 2.1: Schematic view of developed sensor for powder feed rate adapted from Hu and Kovacevic [9]

Several attempts have been conducted in order to develop sensors and powder feeders which can produce stable and low powder feed-rate in high frequency.

Hu and Kovacevic [9, 10] developed a sensor to measure the powder feed-rate. They placed one photo diode in front of a light source (i.e., laser diode). The laser diode emanates a red light within a wavelength of 600-700 nm and a power less than 500 mW. The powder and carrier gas stream pass a glass window that has been placed between the two. The emitted light from laser is detected by the photo diode and converted to voltage signal. Figure 2.1 depicts schematic view of the sensor [9].

The absorbed energy by the photo diode depends upon the powder particles that are in the pass of laser light at the moment. An increase in the powder feed-rate yields to decrease in the absorbed energy. The sensor obtains data at frequency of 10 Hz. The authors reported that the sensor can measure the powder feed-rate in the range of 3 to 22 g/min. However, in many applications, the powder feed-rate should be less than 3 g/min.

Meriaudeau et. al. [11, 12, 13, 14, 15] employed CCD camera in order to detect powder stream distribution. Prior to turning on the laser, the CCD camera captures images from the powder stream continuously in order to detect the powder particle velocity which helps

the operator to choose proper carrier gas flow rate. In other words, the CCD camera is exploited for calibration process. Subsequent to turning on the laser, the CCD camera is employed to identify powder stream distribution. The diameter of the powder stream is measured at the closest point to the melt pool.

Doubenskaia et. al. [16, 17] and Bertrand et. al. [18] used a non intensified CCD camera to visualize powder particles inside the powder stream in laser cladding. The CCD camera (SonyTM ExviewTM HADTM CCD) has high quantum efficiency¹ in near infra red region. Development of a software to study particles velocity and size statistically was reported. Also, the average size and velocity of the particles were presented. The visualized powder stream and acquired values for velocity and size were employed to optimize the process by the help of an expert manpower. In fact, no attempt was made at integration of closed-loop control for the process.

2.2.2 Melt Pool Temperature as a Feedback

Measuring melt pool temperature is of great importance in laser cladding. It can be an indicator of clad quality, dilution, microstructure properties, mechanical properties, mass flow, and energy absorption to name a few. An infrared camera can be a convenient device for temperature monitoring of the process zone in laser cladding, however high cost of infrared camera put an obstacle in the way of utilizing it in laser cladding.

Doubenskaia et. al. [16, 19, 17] used non-contact pyrometry to monitor the melt pool temperature in Nd:YAG laser cladding. In order to protect the pyrometer from laser irradiation ($\lambda = 1064\text{ nm}$) a set of notch filters were utilized in the system. They used 2D monochromatic ($0.860\ \mu\text{m}$ wavelength, $2.5 \times 2.5\ \text{mm}^2$ vision zone, $1.7\ \text{ms}$ acquisition time) pyrometer to acquire 2D temperature mapping of the process zone. They investigated the effect of altering powder feed-rate and laser power parameters on temperature distribution of the process zone. Also they showed temperature deviation in the process zone caused by applying pulsed laser with rectangular shape pulse as well as 2D steady state temperature distributions as a result of applying continuous wave laser. In addition, they employed

¹The definition of the parameters related to CCD camera and their effects on the captured images will be discussed in Chapter 3.

1-spot multi-wavelength (12 wavelengths in the spectral range $1.0 - 1.573 \mu m$, $800 \mu m$ vision zone, $50 \mu s$ acquisition time) pyrometer in order to measure the true temperature of the process zone.

Meriaudeau et. al. [20, 14, 21, 22, 23] and Legrand et. al. [24] used a CCD camera to measure the process zone temperature distribution. The work is based upon Planck's law of black body radiation which defines the relationship between temperature of a black body and the spectral intensity of electromagnetic radiation for different wavelengths. They showed the grey level value in captured images by the CCD can be approximated by linear relationship with black body temperature. It has been claimed that the system possessed a thermal resolution around $5^{\circ}C$ which is promising. They utilized the system to monitor the surface temperature in the process zone during the cladding. However, their results were not compared to the real temperature of the process zone measured by other measuring devices. In fact, the results suffer from the lack of verification.

2.2.3 Melt Pool Geometry as a Feedback

Hu et. al. [9, 25, 26, 27, 28] developed a system to measure melt pool size in laser cladding. They used an infrared camera with high frame rate (up to 800 frames/sec) on the top of the melt pool and the laser delivery system. The emanated light passes through the laser delivery system and reaches the camera. The camera captures top view of the melt pool in grey scale format with a 128×128 pixels resolution. An Nd:YAG laser blocker ($1060 nm$), an iris and an infrared filter ($> 700 nm$) were installed before the CCD sensor of the camera. As a result, the camera receives light with wavelength of 700 to $1060 nm$. Figure 2.2 [9] shows a schematic view of the setup used in the study. In order to find the gray level value corresponding to the liquid-solid transient edge of the melt pool in the infrared image, they located an ultra high shutter speed camera next to the infrared camera. A pulsed nitrogen laser was employed in order to light up the melt pool area. A notch filter with the wavelength of $337 nm$ has been installed before the ultra high shutter speed camera in order to let only the light with the wave length of around $337 nm$ (which is the wavelength of the emanated light from the nitrogen laser) reaches the ultra high shutter speed camera. One set of experiments was conducted while both cameras were

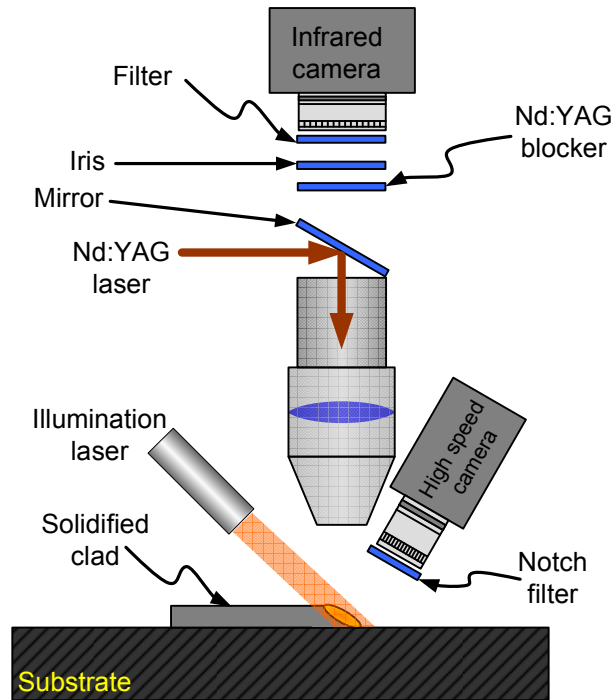


Figure 2.2: Schematic view of developed sensor for melt pool size [9]

capturing images simultaneously. Canny edge detection method was applied to acquired images by the ultra high shutter speed camera. Then the detected edges projected on the images taken by the infrared camera. In this way, the grey level value representing the liquid-solid transient edge acquired which reported 70 in 256 grey scale value. Then the high shutter speed camera was dismantled and the acquired number was considered as a threshold value.

A few experiments were conducted using mild steel as the substrate and H13 tool steel with 25 to 50 micron mesh size as the powder. Images were captured in real time by the infrared camera with frequency of 15 Hz . The images were thresholded and area of the melt pool was calculated. The area of the melt pool was utilized as a feedback signal for a simple PID controller. Applying the controller showed an improvement in the performance of the process. However, they did not mention the location of the ultra shutter speed camera in their report which is very important. Due to existence of the infrared camera,

the ultra high shutter speed camera cannot be located on the top view of the melt pool, and as a result the location of the latter should be somewhere next to the infrared camera as they reported in their report. Thus, the camera axis is not perpendicular to the melt pool and the effect of image projection should be considered. Furthermore, the edge detected by Canny method was considered as the boundary of the melt pool, which can be just an estimation of the actual size of the melt pool since they did not evaluate the acquired size with the real size of the melt pool and, in fact, this is a very difficult task. For example if they apply an edge detection method other than Canny method, the result would be different. However for the interest of the controller, the calculated melt pool may be a good control variable.

Triangulation sensor has been employed for distance measurement in industry for decades [29]. This sensor works based on triangulation concept as illustrated in Figure 2.3. The light source emanates a beam light, which passes through one lens. The lens could be collimated lens or focusing lens depending upon the application. The laser rays are focused or are made parallel by the help of the lens. Then the light strikes the object and the reflected light passes one imaging lens and strikes a light detector. The light detector can be a linear position sensitive opto-electronic detector (PSD) or a Charge Coupled Device (CCD) camera depending on applications. PSD produces electrical current on its both ends which are connected to two electrodes (A and B). These currents are proportional to the distance of spot light from center of PSD [29]:

$$\begin{cases} I_A = I_0 \frac{R_D - R_x}{R_D} \\ I_B = I_0 \frac{R_x}{R_D} \end{cases} \quad (2.1)$$

where,

I_A is the output current at A ,

I_B is the output current at B ,

I_0 is the current produced by beam light,

R_D is the resistance between A and B ,

R_x is the resistance between incident point and B .

Since the resistances are proportional to the distances:

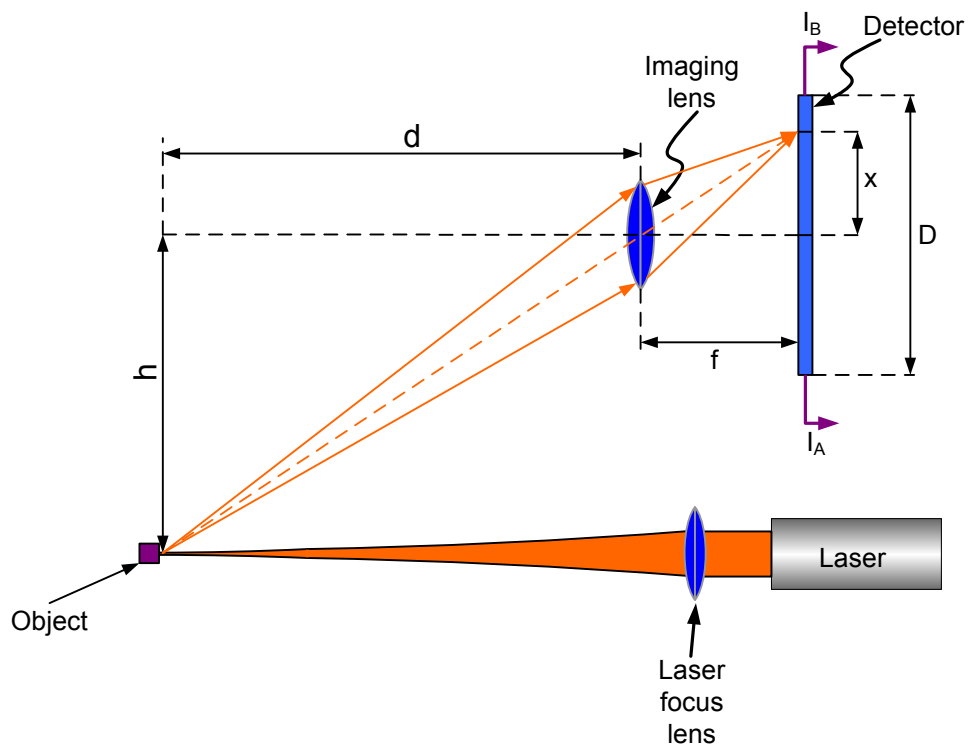


Figure 2.3: Schematic view of triangulation sensor

$$\begin{cases} I_A = I_0 \frac{D-x}{D} \\ I_B = I_0 \frac{x}{D} \end{cases} \quad (2.2)$$

if we assume $P = \frac{I_A}{I_B}$ then:

$$P = \frac{I_A}{I_B} = \frac{D}{x} - 1 \implies x = \frac{D}{P+1} \quad (2.3)$$

from geometrical relation in Figure 2.3,

$$d = f \frac{h}{x} \quad (2.4)$$

by substituting x of Equation (2.3) into Equation (2.4):

$$d = f \frac{h}{D} (P+1) \quad (2.5)$$

Hence, the sensor can measure the distance of the object with respect to the sensor. Using PSD as a light detector has several advantages such as fast processing speed. It can process data up to 200 kHz [30] or even faster as opposed to CCD camera which hardly can go beyond 50Hz. Furthermore, its spectral response is from 320 to 1100 [29], which is wider than that of a regular CCD camera, which is around 400 to 1000 nm. However, the only information that PSD can provide is the distance, while the CCD camera can offer a gray scale image which can be used to extract more information about the object. In general the beam of light should be as thin as possible and therefore always laser, mostly solid state diode laser, is utilized as the light source. Emanated light by solid state laser are in a narrow spectral wave length (e.g., 800 *nm*). Laser Measurement International (LMI) has reported utilization of this sensor in arc welding [30]. Existence of extreme light intensity in arc welding places an obstacle in the way of utilizing this sensor. LMI overcame this obstacle by applying this technique. A solid state pulsating laser was employed as a source of light. The emitted light is in a narrow band spectral wavelength and also in a narrow band of frequency. Utilizing a narrow band pass optical filter before the light detector yields to restrict the receiving light to the light detector to wavelength range around that

of laser. A PSD was used as a light detector. The output of the PSD using an electrical lock-in amplifier was filtered to the frequency range of pulsating laser. As a result, the final output is representative of wavelength and frequency range of the pulsing laser. In other words, LMI developed a sensor which can measure the height of weld in real time and with high frequency using this technique. However, the offered information by the sensor is limited to only the height of weld, and the sensor can not provide any other information. As a result, although having the height of weld is beneficial for the closed-loop control of the system, more information about the process zone is needed. Utilizing “structured light” instead of one single laser beam and a 2D CCD based sensor being able to detect light in several points inside a frame result in surface contour mapping [30]. The author could not find any report on utilizing triangulation sensor in laser cladding; however, it seems that implementing the same technique for laser cladding is feasible.

Beersiek et. al. [31, 32, 33, 34] utilized a CMOS Camera on the top of the laser beam in different types of laser material processing as seen in Figure 2.4. Employing CMOS camera has the advantages of higher fast frame rate and cheaper price as opposed to CCD camera. While frame rate of regular CCD camera is about 50 Hz, CMOS camera is capable of capturing images with the frame rate up to 1 kHz. The applications in which the scanning speed of the laser beam is high such as laser welding, CCD camera could not be a choice due to its low image capturing speed. On the other hand, there are distinctive regions in the processing zone of laser processing, particularly in laser welding that have different characteristics. As Figure 2.4 presents three regions in the processing zone of a typical laser material processing (e.g., laser welding):

Keyhole: When laser strikes and focuses on the substrate, keyhole is generated. Evaporation of the molten metal yields to stable keyhole inside the molten metal. This metal vapor emits acoustic waves [35, 36, 37, 38] and emanates light which is in the visible and infrared spectral range.

Plasma: Further interaction between the laser beam and the vapor metal results in formation of plasma. Plasma emanates light in visible and ultraviolet spectral range [39].

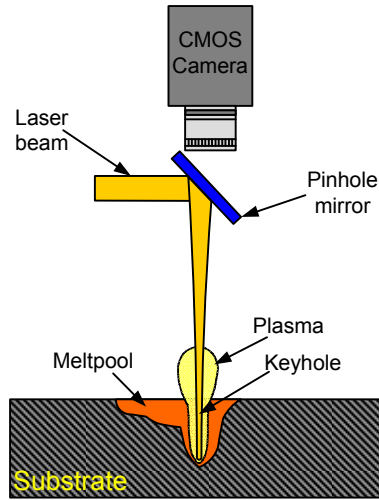


Figure 2.4: Utilizing CMOS camera for monitoring of processing zone in laser beam welding adapted from [31, 32, 33, 34]

Melt-pool: Melt pool radiates light base upon black body radiation. As a result, wavelength of emitted light by the melt pool can be determined based on the temperature of melt pool. (This feature will be investigated in depth in succeeding discussions)

The spectral response of a CCD camera cannot cover the spectral range of keyhole and melt pool together. However, a CMOS camera has a wider spectral response which makes it capable of detecting both signals. The dynamic range of a CMOS camera is 120 dB light density (The conversion of light density to voltage in CMOS camera is logarithmic) while for a CCD camera, it is 60 dB. The difference between light density of melt pool and keyhole is less than 120 dB, hence CMOS camera can detect both region. However, the resolution of CMOS camera is much lower compare to CCD camera.

For increasing the frame capturing speed, only a part of image which is of interest was considered in the images. A few regions in each image were detected and base upon those, for each application a few distinctive features which are representative of specific characteristics of the weld were considered. As an example, the intensity of the emitted light of keyhole region was considered as indication of penetration depth. The capturing

and processing of images with the frequency rate of about 1 kHz were reported in the articles. The work offers valuable information about the parameters of weld, however it does not provide the exact weld geometry.

Haferkamp et. al. [40] developed a new visual system for recognition of dynamic behaviour of the melt pool, and melting and solidification front velocity in the melt pool of aluminium alloys. A pulse Nd:YAG solid state laser ($\lambda = 1064nm$) with pulsing period in the range of micro second and high pulse peak power was utilized to remelt the aluminium alloy. A frequency doubled Q-switched Nd:YAG laser system with $\lambda = 532nm$ and pulse duration of 10 ns was exploited as a frequency selective lightning. Image processing was applied to acquired images in order to extract variation in reflection and Electromagnetic wave backscattering properties of the material surface. Extracted information is representative of transient development of the solid and the liquid isotherm, phase transitions and melting and solidification front velocity within the processing zone. The author could not find type of the image acquisition device. Haferkamp et. al. [41] employed a micro focus radioscopy and a high shutter speed video camera to monitor the mass flow inside the melt pool.

Voelkel and Mazumder [42, 43] developed a novel system for capturing quality pictures of the melt pool in CO₂ laser welding as shown in Figure 2.5. A 1 kW CW CO₂, TEM₀₀ utilized to generate the melt pool. A 3.5 W argon-ion laser with the wavelength of 488 nm produced illumination light which by passing through a lens shines at the melt pool region. Some portion of the argon-ion laser passes through two diffuser plates in order to be scattered as shown in Figure 2.5. The two diffuser plates were constituted from opal to glass. The first one which was smaller reduces the impact of flecks on the image by vibration. The solid angle between the melt pool and the illuminated part of the diffuser plate was enlarged by the second diffuser plate. The second diffuser was 4×7 cm and was 5 cm apart from the melt pool. A CCD video camera monitored the melt pool. A narrow band pass interference filter with the wavelength of 488 nm was placed in front of camera and a thin metal sheet with the 4 mm diameter hole was placed in front of the filter in order to protect the filter from contamination. Thus, light only through the 4 mm protective plane and in the narrow band width of around 488 nm can reach the camera.

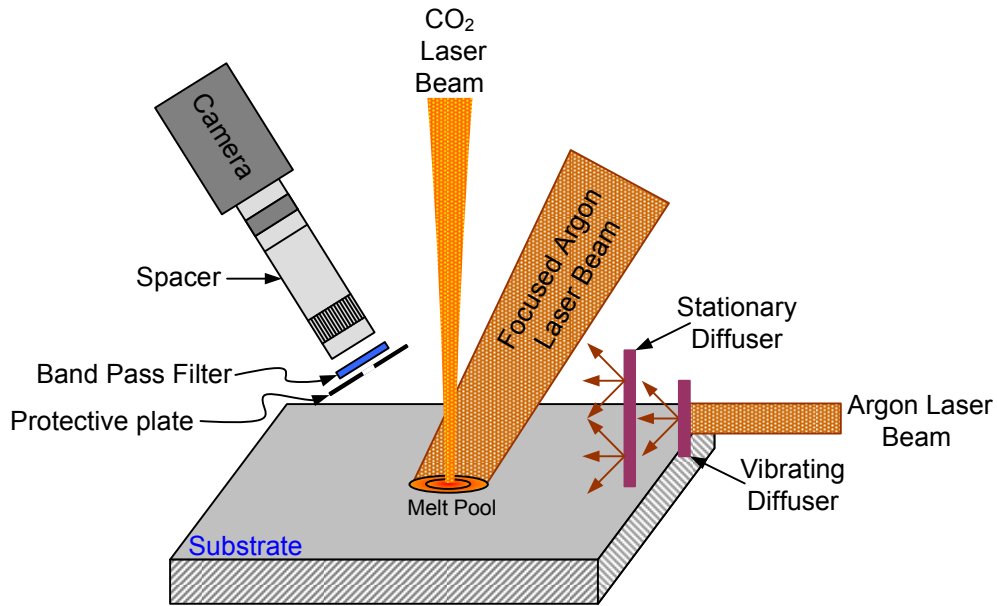


Figure 2.5: Melt pool visualization in laser welding adapted from [42]

One spacer with the length of 18 *cm* was placed between the lens and the CCD sensor. The distance from metal sheet to the melt pool was set to 7 *cm*. They surveyed the effect of illumination laser and diffusers over the quality of the acquired images. For example, existence of diffused laser has great impact on enhancing the quality of images. They could obtain promising images by utilizing simultaneously focus light and scattering light.

2.3 Conclusion

Measuring clad geometry is of great importance in laser cladding and can be a good control variable especially for the purpose of RP. As mentioned, most of the efforts were limited to approximating the melt pool perimeter. For the height measurement, most of the works concentrate on keeping the height constant at a predefined value or to measure the deviation of the height as opposed to measuring the actual height. As seen in the literature review, researchers attempted to measure height fluctuation and use it to optimize the process by changing the input parameters. Changing the input parameters is accomplished either by

an expert manpower or by a closed-loop control system. For validation of the developed algorithms, visual comparison between the produced clad with and without the algorithms was taken place which only shows progress of the process, and not the accuracy of the measurement of the height deviations. Besides, to the best of the author's knowledge, the measurement of the actual height has not been investigated yet.

Furthermore, most of the published papers suffer from not providing details of the height approximation algorithms. Especially when optical detectors were utilized as data acquisition devices, image processing algorithms, locations of cameras, issues related to the direction of clad with respect to the cameras, and the developed algorithms of height approximation were not discussed in detail. Moreover, a few research efforts have been conducted to capture informative images from the melt pool; however, little progress has been reported. All these make this research agenda far from complete.

Based on the aforementioned shortcomings, in this study, the utilization of CCD cameras and issues associated with obtaining high quality images of the melt pool will be discussed. Capturing quality pictures potentially would provide much valuable information about the process. This information could include, but is not limited to, melt pool geometry (i.e., melt pool height, width, melt pool profile, and wet angle), angle of solidification, melt pool temperature, and melt pool temperature distribution. The better quality picture, the more information could be extracted. The issues regarding path dependency of the melt pool image will be addressed. The analysis of the acquired images will be described in detail. The development of algorithms to measure clad height in real-time will be explained. Comparison between the predicted height and actual height measured offline will be presented.

Chapter 3

Experimental Setup

3.1 Introduction

As mentioned in Chapter 1, an automated laser cladding system comprises several elements such as high power laser, powder feeder, multi axes CNC machine or a robot with several degrees of freedom, nozzle and intelligent central controller. In this chapter, the laser cladding configuration in Automated Laser Fabrication (Alfa) at the University of Waterloo will be introduced. Furthermore, tackling the issues pertinent to image acquisition in the presence of harsh and intensive light will be investigated.

3.2 Experimental Setup

A schematic view of the entire system has been illustrated in Figure 3.1. The elements of this configuration will be explained briefly in the following:

Laser source: A LASAG FLS 1042N Nd:YAG pulsed laser with a maximum power of 1000-watt is utilized as a source of energy. The wavelength of this solid-state laser is 1064 nm. Pulsation frequency, peak energy per pulse and laser pulse width is adjustable.

Powder feeder: A 9MP-CL Sulzer Metco powder feeder is used for which the powder feed rate (mass rate) and the carrying gas are adjustable. They are controlled by integrated closed-loop system inside the powder feeder. The powder feeder is able to provide any

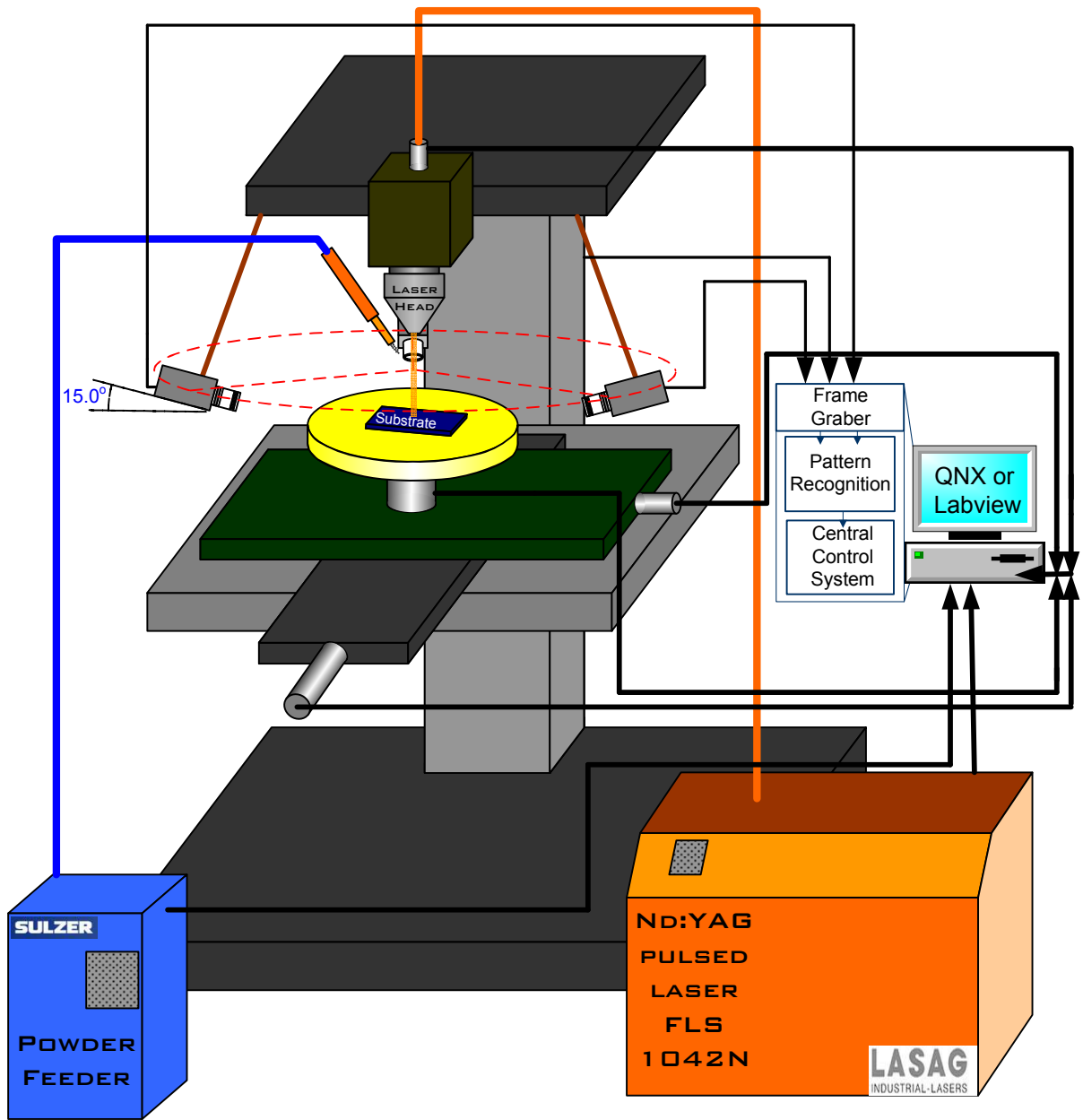


Figure 3.1: Schematic view of the laser cladding system at the University of Waterloo



Figure 3.2: UW Powder feeder

powder feed-rate larger than 0.5 g/min with acceptable fluctuations. However, the amount of fluctuation increases with the decrease in the powder feedrate. To enable a low powder feedrate (less than 1 g/min) with low fluctuation rate, a new powder feeder was designed and built at the University of Waterloo. The powder feeder works based on gravity and mechanical wheel principals. The feeder was designed with a low footprint to allow multiple feeders to be placed side by side. With the appropriate nozzle, different powders could be loaded in each feeder and super alloys could be created. Figure 3.2 shows the UW powder feeder.

CNC table: A 4 axes CNC table is exploited in order to generate relative motion between the laser head and the substrate. Figure 3.3 shows the CNC table.

Nozzles: A lateral nozzle is employed as a powder spraying device. Furthermore, a coaxial nozzle was developed to enable a path independent deposition. provide more options for the powder delivery system. Three powder inlets were included on the coaxial nozzle to allow mixing of various powders. Several enhancements were made to the nozzle including shaping gas fine tuning and water cooling. The nozzle was designed to hold the optical head resulting in easy integration. Figure 3.4 shows lateral nozzle and the laser head.

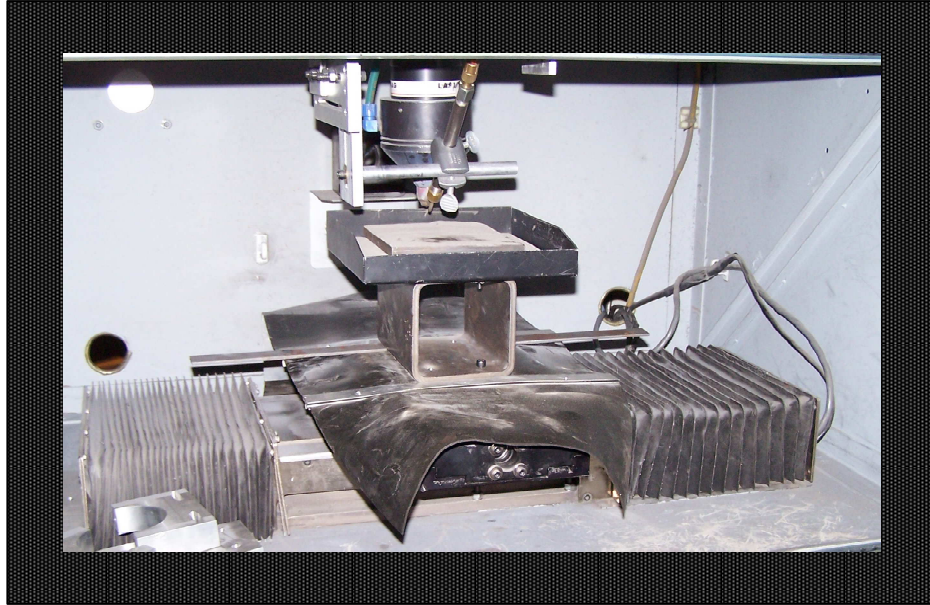


Figure 3.3: 4 axes CNC table used in the laser cladding

Figure 3.5a shows coaxial nozzle and Figure 3.5b shows powder stream in exit of coaxial nozzle.

Real-time operating systems: Two real time operating systems, QNX platform and NI real time platform (Labview) were installed on the system; As a result, the system can be operated by one of the two system separately. QNX benefits from higher processing speed as opposed to Labview; however, Labview is very user friendly. Thus, Labview was employed in this research and development.

3.3 Image Acquisition Device

Capturing high quality images of the melt pool in which melt pool can clearly be recognized from the surrounding area is a formidable task. As mentioned in Chapter 2 a few research efforts have been conducted to capture informative images from the melt pool; however, little progress has been reported. Capturing quality pictures potentially would provide us with much valuable information about the process. This information could include,

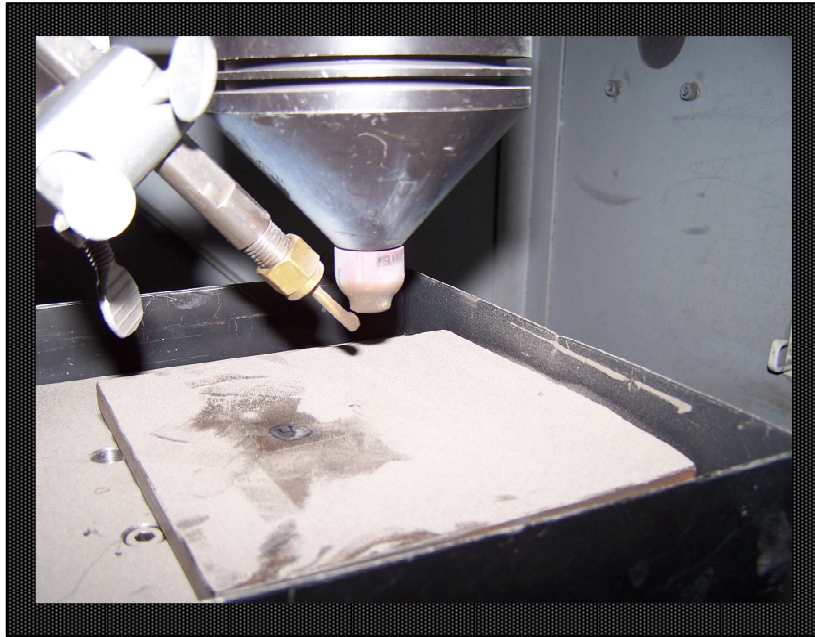


Figure 3.4: Lateral nozzle and laser head

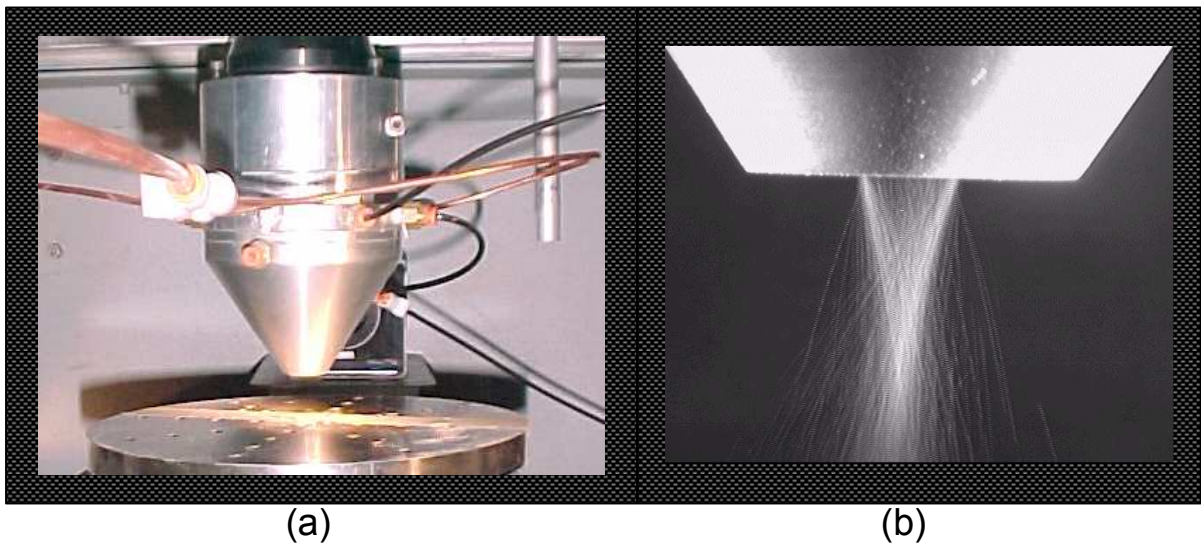


Figure 3.5: a) Coaxial nozzle designed at UW b) Powder stream from the coaxial nozzle when the carrying gas is at 5 SCFH, powder feedrate is 1.5 g/min, and 3 SCFH shaping gas

but is not limited to, melt pool geometry (i.e. melt pool height, width, melt pool profile, and wet angle), angle of solidification, melt pool temperature, and melt pool temperature distribution. The better quality picture, the more information could be extracted. The process intrinsically put obstacles on the way of capturing images, because:

- The presence of harsh and intensive light in the process zone arises from different sources such as high power laser irradiation, black body radiation, specular surface reflection and other kinds of reflections.
- The presence of various sources of noise such as flares and light reflections.
- Hostile environment around the process zone impedes to locate the imaging device close to the melt pool.
- Moving part by a multiple axes CNC machine restricts the location of the camera. As a result, choosing proper locations for cameras is challenging.

There are four kinds of regular digital camera in industry based upon the type of the sensor integrated in them [44, 45]:

- Charge Coupled Device (CCD),
- Complementary Metal Oxide Semiconductor (CMOS),
- Electron Multiplying Charge Coupled Device (EMCCD),
- Image Intensified CCD Camera (ICCD).

Charge Coupled Device (CCD) camera is the most common camera in industry and was chosen as the imaging device in our system. This selection was based upon availability, price and good resolution of the CCD camera. EMCCD and ICCD cameras are much more expensive than CCD camera and on the other hand, their high sensitivity put an obstacle on employing them for the laser cladding. EMCCD camera has higher frame rates and more sensitivity than CCD camera [44, 45]. ICCD camera employed for applications that short exposure time is needed. CMOS camera is cheaper and has higher frame rates than

CCD camera, however, at the expense of lower sensitivity and lower resolution [44, 45]. CCD sensor which is a light sensitive semiconductor chip comprises of many (nowadays in order of millions) tiny photo detectors (pixels). Utilizing CCD camera has some advantages and some drawbacks. CCD cameras are inexpensive which results in cost reduction in the integration of closed-loop control system in the laser cladding. In addition, it collects the data without being in contact with process zone or causing any disturbance to the process. Furthermore it benefits from high resolution (in order of millions pixels) which can lead to sharp and clear images.

There are two major drawbacks associated with CCD cameras: low frame rate and camera over exposition or saturation. Both of the two arise from the way a CCD camera works. When light strikes the CCD through the lens, each pixel gathers photons current and converts it to the electrical charge. The electrical charge is accumulated which is called “pixel’s accumulated charge” [44, 45]. In fact, each pixel performs as a capacitor. The generated electrical charge is proportional to the light intensity received by the pixel. The accumulated electrical charge is measured after specific amount of time; subsequently the electrical charge should be discharged to make pixels ready for next read out. The amount of time is dependent upon the light intensity. As a result, the frame rate in CCD camera is low (around 60 Hz). The first issue does not apply to laser cladding as the scanning velocity is in order of millimeters per second. Hence, having frame rate of 60 Hz seems acceptable.

The second issue is the camera saturation. The maximum charge a pixel can hold is limited which is called “full well capacity” or “saturation level” [44, 45]. Surpassing this saturation level leads to degradation of the signal and the charge overflows to adjacent pixels which is called “blooming”. The linear response of camera strays and makes camera’s response unreliable accordingly. The structure of CCD sensor is in a way that usually tends to let less charge overflow to horizontal pixels and more to that of vertical. Thus, a flash is observed more in vertical direction as a result of blooming. Lasting of the saturation for a considerable period of time results in the permanent damage of the CCD sensor. Full well capacity is a function of the pixel size in the CCD sensor, employment of multi-pinned-phase (MPP) mode, and the operating voltage of CCD. Size of pixel has the major role on

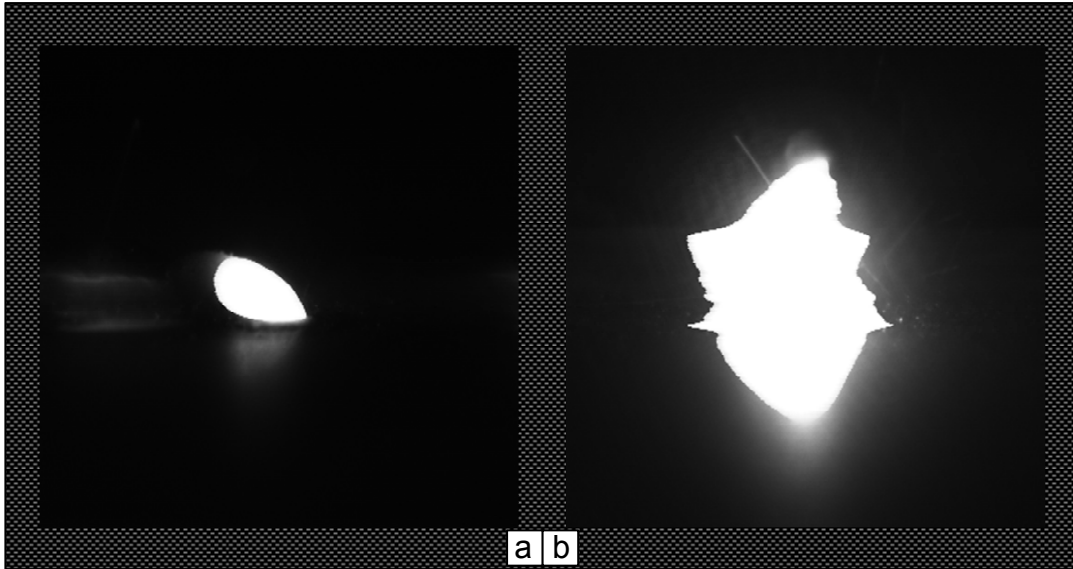




Figure 3.6: a) An image of the melt pool, b) An image of the melt pool when the CCD sensor saturated

determination of full well capacity. Larger pixels have higher full well capacity; however, an increase in the size of a pixel results in a decrease in spatial resolution [44, 45].

The effect of saturation is intensified when the image is of high dynamic range meaning that when it comprises low light signal and bright light signal simultaneously, which is exactly the case in laser cladding. The saturation problem has been frequently observed in laser cladding during the course of the experiments. Figure 3.6 shows a clear image of the melt pool and a saturated image. As seen, in saturated image, a flash obscured the entire process zone. The saturated image does not offer any useful information. It should be noted that when saturation happens, it does not occur in only one image; it may occur in several consecutive images periodically. In fact, when saturation arises, the entire set of images related to that experiment is useless, and the sensor could not provide any useful information. Part of this issue could be addressed through proper selection of the CCD camera; however, major part of the problem should be tackled by proper selection of filters which will be discussed in detail in Section 3.4.

Table 3.1: Specification of exploited cameras

| Camera type |  |  |
|----------------------|---|---|
| Image device | 1/3" Progressive CCD imager | 1/3" Hyper HAD CCD imager |
| Picture elements | 659 × 494 pixels | 510 × 492 pixels |
| Pixel size | 7.4μm × 7.4μm | 7.4μm × 7.4μm |
| Frame rate | 60Hz | Not provided |
| SNR | < 58dB | 45dB |
| Minimum illumination | 0.2 lux | 0.6 lux |

Before showing the specification of the employed CCD cameras, it is beneficial to explain two important factors of a CCD sensor [44, 45]:

- **Dynamic range:** is the ratio of full well capacity to the camera noise and describes camera's ability to detect very low light signals and very bright signals simultaneously. It is usually measured in dB by

$$DR = 20 \log \frac{C_f}{N} \quad (3.1)$$

where, DR is dynamic range and is measured in dB, C_f is full well capacity and is unitless, N is camera noise and is unitless.

- **Signal to Noise ratio (SNR):** is the ratio of measured signal to the overall noise in each pixel. It describes the quality of light measurement and a higher SNR leads to more precise light measurement.

Two types of CCD cameras were selected with specification listed in Table 3.1. The selection made based upon the price and accessibility.

3.4 Filter Selection

Exposing the CCD sensor directly to the harsh and intensive light arising from laser processing zone leads to an entire white image or damage of the CCD sensor as mentioned in the previous section. The present light in the process arise by several sources including laser radiation, black body radiation, the environment light and the reflection. These lights are in different wavelength range. The radiated light from the laser source is in the wavelength of 1064 nm . The wavelength of radiated light from the black body radiation source is not exactly known and should be scrutinized in order to calculate the wavelength range. The other important aspect of this investigation is the spectral response of the camera. In the following, each of these factors will be investigated in depth.

3.4.1 Spectral Response (Quantum Efficiency)

Photons are converted into electric charges in the CCD sensor. The ability of the photons to be absorbed in the depletion region of the detector depends upon the wavelength of the light. It is only the depletion region that photons are converted into electronic charges and subsequently can be held by the electric fields. The charge held in the depletion region is then transferred and measured. Photons striking on the CCD must first pass the region which is dominated by the gate electrodes by which the applied clocking voltages create the electric fields that form the boundary of the depletion region and transfer charge through the CCD. The gate structure can absorb or reflect photons based upon the wavelength of the light. As a result, there would not be one electron charge per one photon. The shorter wavelengths (blue light) are particularly absorbing, and below $\sim 350\text{ nm}$, they absorb all the photons before they can be detected in the depletion region. Photon with longer wavelengths (i.e., red photons) have a low probability of absorption by the silicon and can pass through the depletion region without being detected, and as a result reduce the red sensitivity of the CCD. Photons with wavelengths larger than 1100 nm do not have enough energy to create a free electron charge and they can not be detected by CCD. These factors govern the spectral response of the CCD [44, 45]. The spectral response is presented in a quantum efficiency which shows the probability of detection of a photon of

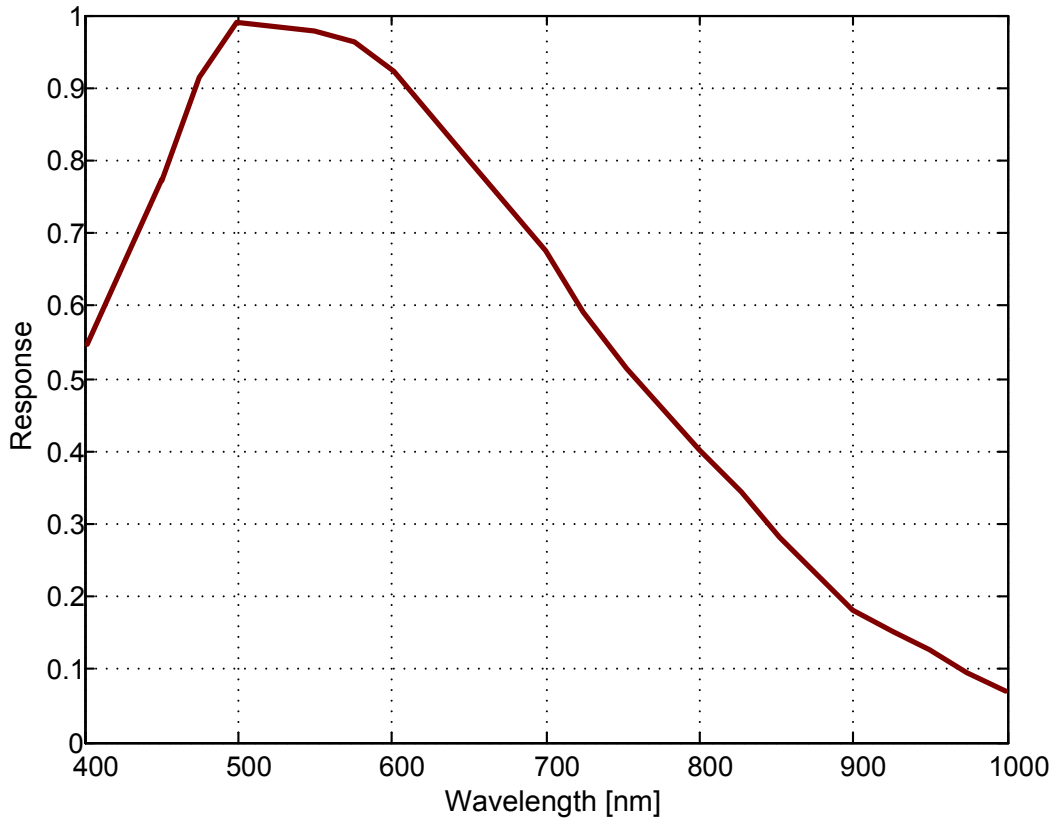


Figure 3.7: Spectral response of UNIQ UP-600CL extracted from manufacturer’s manual

a specific wavelength. For example, when the probability is 0.1 or 10 percent means one out of ten photons is detected. Figure 3.7 shows the spectral response of the UNIQ UP-600CL extracted from manufacturer’s manual. The typical spectral response of the SONY CCD camera is similar to that of UNIQ camera , in fact there is not considerable difference between spectral response of the two CCD cameras.

3.4.2 Black Body Radiation

Planck’s law of black body radiation defines the relationship between temperature of a black body and the spectral intensity of electromagnetic radiation for different wavelengths as:

$$E(\lambda, T) = \frac{2\pi hc^2}{\lambda^5(e^{hc/\lambda kT} - 1)} \quad (3.2)$$

where,

λ is the wavelength [m],

T is the temperature [k],

h is Planck's constant [$J.s$],

$c = 3 \times 10^8$ is the speed of light [m/s],

$k = 1.381 \times 10^{-23}$ [J/K].

Figure 3.8 shows graphical presentation of the Planck's law for the possible temperature range existing in the laser cladding process. Asselin [46] based on the Planck's law and camera's spectral response showed that adding a bandpass filter centered at $700nm$ results in capturing of maximum amount of light irradiated from the melt pool due to black body radiation. As a result, $700nm$ band pass filter was added to the camera's hardware in order to overcome the existence of harsh and intensive light, and to capture only the light originated from melt pool black body radiation.

3.5 Trinocular cameras

It is desired to acquire an image revealing full view of the melt pool. Since the melt pool is a three dimensions object, showing all the three dimensions in one image is not practical. On the other hand, the system inherently put some obstacle on the way of locating the camera at a desired position. First of all, there is a relative motion between the laser beam and the substrate; the substrate moves by multi axes CNC machine and in turn has multiple degrees of freedom motion. Hence the camera should not obstruct this path. Furthermore the space around the process zone is limited due to existence of the laser head, nozzle, substrate, and CNC table. Relative motion between the laser beam and the substrate yields to change in direction of tangential path vector to the generated track. Figure 3.9 shows a few directions of the tangential path vector to sinusoidal clad tracks. As seen, the tangential path vector can have all the angles between 0^0 and 360^0 with respect

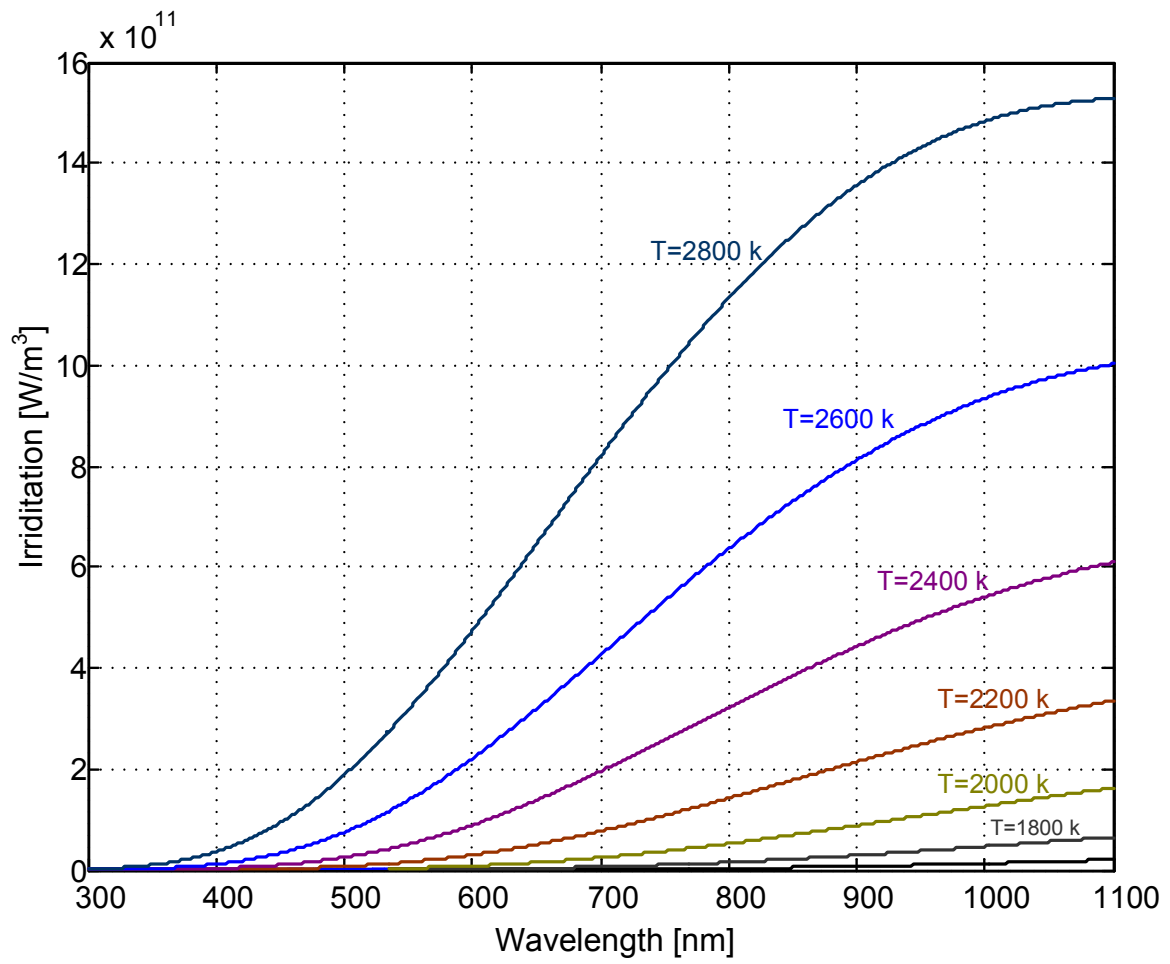


Figure 3.8: Planck's law: black body radiation

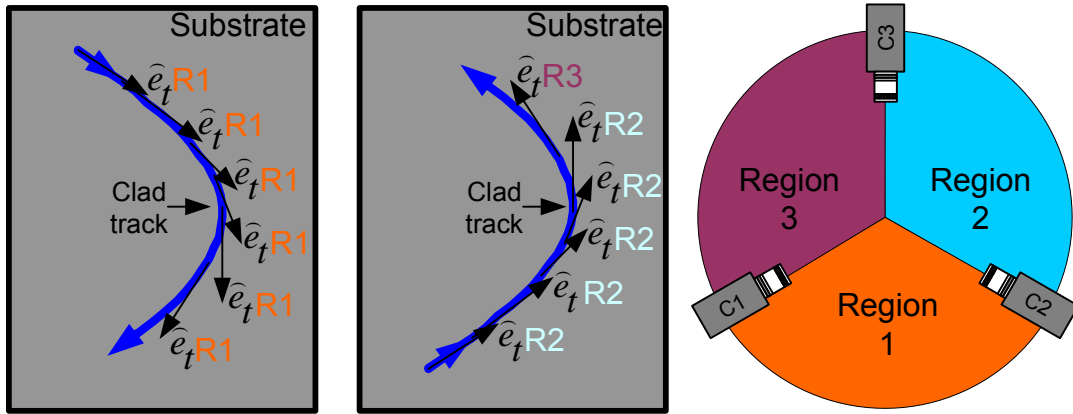


Figure 3.9: Tangential path vector's direction changes during a sinusoidal path and it places in different regions generated by trinocular cameras

to the positive direction of x axis. Based upon this angle, the position of the melt pool with respect to one stationary camera would be different, and in turn, the image of the melt pool would be completely different. For instance, when the clad moves on the camera axis and toward the camera (which means the substrate is moving away from the camera), the camera captures the front view of the melt pool which is the region of the interest. However, when the clad moves on the same axis but in opposite direction, the camera captures an image which based upon the angle of camera to the horizontal axis could be the back end of the melt pool or could not even capture any part of the melt pool due to blockage by the solidified clad.

In order to address these issues, a trinocular cameras configuration was designed. This configuration was patented by Toyserkani et. al. [47] at the University of Waterloo. In this arrangement, three CCD cameras are placed on an imaginary circle separated by equal angle (120° apart of each other). Each camera is located under the horizontal line and the camera axis has a 15° angle with the horizontal line as illustrated schematically in Figure 3.1 and by a picture in Figure 3.10. All the three cameras are focused on the process zone which is located under the process zone. At any moment, the tangential path vector places in one of the three regions between the cameras (see Figure 3.9); the two cameras next to the region monitor the front end of the melt pool and the other one monitors the back end

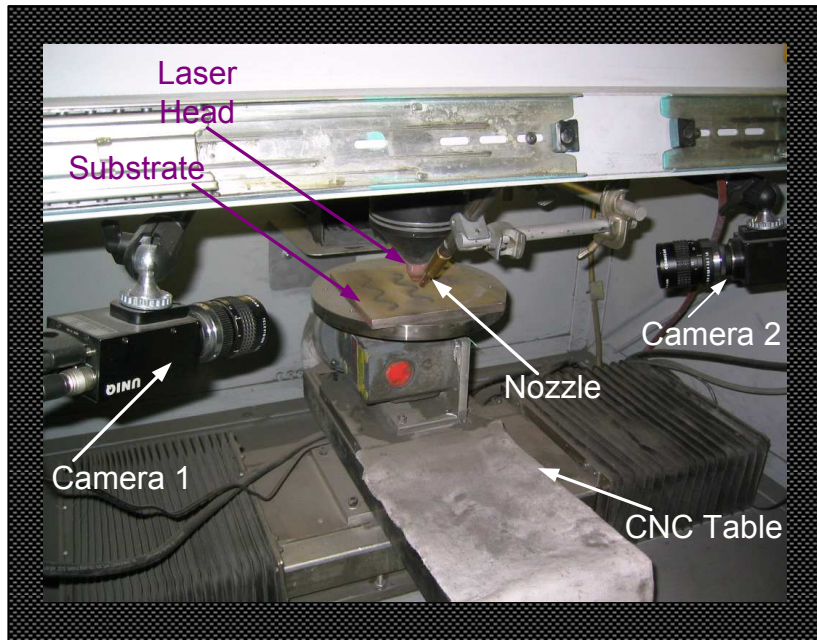


Figure 3.10: Trinocular cameras installed on the system

of the melt pool which is not of great importance. Hence the images from the cameras next to the region are saved for further analysis and the third image is not saved for the sake of increasing the processing speed.

Chapter 4

Image Processing

4.1 Introduction

The grabbed melt pool images by the cameras are in grey scale format. The images include two main regions, the dark region which represents the background or the surrounding of the melt pool and the bright area, which represents the melt pool. It is desired to separate the area which accurately presents the melt pool from its surrounding. In fact, precise determination of the melt pool is the fundamental of the algorithm, and improper determination of the melt pool leads to huge perturbation in the output of the algorithm. The algorithm needs the border of the melt pool for further analysis. Two approaches can be adopted in order to acquire the border of the melt pool. In the first approach, the image should be converted to the binary format (black and white) by applying a proper thresholding method, and then the border of the melt pool should be detected by exploiting a suitable edge detection technique. In the second approach the border of the melt pool can be detected using an appropriate edge detection technique. These two approaches involve two important image processing tasks namely “image thresholding” and “edge detection”. In this chapter, image thresholding technique and edge detection method will be discussed and the results of utilization of the developed techniques in obtained images in laser cladding will be presented.

4.2 Image Thresholding

Image segmentation is one of the most formidable tasks in image processing. Image segmentation divides a digital image into recognizable parts. In image thresholding, as a particular case of image segmentation, an image is segmented into two parts: foreground or object and background. Each pixel in grey level images has a grey value between 0 and $L - 1$ which corresponds to totally black (0) and totally white ($L - 1$) respectively.

Suppose [48, 49]:

$P = [I_{mn}]_{M \times N}$ represents the image in which I_{mn} is a pixel located at (m, n) and has a discrete grey value such that

$$I_{mn} \in \{0, 1, \dots, L - 1\} \quad (4.1)$$

thresholding is determination of a threshold value such as T which segments the image into two regions: object (O) and background (B) such that:

$$O = \{(m, n) | I_{mn} \geq T\} \quad (4.2)$$

$$B = \{(m, n) | I_{mn} < T\} \quad (4.3)$$

then I_{mn} becomes 1 for the object and 0 for the background or vice versa.

Choosing an optimal threshold value in each image depends upon many factors such as the image itself, the desired region, definition of the object, and applications. For example in one image the area of interest or the object for one specific application could be completely different from that of another application. For that reason there are many thresholding methods with specific applications. In other words, there is not a unique thresholding method for all applications.

When there is considerable difference between the grey level values of pixels in the border of object and the pixels belonging to the background the image thresholding is a straightforward task; however, when the border is composed of a hazy area which is frequently the case in obtained images in the laser cladding process, the thresholding is a complicated task. As mentioned earlier, several thresholding algorithms have been

developed in order to overcome the inherent complexity in real life images. Researchers categorized images based upon several criteria in order to develop proper thresholding algorithm for each criterion. Image histogram which presents frequency distribution of each grey value in an image or a region reveals important properties of an image and many thresholding algorithms exploit the information extracted from the histogram. It is quite beneficial to examine a few typical images from the process, their corresponding surface plot, and histogram. (see Figures 4.1, 4.2, and 4.3).

Figure 4.1a and 4.1b provide two typical images of the melt pool. Both images include a very bright melt pool, a relatively black background and hazy area around the melt pool. The surface plot of both images which are shown in Figure 4.1c and 4.1d illustrate the hazy area around the melt pool clearly as those lines which connect the peak value plane of the cylindrical area to the minimum grey value plane that are not perpendicular to the later. Divergence of the lines from the perpendicular lines indicates that there is not a distinctive boundary between the melt pool and the back ground. The histogram (the grey area shows the logarithmic histogram) of both images as shown in Figure 4.1e and 4.1f. It is observed that there is not a valley in the histograms. In fact, between the two peaks of histogram (at grey value of 20 and grey value of 255), the frequency smoothly decreases and in some regions the frequency is almost constant. Both images have large standard deviations which indicates large amount of dispersal from the mean value. Two more typical images have been provided in Figure 4.2a and 4.2b. Figure 4.2a comprises a large black area as the background, a white area as the melt pool, some reflections and blurred area, and relatively solidified clad at the back end of the melt pool. The histogram has two peaks, one at the very low grey values and the other at very high grey values (255). There is a distinctive valley between the two peaks and standard deviation is much less (36.89) as opposed to two previous images (around 90). Another image is shown in Figure 4.2b. This image is composed of a large black area as the background, an area that the grey value is increasing slowly which is the melt pool, and very little reflection. The histogram has a major difference from the previous ones which is existence of only one peak in the histogram. The maximum grey value in the image unlike the others is 236 instead of 255. The standard deviation is 17.326 which is the minimum value among

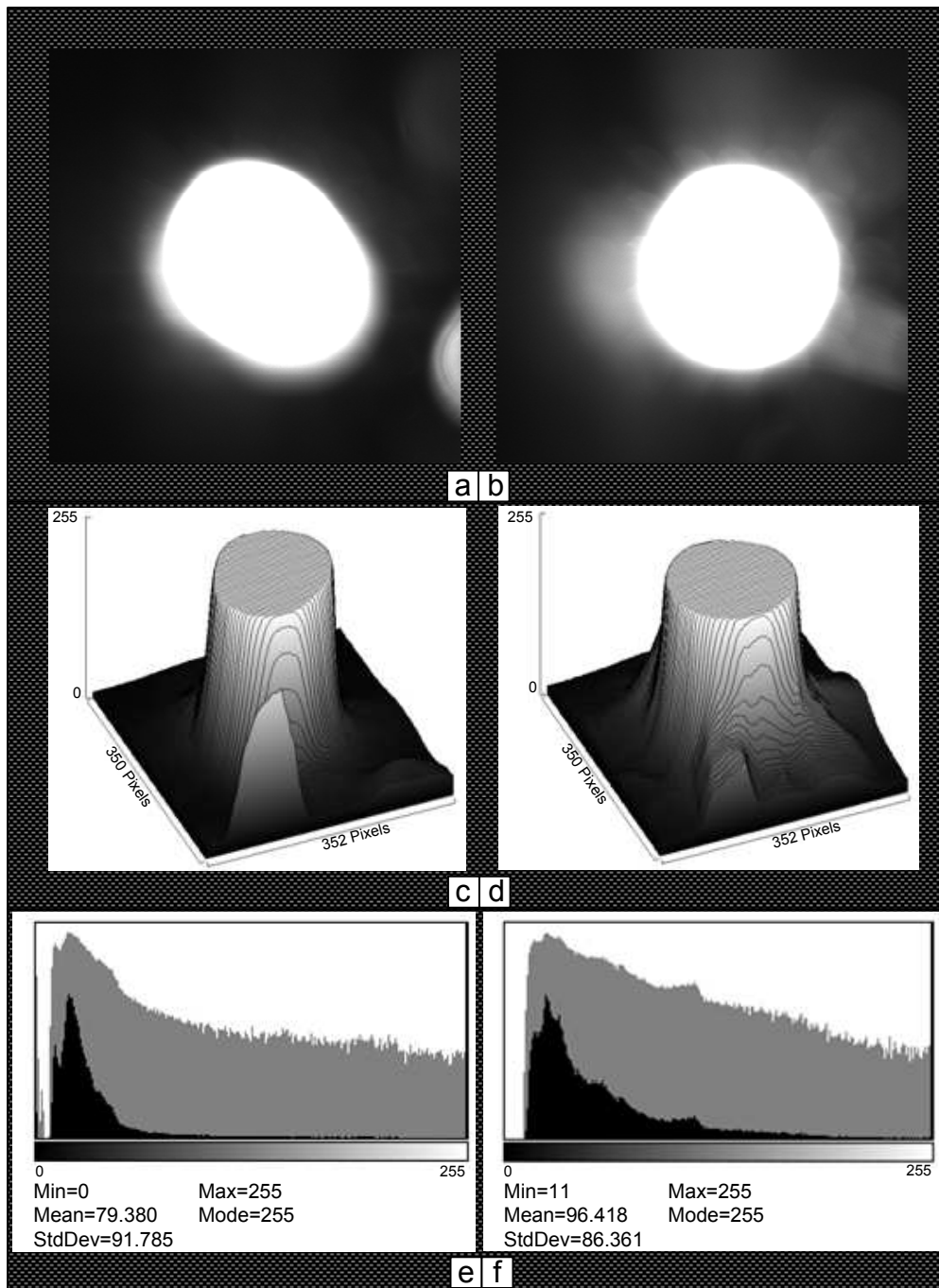


Figure 4.1: Typical types of images taken from the melt pool (part 1). a) & b) melt pool images. c) & d) corresponding surface plots of the images. e) & f) corresponding histograms along with the related statistical data of the images

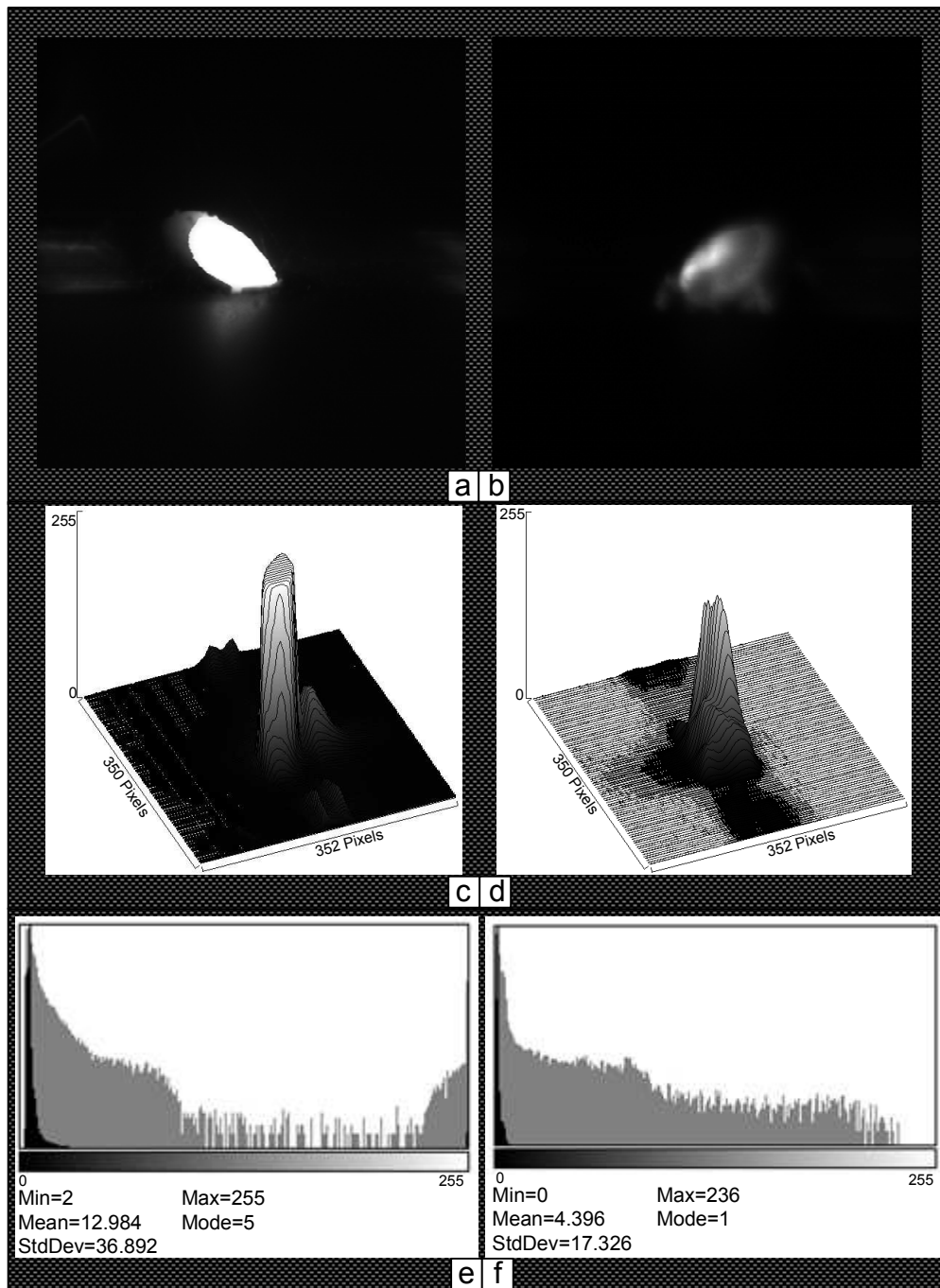


Figure 4.2: Typical types of images taken from the melt pool (part 2). a) & b) melt pool images. c) & d) corresponding surface plots of the images. e) & f) corresponding histograms along with the related statistical data of the images

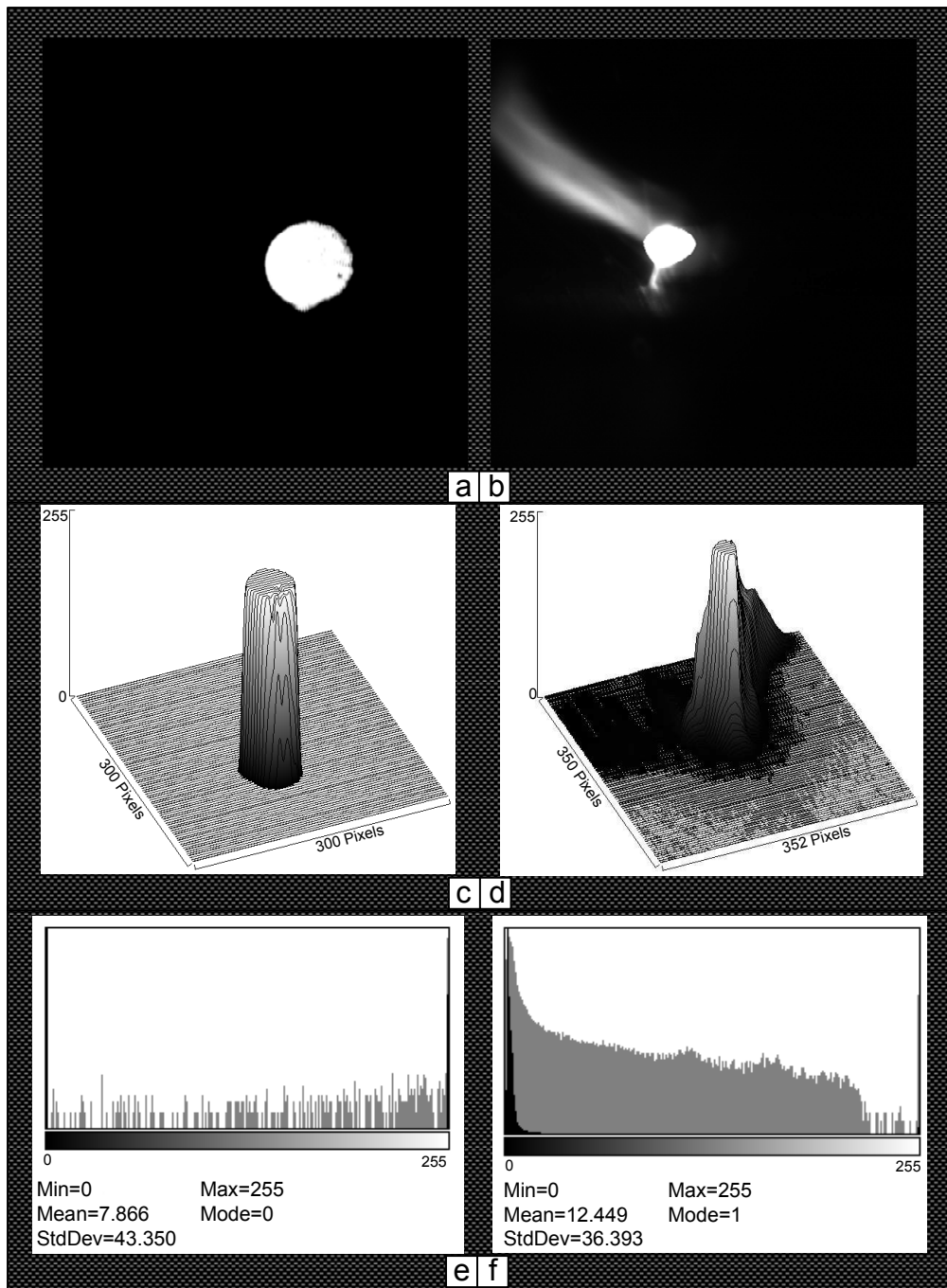


Figure 4.3: Typical types of images taken from the melt pool (part 3). a) & b) melt pool images. c) & d) corresponding surface plots of the images. e) & f) corresponding histograms along with the related statistical data of the images

the four investigated images which again is due to existence of only one peak. Figure 4.3a shows one more typical image of the melt pool. This image consists of almost only two regions, a consistent black region as the background and a white area as the melt pool. The deviation of grey values in the melt pool area is small. This fact clearly is illustrated in the surface plot of the image; the surface plot is flat plane at zero and a cylinder with the height of 255. The histogram includes a wide valley between the two peaks at both ends. The last image of these typical images of the melt pool is shown in Figure 4.3b. The image comprises a black area as the background, a white area as the melt pool, some reflection, a grey area which represents not completely solidified clad around the melt pool at the bottom and the back and a dusty area which seems is the vapor arising from the melt pool. The histogram includes two peaks at both ends, a narrow valley near the value of 255, and an area in which the frequency decreases with a slight slope along the increase in grey value.

The aforementioned description indicates that characteristics of these images vary from one to another. In fact, there are major differences between the histograms. Furthermore, for some of them the thresholding is a challenging task even if all images are considered to be the same. For example, in the image of Figure 4.1a and 4.1b, the hazy area around the melt pool could make the thresholding algorithm complicated due to the fact that the thresholding algorithm should be able to distinguish between the melt pool and the hazy area. As a result, exploiting of proper thresholding algorithm is a challenging task.

As mentioned earlier many thresholding algorithms have been developed by researchers over years. An exposition survey over image thresholding techniques can be found in [50, 51, 52, 53, 54, 55]. In these articles authors attempted to classify the current thresholding methods based upon several criteria such as the employed information. For example, Sezgin and Sankur classified the thresholding algorithms based upon the employed information into six groups [50]: “

1. histogram shape-based methods, where, for example, the peaks, valleys and curvatures of the smoothed histogram are analyzed
2. clustering-based methods, where the gray-level samples are clustered in two parts as

background and foreground (object), or alternately are modeled as a mixture of two Gaussians

3. entropy-based methods result in algorithms that use the entropy of the foreground and background regions, the cross-entropy between the original and binarized image, etc.
4. object attribute-based methods search a measure of similarity between the gray-level and the binarized images, such as fuzzy shape similarity, edge coincidence, etc.
5. the spatial methods use higher-order probability distribution and/or correlation between pixels
6. local methods adapt the threshold value on each pixel to the local image characteristics.” [50]

Haralick and Shapiro categorized the thresholding algorithms into 6 groups [55]: “

1. measurement space guided spatial clustering,
2. single linkage region growing schemes,
3. hybrid linkage region growing schemes,
4. centroid linkage region growing schemes,
5. spatial clustering schemes,
6. split and merge schemes.” [55]

The most common algorithm among these various selections of algorithms which has shown relatively good result for a wide range of image types is Otsu thresholding technique [56]. Otsu thresholding which is a statistical based thresholding technique was applied to several obtained images in laser cladding. Figure 4.4 illustrates one of the images and the binary image acquired by applying the Otsu thresholding. As shown Otsu fails to detect the melt at the presence of a flare. Several other thresholding methods also were applied to the images; however none of them were able to detect the melt pool properly.

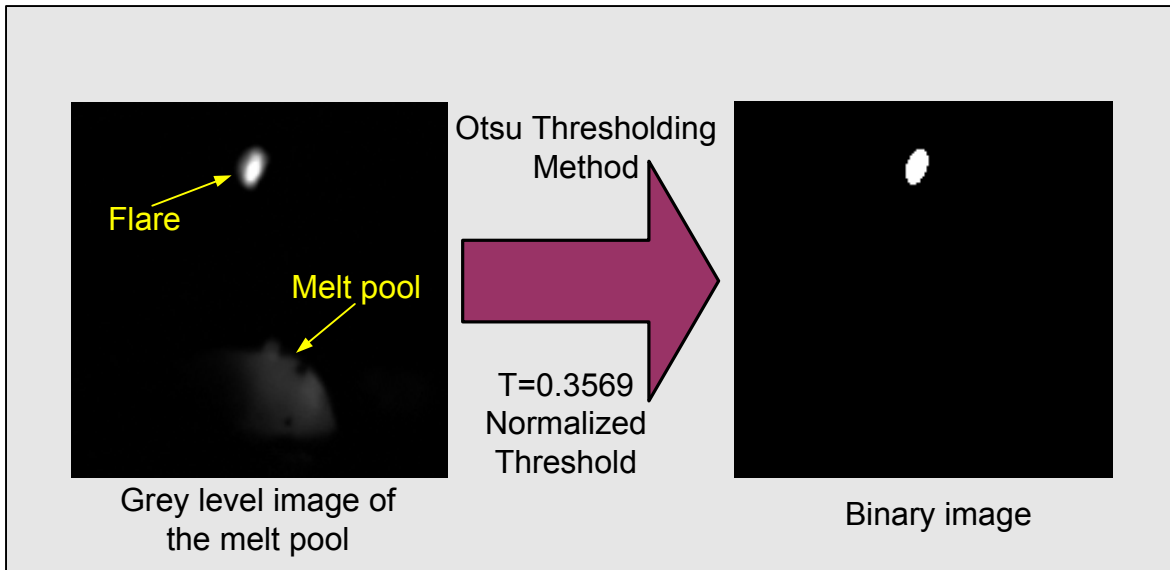


Figure 4.4: Thresholded image by applying Otsu method : Only the flare has been detected, and the melt pool completely eliminated.

The reason for this could be the fact that most of these algorithms are based on hard partitioning of the pixels into the object and background. As a result, it has been observed that performance of these algorithm is promising when the images meet the criteria on which these algorithms structured; however, when the images do not meet the criteria, the performance of the algorithms is downgraded. For instance when a thresholding method is constructed based on a specific characteristic of the histogram (e.g., geometrical distribution such as existence of valley between the peaks), the thresholding method mostly has a promising performance when applied to such characteristics. In fact, these thresholding methods are not able to respond properly to the structural features inherent in the grey distribution of images or they are not adaptive thresholding techniques. Therefore, these algorithms are called “ad hoc” algorithms. Hence, utilizing the thresholding techniques based upon the fuzzy set theory is recommended. In the following, development of two fuzzy based thresholding techniques will be investigated and the result of application of these algorithms on the obtained images will be presented.

4.3 Application of Fuzzy Set Theory to Image Thresholding

A fuzzy set A is defined by a membership function such that:

$$\mu_A(x) \in [0, 1] \tag{4.4}$$

where, A is a fuzzy set, x belongs to A with the degree of μ , $\mu_A(x)$ is the degree of attachment of x to A .

This is unlike the crisp set theory in which x either belongs to A or not. In other words, crisp set theory is a special case of fuzzy set theory in which, $\mu_A(x) \in \{0, 1\}$.

Fuzzy set can be applied to the image thresholding by dividing the image to two fuzzy sets, object O and background B . Pixels are associated by membership distribution μ_O and μ_B to O and B ; respectively, which means $\mu_O(I_{mn}) \in [0, 1]$ and $\mu_B(I_{mn}) \in [0, 1]$. Several algorithms were developed by researchers in order to find optimal threshold value T . One can find a survey of thresholding techniques exploiting fuzzy set theory in [48, 49]. A number of researchers employed the measure of fuzziness of the image space to determine optimal T and in turn to partition the image to object and background. The measure of fuzziness acquired by using different terms- entropy, index of fuzziness, index of non fuzziness, to name a few. Some others employed soft partitioning or fuzzy clustering to find the optimal threshold. Among these algorithms, one based upon measure of fuzziness and one based upon fuzzy clustering are scrutinized in the following. The result of applying these algorithms to the acquired images also will be presented.

4.4 Determination of Optimal Threshold by Minimizing the Measure of Fuzziness

In this method, two fuzzy sets should be defined, then by minimizing the measure of fuzziness of the fuzzy sets, the optimal threshold should be acquired. Fuzzy sets can be

acquired by using the relationship between each pixel grey value and average grey value of selected region [57].

Suppose [57]:

$P = [I_{mn}]_{M \times N}$ represents the image in which I_{mn} is a pixel located at (m, n) and has a discrete grey value such that: $I_{mn} \in \{0, 1, 2, \dots, L - 1\}$. P can be expressed in fuzzy sets by:

$$P = \{(I_{mn}, \mu_A(I_{mn}))\} \quad (4.5)$$

Assume that the frequency of grey value of g is $h(g)$. By selecting an arbitrary threshold value of t , the image is divided to two arbitrary regions, object and background. The average grey value of object (\bar{g}_o) and background (\bar{g}_b) is calculated by:

$$\bar{g}_o = \frac{\sum_{g=0}^t gh(g)}{\sum_{g=0}^t h(g)} \quad (4.6)$$

$$\bar{g}_b = \frac{\sum_{g=t+1}^{L-1} gh(g)}{\sum_{g=t+1}^{L-1} h(g)} \quad (4.7)$$

These values are utilized in order to define membership distribution of each pixel in these regions. By assuming triangular membership distributions, the membership distribution of the object is evaluated as:

$$\mu_o(I_{mn}) = \begin{cases} \frac{1}{1 + |I_{mn} - \bar{g}_o|/\nu} & \text{if } I_{mn} > t \\ 0 & \text{if } I_{mn} \leq t \end{cases} \quad (4.8)$$

where ν is an arbitrary number in order to keep $\mu(I_{mn})$ between 1/2 and 1 and is considered

as L in this study. Membership distribution of the background is calculated similarly:

$$\mu_b(I_{mn}) = \begin{cases} 0 & \text{if } I_{mn} > t \\ \frac{1}{1 + |I_{mn} - \bar{g}_b|/\nu} & \text{if } I_{mn} \leq t \end{cases} \quad (4.9)$$

As seen, $\mu_b(I_{mn})$ in object region is zero, likewise the $\mu_o(I_{mn})$ is zero in the background region. In fact, there is no overlap between the two selected fuzzy set. As a result, ν is selected as L to maintain the membership greater or equal to $1/2$.

4.4.1 Entropy

As mentioned earlier, many measures can be used for minimizing the measure of fuzziness. One of these proposed measures is entropy. Entropy can be defined by several functions. De Luca and Termini [58] used Shannon function to identify the entropy of a fuzzy set A :

$$E(A) = \frac{1}{n \ln 2} \sum_{i=1}^n S(\mu_A(x_i)) \quad (4.10)$$

where S is the Shannon function with definition of:

$$S(y) = -y \ln y - (1 - y) \ln(1 - y) \quad (4.11)$$

Huang and Wang [57] extended this definition to the fuzzy sets defined in the image by:

$$E(P) = \frac{1}{M \times N \ln 2} \sum_m^{M-1} \sum_n^{N-1} S(\mu_A(I_{mn})) \quad (4.12)$$

or by considering $h(g)$:

$$E(P) = \frac{1}{M \times N \ln 2} \sum_g S(\mu_A(g)) h(g) \quad (4.13)$$

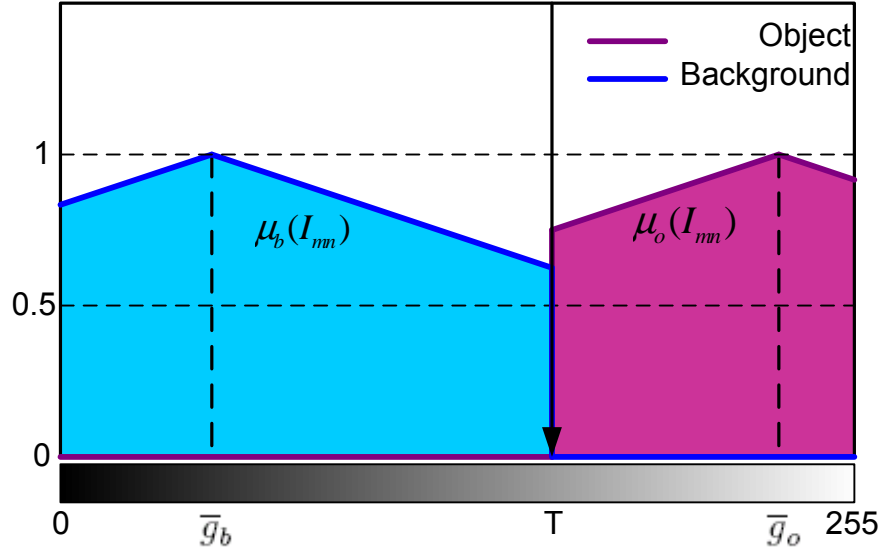


Figure 4.5: Membership distribution in typical image using triangular membership

It should be noted that Shannon function is a decreasing function between 0.5 and 1. Since $0.5 \leq \mu(I_{mn}) \leq 1$, hence $E(P)$ is a decreasing function. As a result, the maximum of $E(P)$ happens at $\mu(I_{mn}) = 0.5$. This occurs when the differences between I_{mn} and g are at maximum. In other words, the generated regions by t have large standard deviations. On the contrary, the minimum of $E(P)$ happens at $\mu(I_{mn}) = 1$, which means the differences between I_{mn} and g is 0. In this case, the generated regions by t have the minimum standard deviations. As an example suppose that the image consists of one object which only consists of one grey value, and also one background which consists of only one grey value. In that case, standard deviation of both regions would be zero. $\mu(I_{mn})$ would be one for both regions and E will be at its minimum value zero. As a result, the crispier generated regions by t would result in smaller value for E . In order to find the optimal threshold T , t is increased from 0 to 255 in increment of one, the t which make $E(P)$ minimum is selected as optimal threshold. In fact:

$$T = \{t | \min_t E(P)\} \quad (4.14)$$

The membership distribution of the generated fuzzy sets in a typical histogram has

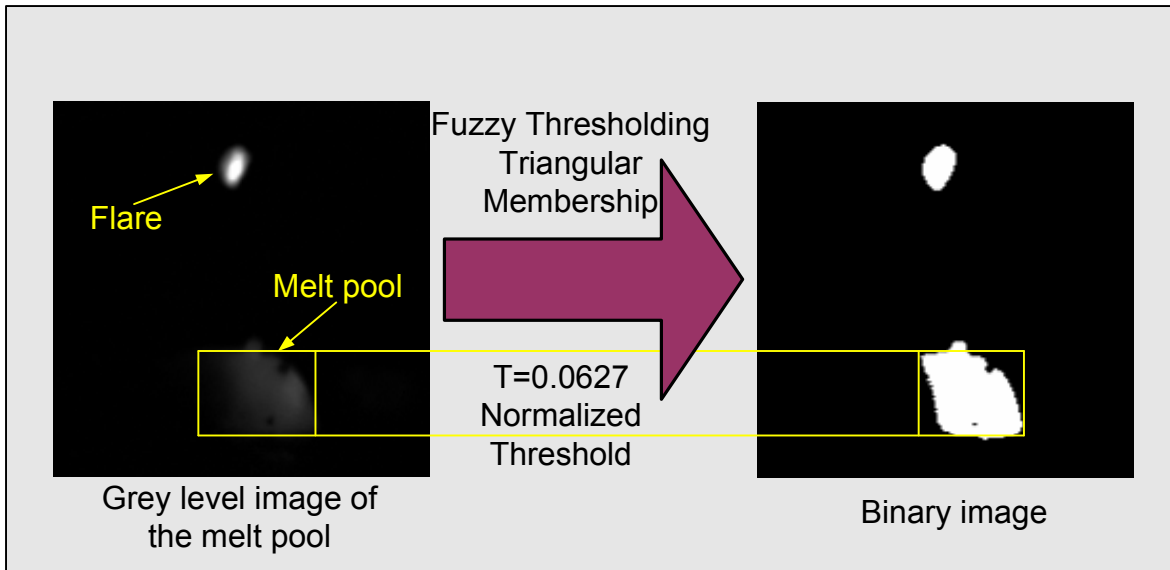


Figure 4.6: Applying minimizing the measure of fuzziness with triangular membership function to an image

shown in Figure 4.5. The algorithm was applied to the same image as Figure 4.4 which the result has shown in Figure 4.6. The figure clearly illustrate that the fuzzy method with triangular membership detected the melt pool whereas the Otsu method completely failed to detect the melt pool. Further discussion will be presented in the results and discussion section.

4.4.2 Membership Distribution Using Gaussian Membership Function

Gaussian membership function is employed instead of triangular membership in order to investigate the effect of chosen membership function on the algorithm. Gaussian membership function is defined as follows:

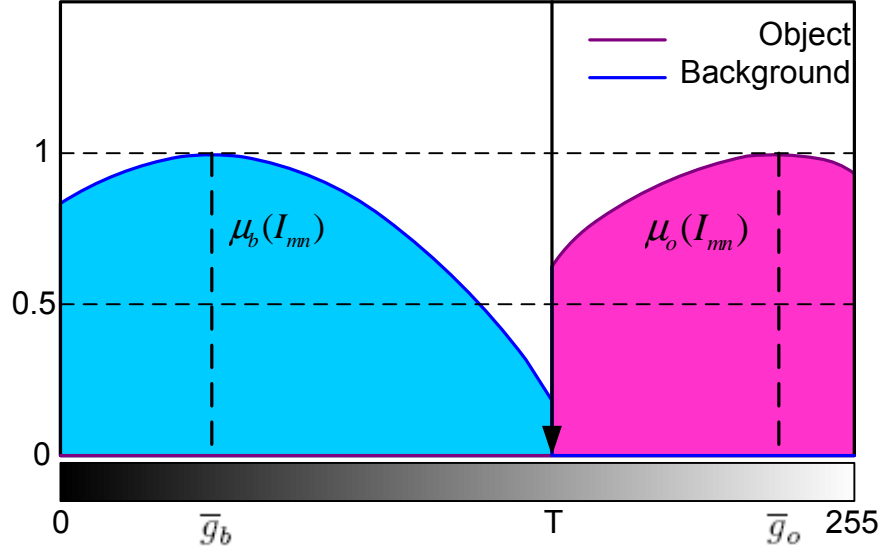


Figure 4.7: Membership distribution in a typical histogram using Gaussian membership

$$\mu_o(I_{mn}) = \begin{cases} \exp\left(\frac{-(I_{mn} - \bar{g}_o)^2}{2\sigma^2}\right) & \text{if } I_{mn} > t \\ 0 & \text{if } I_{mn} \leq t \end{cases} \quad (4.15)$$

$$\mu_b(I_{mn}) = \begin{cases} 0 & \text{if } I_{mn} > t \\ \exp\left(\frac{-(I_{mn} - \bar{g}_b)^2}{2\sigma^2}\right) & \text{if } I_{mn} \leq t \end{cases} \quad (4.16)$$

where σ is a number which makes the membership function wide or narrow and considered as $0.3 \times L$ in this study.

Figure 4.7 graphically illustrates how the above thresholding is implemented in the histogram region. The algorithm with Gaussian membership function was employed for melt pool detection of the same image shown in Figure 4.4 and 4.6. The result is shown in

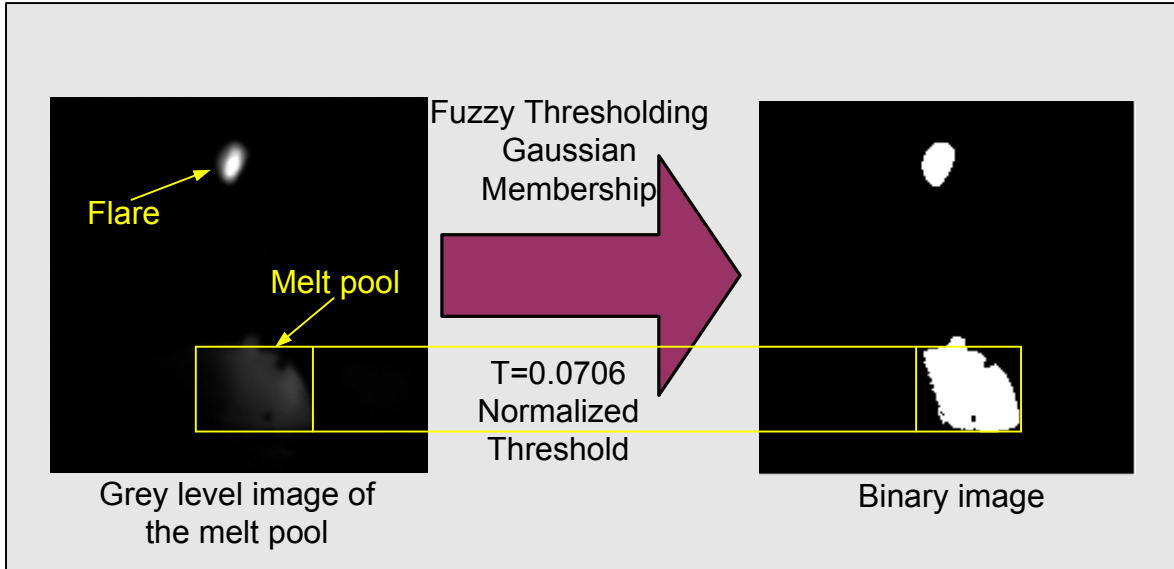


Figure 4.8: Applying minimizing the measure of fuzziness with Gaussian membership function to an image

Figure 4.8. The result of the algorithm with Gaussian membership function seems better than the algorithm with triangular membership function. Further discussions will be given in the results and discussion section.

4.4.3 Membership Distribution Using Generalized Bell Membership Function

Generalized Bell membership function is also applied to further investigate the effect of the membership function type. Generalized bell is an extension to the Cauchy probability distribution. The Cauchy probability distribution $C : R \rightarrow [0, 1]$ is defined as:

$$C(x) = \frac{1}{1 + \frac{\|x - \alpha\|^\beta}{\gamma}} \quad (4.17)$$

where $\alpha \in R$, $\beta \geq 0$, $\gamma > 0$. α is the center of curve, γ makes the curve wide or narrow,

and β defines the smoothness of function. In fact γ and β determine the fuzziness of the membership function. Generalized Bell membership function was applied to define the membership distribution of object and background as:

$$\mu_o(I_{mn}) = \begin{cases} \frac{1}{(1 + |\frac{I_{mn} - \bar{g}_o}{256}|)^{2B}} & \text{if } I_{mn} > t \\ 0 & \text{if } I_{mn} \leq t \end{cases} \quad (4.18)$$

$$\mu_b(I_{mn}) = \begin{cases} 0 & \text{if } I_{mn} > t \\ \frac{1}{(1 + |\frac{I_{mn} - \bar{g}_b}{256}|)^{2B}} & \text{if } I_{mn} \leq t \end{cases} \quad (4.19)$$

where, $B \geq 0$ determines the grade of fuzziness of the membership function. In this study, B is considered as 1.5. Figure 4.9 shows a typical histogram with generalized bell curve membership function as membership distributions. As it is seen, the area around the average of each region is almost a straight line and by getting far from the average the curve is going down with a slight slope. By having a look at triangular, Gaussian, and bell, it reveals that, from triangular to bell, curves get wider and the slope is decreasing, in fact the area under the curves becomes larger. In other words, the generalized bell function has greatest fuzziness among the three, and triangular has the minimum.

The algorithm with generalized bell membership function was applied to the same image as Figure 4.4, 4.6, and 4.8. The result has been presented in Figure 4.10. More results will be presented in the results and discussion section.

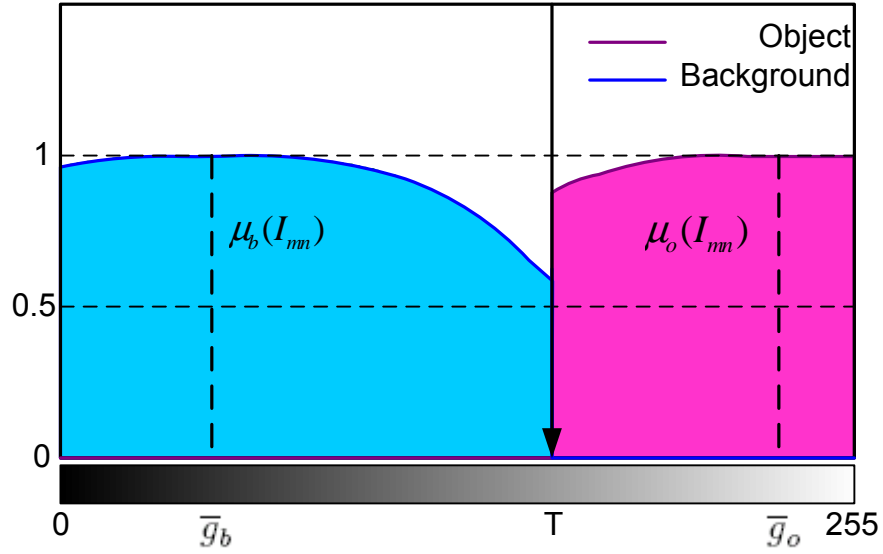


Figure 4.9: Membership distribution using generalized bell curve membership function

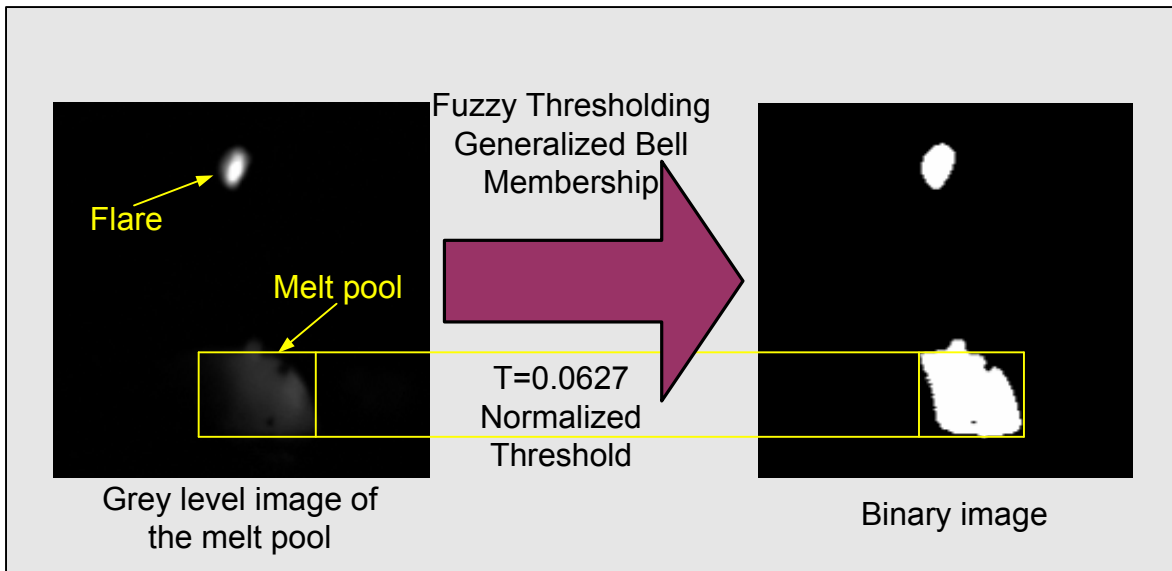


Figure 4.10: Applying minimizing the measure of fuzziness with generalized bell membership function to an image

4.4.4 Employment of Look Up Table

The above-mentioned algorithm has been used for different melt pool images. In spite of the good results, the algorithm is slow. Fuzzy thresholding technique using Gaussian membership function is about 19 times slower than Otsu method. The algorithm is very crucial to be fast, considering the fact that it is ultimately intended to be implemented in the laser cladding process in order to detect the melt pool in a real-time fashion. In order to address this issue, the following modification has been made to lessen the computation time of the algorithm.

Without affecting the performance of algorithm it can be assumed:

$$\bar{g}_o = \mathbf{int} \left[\frac{\sum_{g=0}^t gh(g)}{\sum_{g=0}^t h(g)} \right] \quad (4.20)$$

$$\bar{g}_b = \mathbf{int} \left[\frac{\sum_{g=t+1}^{L-1} gh(g)}{\sum_{g=t+1}^{L-1} h(g)} \right] \quad (4.21)$$

As a result, \bar{g}_o and \bar{g}_b are assigned integer numbers between 0 and 255. On the other hand, I_{mn} is an integer number between 0 and 255, hence $I_{mn} - \bar{g}$ is an integer number and we have $0 \leq I_{mn} - \bar{g} \leq 255$. Therefore, for the different values of $I_{mn} - \bar{g}$ a look up table has been constructed offline in which $I_{mn} - \bar{g}$, $\mu(g)$, and $S(\mu(g))$ were stored respectively.

In other words, the membership functions and Shannon function are calculated offline and recalled from the look up table during the online process. These modifications made the fuzzy threshold with Gaussian membership function about 20 times faster than before or 5 percent faster than Otsu method which is quite promising.

4.5 Determination of Optimal Threshold by Fuzzy C-Means Clustering

Data clustering can be defined as partitioning of a group of data points into a number of subgroups (clusters) based upon closeness and similarity between members of each cluster, in fact clustering is grouping n data points into k clusters. In order to have a scale to measure degree of closeness or similarity a distance function is exploited, in other words distance function reveals the degree of closeness between members of a subgroup. There are several distance functions which consider different features as the measure of closeness and in turn measure the degree of closeness from different point of views such as Euclidean and Hamming function.

Several data clustering methods were developed during the past decades. These methods may be divided into two major categories:

- Hierarchical
- Objective function based clustering

In Hierarchical clustering, first each data point is considered as a cluster, and then in each iteration two closest clusters are joined and this continues until a threshold value is reached. Hierarchical clustering is common due to its simplicity, however because of its iterative character it is time consuming.

In the Objective function based clustering, data points are divided into a number of subgroups and then minimization of an objective function is sought to determine one configuration among all the possible partitions. Among different objective function based clustering, C-Means clustering (HCM) has drawn much attention and arisen in a multitude of applications. In C-Means clustering minimization of a cost function by finding center of each cluster is sought as follows [59]:

$$Q = \sum_{i=1}^k q_i = \sum_{i=1}^k \sum_{j=1}^n u_{ij} d(x_j, c_i)^2 \quad (4.22)$$

where,

q_i is the cost function in group i ,

c_i is the center for cluster i ,

$d(x_j, c_i) = \|x_j - c_i\|$ is a the distance function between each vector (data point) and center of the cluster,

$U = [u_{ij}]_{k \times n}$ is the similarity, partition or membership matrix.

u_{ij} is 1 when x_j belongs to cluster i and is 0 when it does not. A data point belongs to the cluster which its center has minimum distance to it among all centers. In fact:

$$u_{ij} = \begin{cases} 1 & \text{if } \|x_j - c_i\|^2 = \min_i (\|x_j - c_i\|^2) \\ 0 & \end{cases} \quad (4.23)$$

It should be noted that each data point only belongs to one cluster and as a result:

$$\sum_{i=1}^k u_{ij} = 1 \quad \forall j = 1, \dots, n \quad (4.24)$$

$$\sum_{i=1}^k \sum_{j=1}^n u_{ij} = n \quad (4.25)$$

C-Means clustering algorithm can be described as:

Step 1: Choose k data points randomly as cluster centroid.

Step 2: Calculate partition matrix by and assign $n - k$ remained data points to k chosen clusters.

Step 3: Calculate the cost function from 4.22. Stop if the cost function is below a threshold value or if the difference between the current cost function and the one from the previous iteration is below a threshold value.

Step 4: calculate new cluster centers and go to step 2.

4.5.1 Fuzzy C-Means Clustering (FCM)

Fuzzy C-Means Clustering (FCM) is generalized form of Hard C-Means Clustering (HCM) in a fuzzy fashion. The main difference between HCM and FCM is in HCM, each data point only belongs to one cluster, whereas in FCM each data point can be associated with several clusters with different degree of membership between 0 and 1. As a result, u_{ij} (membership degree of data point j with respect to cluster i) has these properties [48, 59]:

$$u_{ij} \in [0, 1] \quad (4.26)$$

$$0 < \sum_{j=1}^n u_{ij} < n \quad \forall i = 1, \dots, k \quad (4.27)$$

$$\sum_{i=1}^k u_{ij} = 1 \quad \forall j = 1, \dots, n \quad (4.28)$$

The objective function is:

$$Q = \sum_{i=1}^k \sum_{j=1}^n u_{ij}^m d(x_j, c_i)^2 \quad (4.29)$$

where,

c_i is the center of fuzzy cluster i ,

$d(x_j, c_i) = \|x_j - c_i\|$ is Euclidean distance between data point j and center of group i ,

$m = [1, \infty)$ is the weighting parameter.

m controls the amount of fuzziness. When $m = 1$ the formula becomes equivalent to the hard C-Means clustering. m is usually considered between 2 and 7. In order to minimize Q of Equation (4.29), c_i and u_{ij} should satisfy these equations [60]:

$$c_i = \frac{\sum_{j=1}^n u_{ij}^m x_j}{\sum_{j=1}^n u_{ij}^m} \quad \forall i = 1, \dots, k \quad (4.30)$$

$$u_{ij} = \frac{1}{2 + \sum_{p=1}^k \left(\frac{d_{ij}}{d_{pj}}\right)^{m-1}} \quad \forall i = 1, \dots, k \quad \forall j = 1, \dots, n \quad (4.31)$$

where $d_{ij} = d(x_j, c_i) = \|x_j - c_i\|$.

The algorithm can be described as:

Step 1: Choose membership matrix randomly in such a way that Equations (4.26), (4.27), and (4.28) are satisfied.

Step 2: Calculate fuzzy cluster centers $c_i, \quad i = 1, \dots, k$ by Equation (4.30).

Step 3: Calculate the cost function by Equation (4.29). Stop if the cost function is below a threshold value or if the difference between the current cost function and the one from the previous iteration is below a threshold value.

Step 4: Update the membership matrix, U , by Equation (4.31) and go to step 2.

It should be noted that the algorithm can also be processed by first initialization of cluster centers.

4.5.2 Computation of Optimal Threshold by FCM

Image segmentation can be considered as a special case of clustering in which the clustering is performed in the domain of image. The grey value of each pixel can be considered as a one dimensional data point. Suppose $P = [I_{mn}]_{M \times N}$ represents the image in which I_{mn} is a pixel located at (m, n) and has a discrete grey value such that: $I_{mn} \in \{0, 1, 2, \dots, L-1\}$. Also let $(g, h(g))$ be the histogram of image. Number of clusters, k , is considered as 2 corresponding to object and background. Since u_{ij} is membership degree of data point j to cluster i , it can be shown by: $u_{ij} = \mu_i(g)$ then the Equation (4.29) becomes [48]:

$$Q = \sum_{i=1}^2 \sum_{g=0}^{L-1} h(g) \mu_i(g)^m d(g, c_i)^2 \quad (4.32)$$

Also, Equation (4.30) becomes:

$$c_i = \frac{\sum_{g=0}^{L-1} h(g) \mu_i(g)^m g}{\sum_{g=0}^{L-1} h(g) \mu_i(g)^m} \quad \forall i = 1, 2 \quad (4.33)$$

where c_1 and c_2 correspond to center of the fuzzy cluster representing the background c_b and center of the fuzzy cluster representing the object c_o , respectively.

Membership distribution by Equation (4.31) becomes:

$$u_{ij} = \mu_i(g) = \frac{1}{\sum_{p=1}^2 \left(\frac{d_{ig}}{d_{pg}}\right)^{\frac{2}{m-1}}} \quad \forall i = 1, 2 \quad \forall g = 0, 1, \dots, L-1 \quad (4.34)$$

since $i = 2$ corresponds to object cluster:

$$\mu_o(g) = \frac{1}{\sum_{p=1}^2 \left(\frac{d_{2g}}{d_{pg}}\right)^{\frac{2}{m-1}}} = \frac{1}{\left(\frac{d(g, c_2)}{d(g, c_1)}\right)^{\frac{2}{m-1}} + \left(\frac{d(g, c_2)}{d(g, c_2)}\right)^{\frac{2}{m-1}}} \quad \forall g = 0, 1, \dots, L-1 \quad (4.35)$$

then:

$$\mu_o(g) = \frac{1}{\left(\frac{d(g, c_o)}{d(g, c_b)}\right)^{\frac{2}{m-1}} + 1} \quad \forall g = 0, 1, \dots, L-1 \quad (4.36)$$

considering Equation (4.27) and since there are 2 clusters:

$$\mu_b(g) = 1 - \mu_o(g) \quad \forall g = 0, 1, \dots, L-1 \quad (4.37)$$

As a result, the algorithm can be described as:

Step 1: Choose membership distributions $\mu_o(g)$ and $\mu_b(g)$ randomly in such a way that Equations (4.26), (4.27), and (4.28) are satisfied.

Step 2: Calculate fuzzy cluster centers c_b and c_o by Equation (4.33).

Step 3: Calculate the cost function by Equation (4.32). Stop if the cost function is below a threshold value or if the difference between the current cost function and the one from the previous iteration is below a threshold value.

Step 4: Update the membership distributions $\mu_o(g)$ and $\mu_b(g)$ by Equations (4.36) and (4.37) and go to step 2.

c_o and c_b computed by the algorithm are employed to calculate the optimal threshold. Jawahar et. al. [48] showed that for a unique point between c_o and c_b , $\mu_b(g)$ and $\mu_o(g)$ are equal, and this point has the same distance to c_b and c_o . As a result:

$$T = \frac{c_b + c_o}{2} \quad (4.38)$$

In this study m was considered as 2. Figure 4.11 graphically illustrates how the above algorithm is implemented in the histogram for $m = 2$. As seen in the figure, T is equidistant from c_o and c_b , also we have: $\mu_b(T) = \mu_o(T) = 0.5$.

The algorithm was applied to the same image as Figures 4.4, 4.6, 4.8, and 4.10. The result is presented in Figure 4.12. More results will be presented in the results and discussion section.

4.6 Results and Discussion

To investigate the performance of the aforementioned algorithms, several experiments were conducted using the apparatus shown in Figure 3.10. Two cameras of the proposed trinocular CCD-based optical detectors were installed into the processing head with 120°degrees apart from each other, as explained in Chapter 3. Images of the melt pool were captured by UNIQ UP-600CL digital cameras at a rate of 10Hz on a QNX 6.3 platform (Pentium 4, 2.6 GHz processor). A Band pass filter centered at 700 nm and a number 4 neutral intensity filter were added to each camera. During the course of the experiments, all process parameters except the velocity were kept constant as the laser frequency was set to 90 Hz, laser pulse duration to 3.0 ms , and laser pulse energy to 4 J/pulse. Stainless steel powder

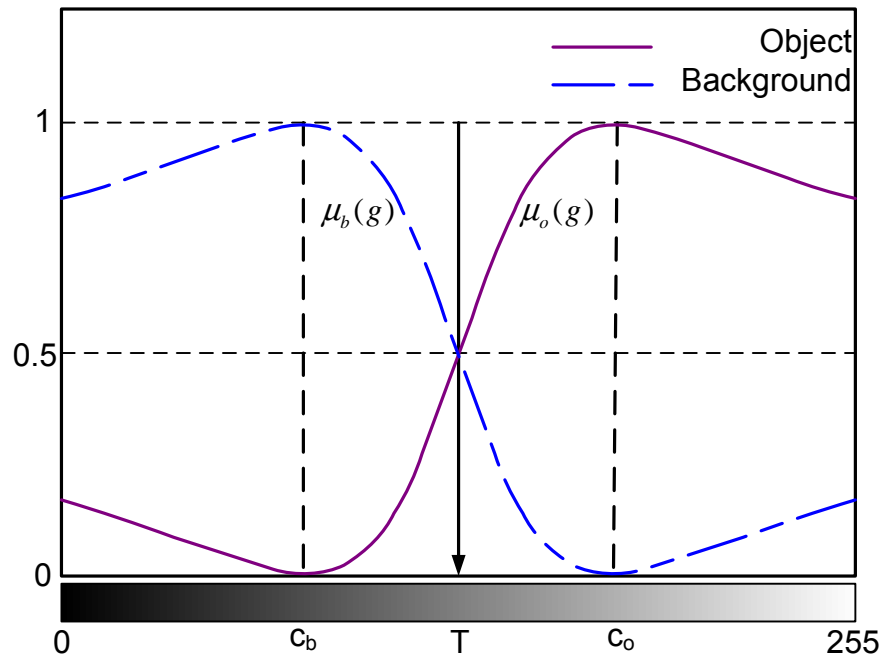


Figure 4.11: Membership distributions in a histogram by applying FCM method

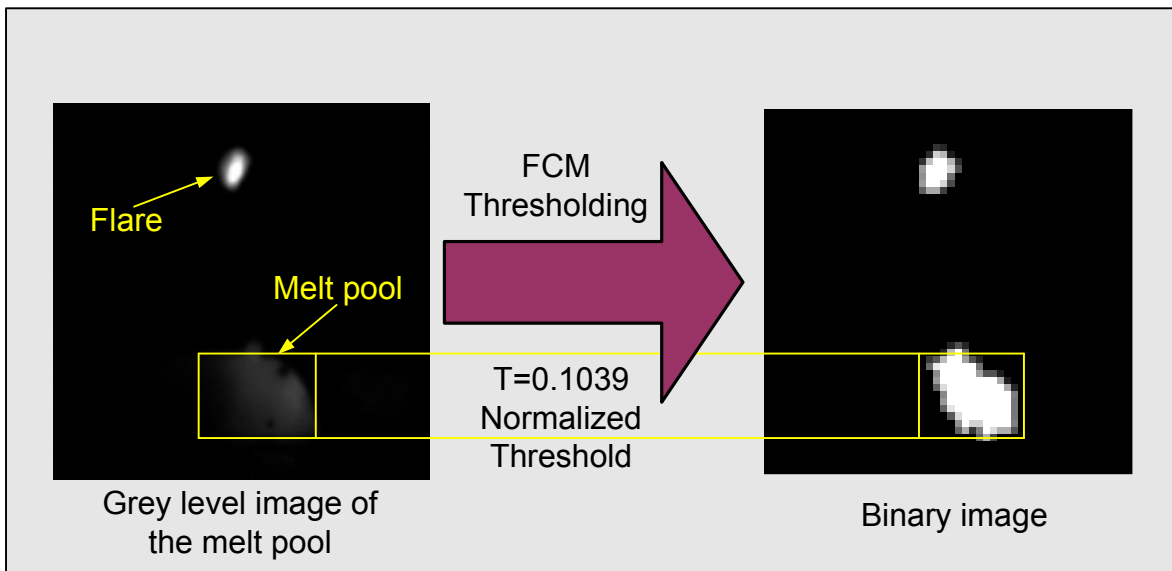


Figure 4.12: Application of FCM thresholding to one image

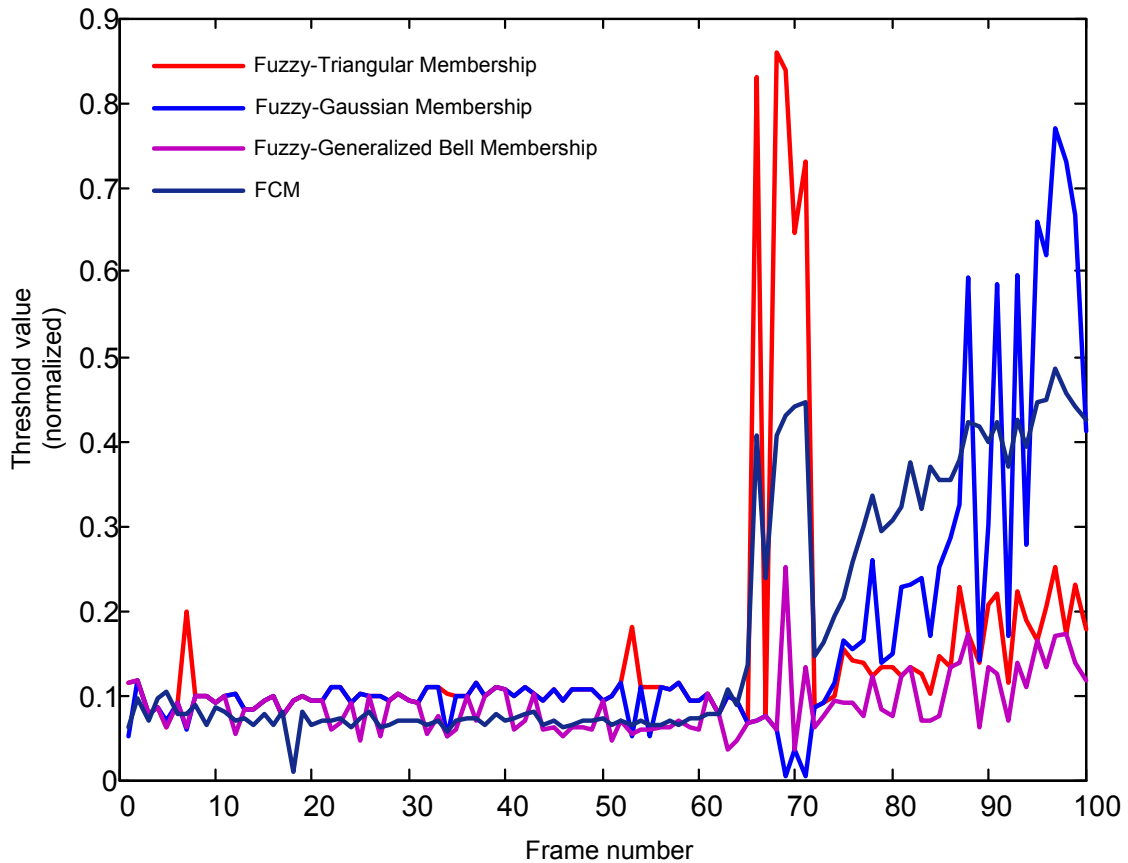


Figure 4.13: A comparison of threshold levels obtained through the aforementioned algorithms for 100 of the acquired images during the experiments

(303L) was fed at a rate of 2 g/min through the powder feeder's lateral nozzle. The process scanning speed was being changed between 0.5 mm/sec to 3 mm/sec.

The algorithms, fuzzy thresholding with triangular membership function, fuzzy thresholding with Gaussian membership function, fuzzy thresholding with generalized bell membership function, and fuzzy c-means thresholding were applied to the captured images of the melt pool during the course of the experiments. Figure 4.13 presents the acquired threshold values through each algorithm for 100 images. It can be observed that the results of these algorithms in most cases are close; however in some cases the results are drastically different. This can be observed, where for the first 65 frames, in most of the cases

the threshold values are between 0.05 and 0.15, while the differences between the threshold values for the last 35 frames are much larger. However, it should be noted that small change in the threshold value may lead to considerable changes in the binarized image. Many obtained images through the course of experiments were scrutinized by comparing the results of the algorithms. The results can be summarized as follows:

The results can be summarized as follows:

- Unlike Otsu thresholding techniques, fuzzy thresholding with different membership functions and FCM thresholding, are able to reasonably detect the melt pool;
- In most cases, the results of fuzzy thresholding and FCM thresholding are relatively identical;
- Depending on the case, different algorithms will provide the best result, in other words one algorithm doesn't provide the best result for all cases;
- Among different membership functions of fuzzy thresholding, Gaussian membership function offers the best results, almost in all cases;
- The results of fuzzy thresholding with Gaussian membership and FCM in the most cases are almost identical. However in some cases fuzzy thresholding with Gaussian provides better results and in some FCM. Overall, the results of FCM are slightly better;
- For the interest of processing speed, FCM suffers from lower processing speed compare to fuzzy thresholding (different membership functions) with implementation of look-up table. The fuzzy thresholding with Gaussian membership with implantation of look-up table is about 23 times faster than FCM thresholding;
- Fuzzy thresholding with Gaussian membership function due to good results and high speed processing can be considered for implementing in controller.

A few of the images along with the corresponding detected melt pool resulted by these algorithms are illustrated in Figures 4.14 and 4.15. In Figures 4.14 and 4.15, the first row

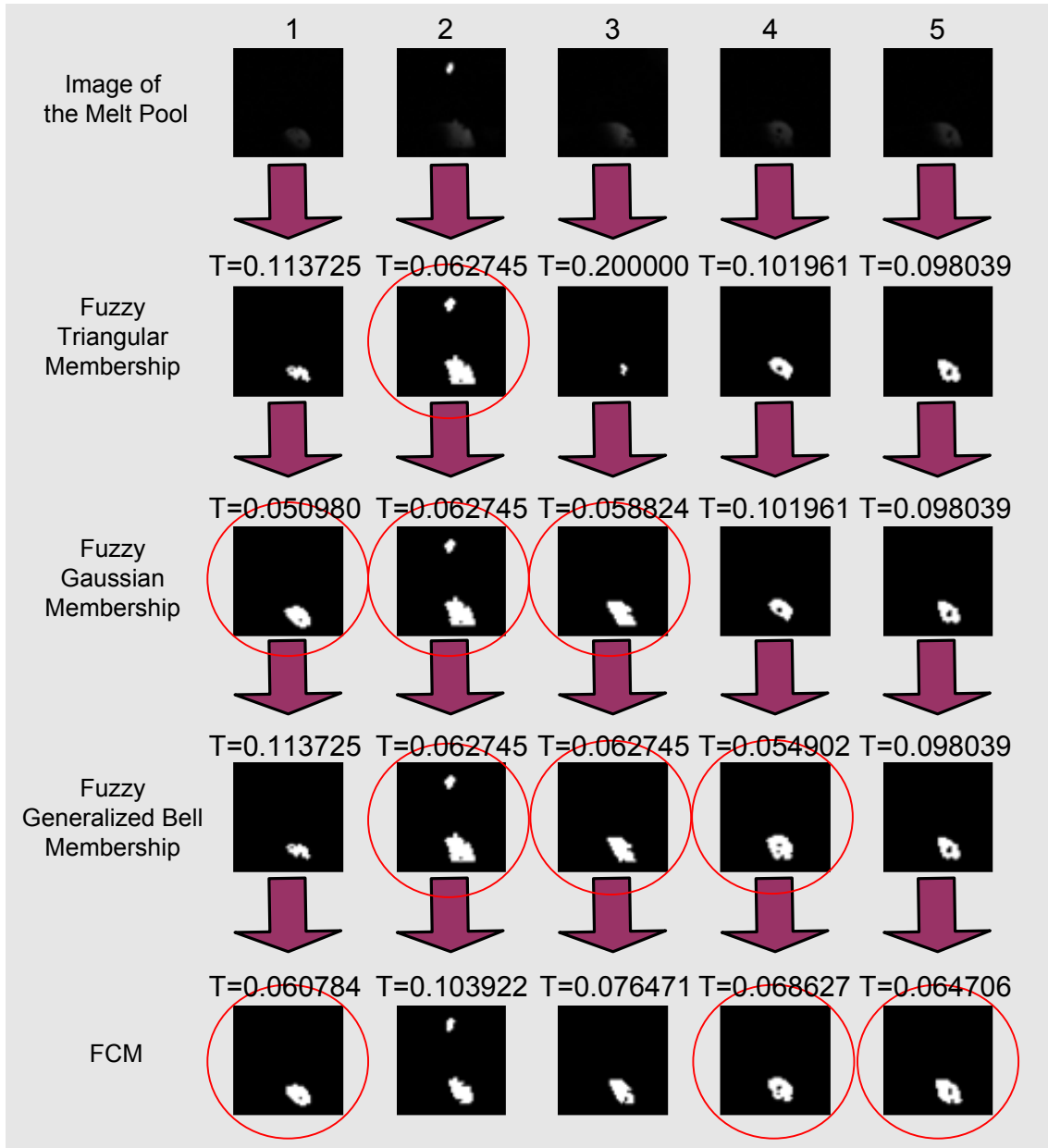


Figure 4.14: Obtained thresholded images through the aforementioned algorithms for 5 images selected through many images as a sample (first part). Circled results show the better outputs among the four results.

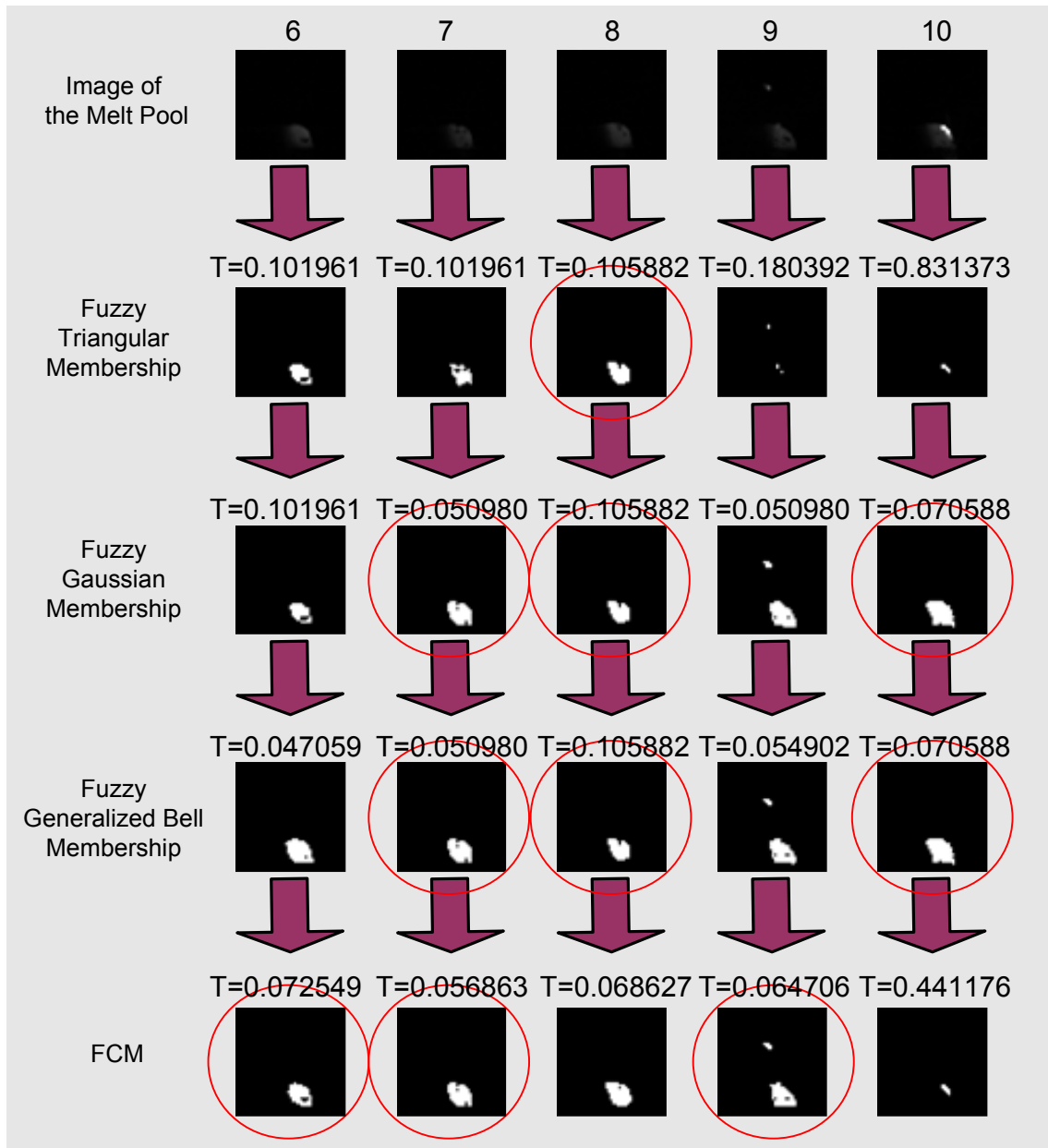


Figure 4.15: Obtained thresholded images through the aforementioned algorithms for 5 images selected through many images as a sample (second part). Circled results show the better outputs among the four results.

is the original images, the second row is the detected melt pools by fuzzy thresholding through triangular membership function, the third row is the detected melt pools by fuzzy thresholding through Gaussian membership function, the fourth row is the detected melt pools by fuzzy thresholding through generalized bell membership function, and the fifth row is the detected melt pool through fuzzy c-means thresholding. It should be noted that, these images were selected among many images to show that one algorithm always is not able to provide the best result. The best result of the four algorithms is marked by a circle around it, and where two or more algorithms provide the best results, all of them are circled.

Chapter 5

Feature Tracking Algorithms

In this chapter, extraction of features from the detected borders of the melt pool images and prediction of the clad height using these features will be discussed. Also, experimental verification in order to evaluate the validity of the developed model will be presented and discussed.

5.1 Image Transformation

As mentioned earlier, there is a relative motion between the cameras and the clad trajectories. As a result, any analysis of two images obtained from the two cameras is subject to the angle of cameras with respect to the horizontal plane. As a result, the images are first projected on a reference plane in order to be analyzed. In order to project the images on a reference plane, a perspective transform estimation approach is used [61, 62, 63]. This technique maps a quadrilateral from a plane coordinate system to another (see Figure 5.1) by the use of a perspective transformation. The perspective transformation can be represented by the matrix equation $P = Hq$, where, q represents the coordinates in the image plane, P represents the coordinates in the work plane, and H is a homogeneous transformation from the image plane to the work plane. This equation can be manipulated to represent the nonlinearities involved in the perspective projection such that it becomes:

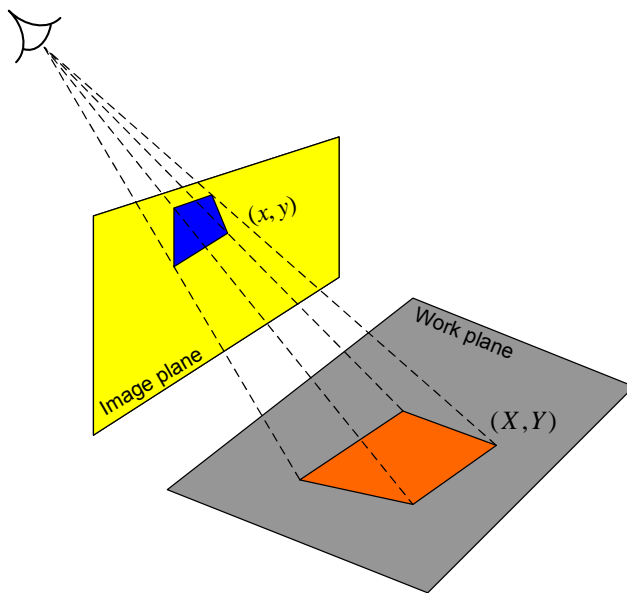


Figure 5.1: Perspective transformation: transformation of coordinates from the image plane to the world plane

$$\begin{Bmatrix} XW \\ YW \\ W \end{Bmatrix} = \begin{bmatrix} a & b & c \\ d & e & f \\ g & h & 1 \end{bmatrix} \begin{Bmatrix} x \\ y \\ 1 \end{Bmatrix} \quad (5.1)$$

where, H , the homogeneous transformation matrix, is represented by the constants a to h . Also, W is given by the following equation:

$$W = gx + hy + 1 \quad (5.2)$$

Arranging into a matrix form, one can obtain a linear equation for the unknown parameters of the homogeneous transformation in the form of $A\lambda = B$, where

$$A = \begin{bmatrix} x & y & 1 & 0 & 0 & 0 & -Xx & -Xy \\ 0 & 0 & 0 & x & y & 1 & -Yx & Yy \end{bmatrix} \quad (5.3)$$

$$\lambda = \left[a \ b \ c \ d \ e \ f \ g \ h \right]^T \quad (5.4)$$

$$B = \begin{bmatrix} X \\ Y \end{bmatrix} \quad (5.5)$$

This equation can be solved by a least squares optimization method. With eight unknown parameters in λ , one requires 8 data points, or 4 pairs of coordinates, for an exact solution. It should be noted that for each new pair of coordinates, the A and B matrices are increased by two rows, following the convention of Equations 5.3 to 5.5. The resulting linear equation may be solved using of the pseudo-inverse approach as:

$$\lambda = (A^T A)^{-1} A^T B \quad (5.6)$$

In order to obtain the transformation matrices, four pairs of coordinates on the image plane are mapped to their corresponding points on the work plane as shown in Figure 5.1. These matrices were then used for the projection of images on the work plane in which merging and analysis of the images can be directly performed.

As an example, Figure 5.2a depicts two typical images grabbed by two cameras (i.e., 1 and 2). These two images are first converted to binary (Figure 5.2b) and then the borders of the segmented melt pool are detected (Figure 5.2c). The projected detected borders are depicted in Figure 5.2d. As seen in Figure 5.2d, the front edge of the projected border, which is faced toward the cameras are real and the other side of the border is faked as affected by the shadow generated by the clad height. This fact is shown in Figure 5.3, in which the shadowing length is a function of the clad height and the clad cross section profile. Since the shape of the clad's cross section profile, shown in Figure 5.3, is unknown and varies over the process, calculating the clad height is not analytically applicable. Therefore, this fact requires us to use a soft computing technique (i.e., neural network) to be trained through the collected data presenting the features of the images. As a result, the following feature tracking module is proposed to not only obtain rich data from the projected borders but also reduce the number of inputs to the neural network.

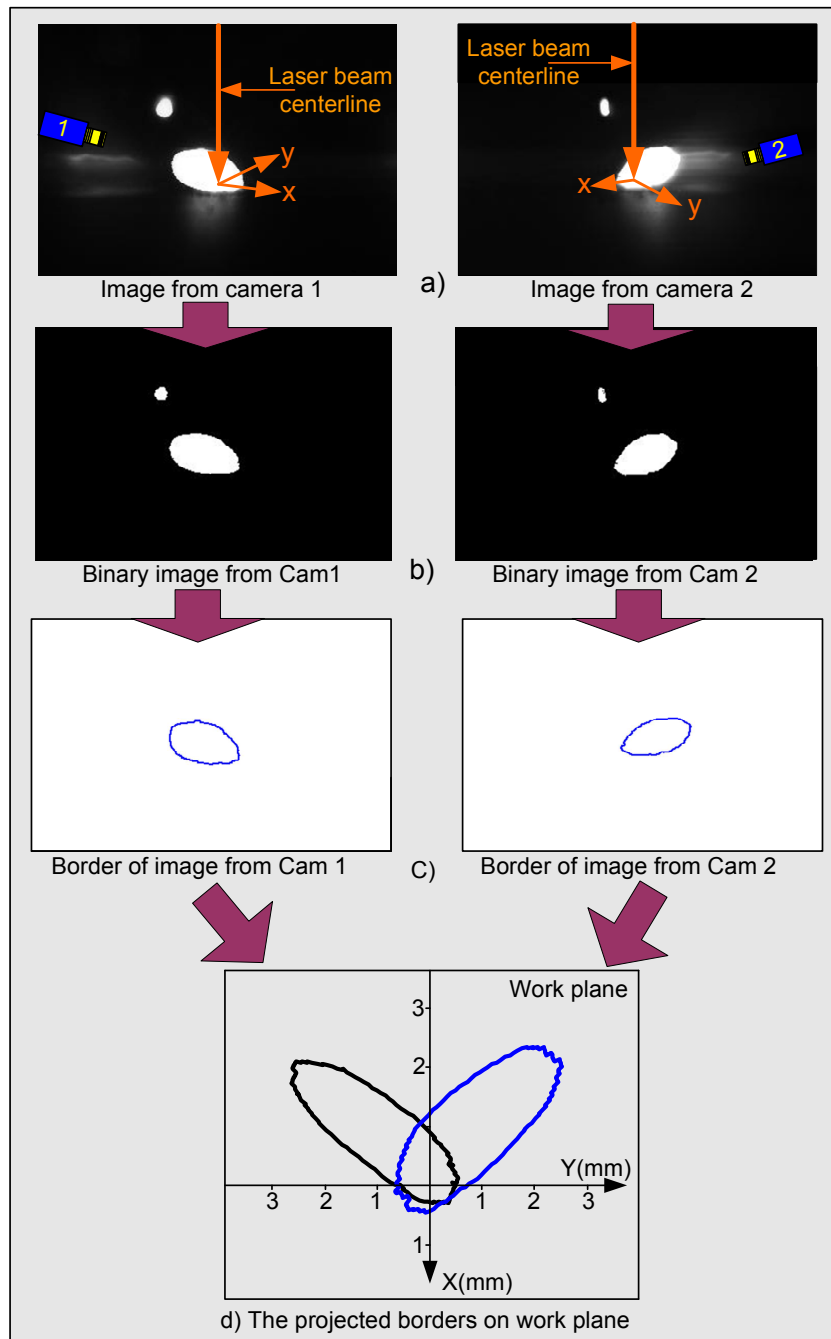


Figure 5.2: Typical projected images on the reference plane: a) Typical images from camera 1 and 2, b) Binarized images, c) Detected border of the melt in each image, d) The projected melt pool border images on the work plane

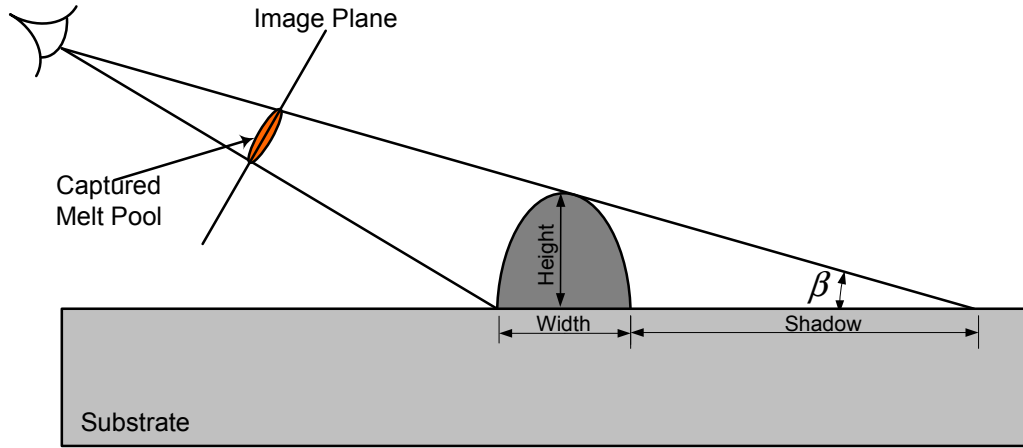


Figure 5.3: A schematic view of projection of the melt pool on the reference plane

5.2 Image Feature Tracking Module

Minimization of the number of inputs and the reduction of the computational time call for tracking special features in the projected images. As seen in Figure 5.2d, the projected borders of the melt pool have an elliptical form. Hence, each projected image can be parameterized in terms of ellipse's major and minor axes (A and B), and the angle between the major diameter and a datum line (i.e., α) as shown in Figure 5.4.

5.2.1 Extracting the ellipse major and minor diameters and α from the projected borders

In order to extract A , B , and α , it is needed to fit an ellipse to the border of each projected image. This fitting can be carried out by Fitzgibbon's approach, which is based on least squares minimization technique [64]. In general, an ellipse can be written by an implicit second order polynomial as

$$F(x, y) = a_1x^2 + a_2xy + a_3y^2 + a_4x + a_5y + a_6 = 0 \quad (5.7)$$

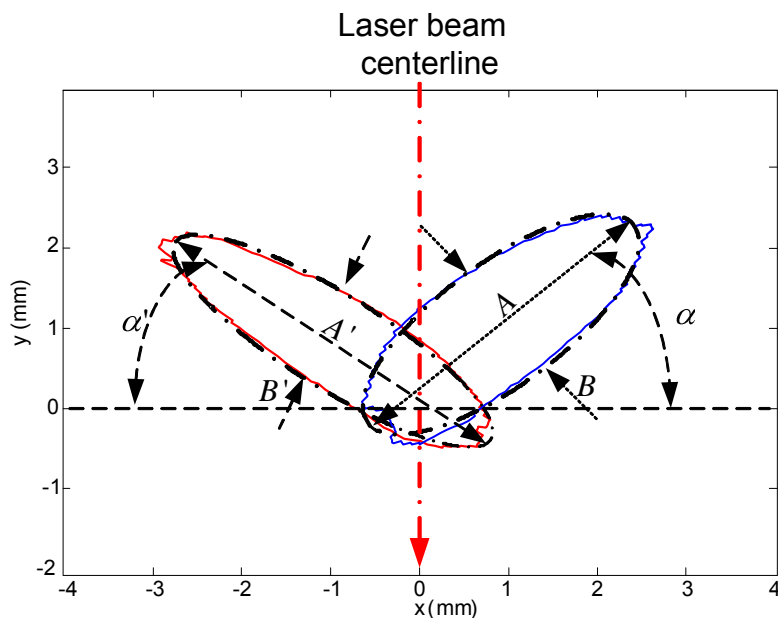


Figure 5.4: Selected features in the images after fitting ellipses

where a_1 to a_6 are coefficients of the ellipse and (x, y) are coordinates of points which form the ellipse. These coefficients can be presented by the following vectors

$$\mathbf{a} = \begin{bmatrix} a_1 & a_2 & a_3 & a_4 & a_5 & a_6 \end{bmatrix} \quad (5.8)$$

$$\mathbf{x} = \begin{bmatrix} x^2 & xy & y^2 & x & y & 1 \end{bmatrix} \quad (5.9)$$

As a result, Equation (5.7) can be expressed as

$$\mathbf{F}_a(\mathbf{x}) = \mathbf{a}\mathbf{x}^T \quad (5.10)$$

The geometrical ellipse constraint associated with

$$4a_1a_3 - a_2^2 = 1 \quad (5.11)$$

In order to find the associated coefficients, a least square minimization on N points (x_i, y_i) , $i = 1, \dots, N$ will be carried out. This minimization can be presented by the following equation

$$\mathbf{min} \sum_{i=1}^N F(x_i, y_i)^2 = \mathbf{min} \sum_{i=1}^N (\mathbf{x}_i \mathbf{a})^2 \quad (5.12)$$

Equation (5.12) can be solved directly by the standards least squares method along with the constraint presented by Equation (5.11). The output of this minimization will be the ellipse coefficients presented by Equation (5.7).

The major and minor axes and α can then be derived by the following equations:

$$\alpha = \frac{1}{2} \tan^{-1} \left(\frac{a_2}{a_1 - a_3} \right) \quad (5.13)$$

$$M = -a_6 + \frac{(a_4 \cos \alpha - a_5 \sin \alpha)^2}{4(a_1 \cos^2 \alpha + a_2 \cos \alpha \sin \alpha + a_3 \sin^2 \alpha)} + \frac{(a_5 \cos \alpha - a_4 \sin \alpha)^2}{4(a_1 \sin^2 \alpha - a_2 \cos \alpha \sin \alpha + a_3 \cos^2 \alpha)} \quad (5.14)$$

$$a' = \left(\mathbf{abs} \left(\frac{M}{a_1 \cos^2 \alpha + a_2 \cos \alpha \sin \alpha + a_3 \sin^2 \alpha} \right) \right)^{0.5} \quad (5.15)$$

$$b' = \left(\mathbf{abs} \left(\frac{M}{a_1 \sin^2 \alpha - a_2 \cos \alpha \sin \alpha + a_3 \cos^2 \alpha} \right) \right)^{0.5} \quad (5.16)$$

where M , a' , and b' are dummy variables. The major and minor diameters can then be expressed by

$$A = 2\mathbf{max}(a', b') \quad (5.17)$$

$$B = 2\mathbf{min}(a', b') \quad (5.18)$$

These values are then collected to be used in training of the proposed neural network as will be described below.

5.2.2 Features Selection

The collected data from images should be rich enough to present the dynamic behavior of the system accurately. Moreover, there should be a strong correlation between the selected features and the clad height deviation. On the other hand, the collected data should be fed into a neural network structure whose convergence is a function of the selected features. In order to address the above mentioned issues, 4 features from the projected image are selected: A , B , A' , B' . These parameters, as shown in Figure 5.4, represent the nature of two ellipses fitted into the projected melt pool's images which were grabbed by cameras 1 and 2. These four parameters are strongly correlated with the clad height.

As mentioned in Chapter 3, direction of the tangential path vector, \hat{e}_t , varies by changing the orientation of the clad (see Figure 3.9). Depending on the orientation of the track tangential vector, \hat{e}_t , with respect to the reference line, the size of the projected border varies, and in turn, corresponding elliptical features alter. This unit vector makes a varied angle, θ , with respect to a reference line. This reference line is considered to be the corresponding right hand side camera's axis (the line between the right hand side camera of the unit vector and the center of the workspace). Hence, θ should also be considered as one of the correlated features to the clad height.

Figure 5.5 shows typical projected melt pool's borders at different θ_s (i.e., 0° , 30° , 60°). As seen, θ has a significant impact on the shape of the projected image. As a result, this angle is used as the 5th input for the proposed neural network and angle θ associated with each elapsed time was collected through the trajectories. Selection of these parameters is also based on observation from the melt pool deviations during the actual laser cladding process. Inherent in the selection is the fact that these features are sensitive enough for various clad height range. This arrangement can minimize the computational time which,

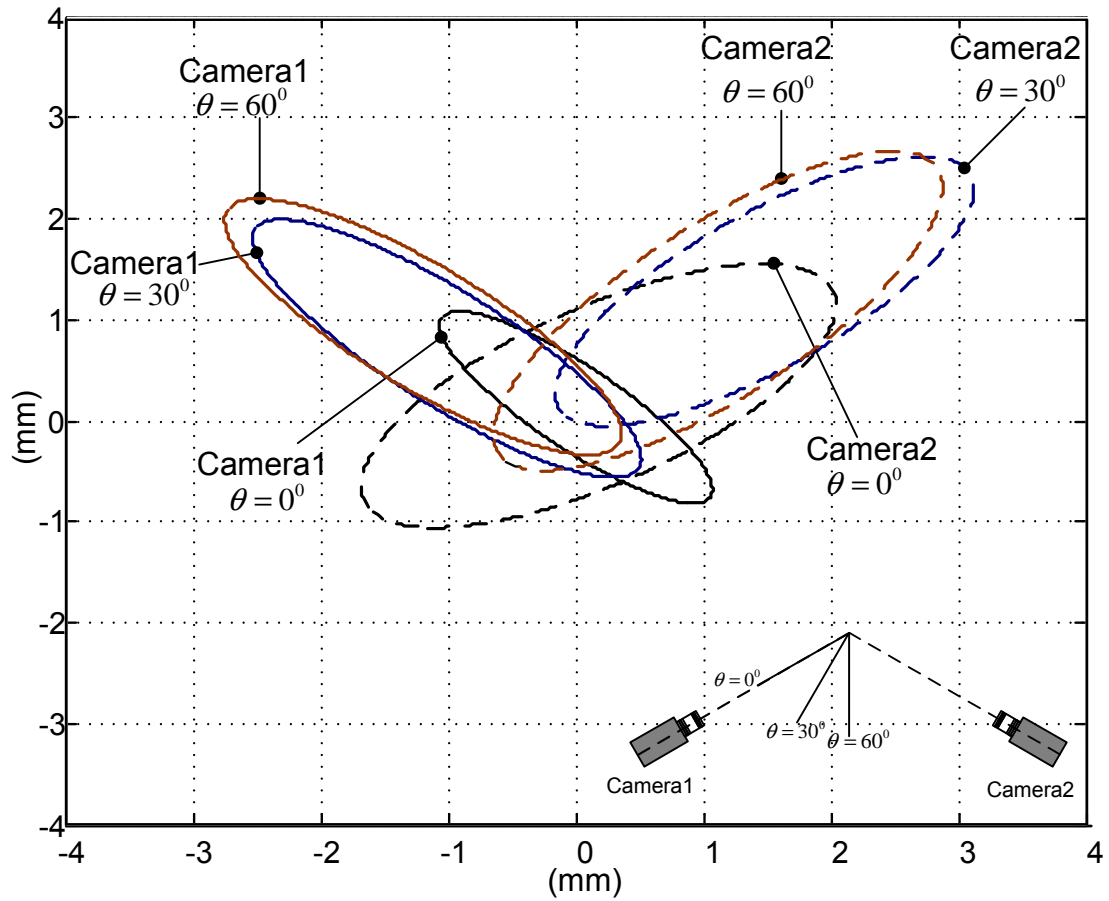


Figure 5.5: Typical projected melt pool borders for different angles of the tangential path vector

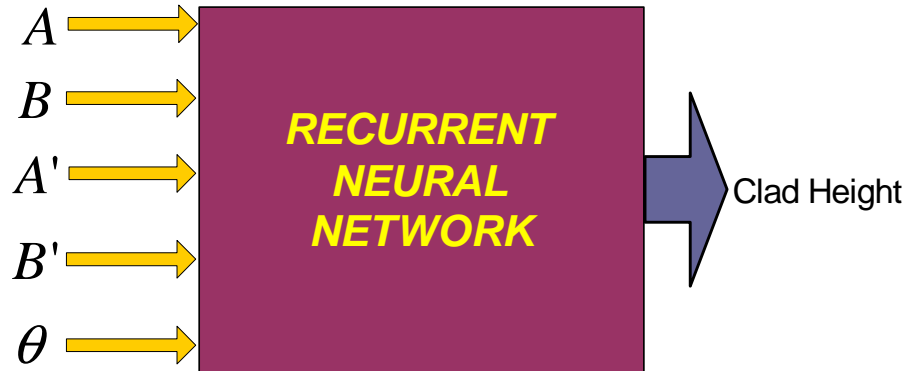


Figure 5.6: Input and the output of the recurrent neural network

in turn, increases the suitability of the algorithm for the prediction of clad height in real-time.

In summary, the selected neural network consists of 5 inputs and one output as shown in Figure 5.6. The actual height measured in off-line is considered as the target for the training of the model.

5.3 Recurrent Neural Network

A recurrent neural network (RNN) is a particular form of neural network model that has a feedback signal in the network architecture. The universal approximation capabilities of the recurrent multilayer perceptron make it a popular choice for modelling nonlinear dynamic systems and implementing general-purpose nonlinear controllers. There are different forms of recurrent neural networks such as Elman and Hopfield networks.

An Elman RNN is considered for this study due to its supervised structure. Elman network, as shown in Figure 5.7, contains of an internal feedback loop, which makes it capable of detecting temporary and sudden patterns in the images [65]. Due to this feature, it can indirectly resolve the influence of noise in the prediction of the clad height. As explained before, the images might be affected by undesired noise generated by plasma formation, flare and reflected light. The dynamic nature of the selected RNN can effectively detect any dynamic disturbances in the network inputs generated by the noise. In fact,

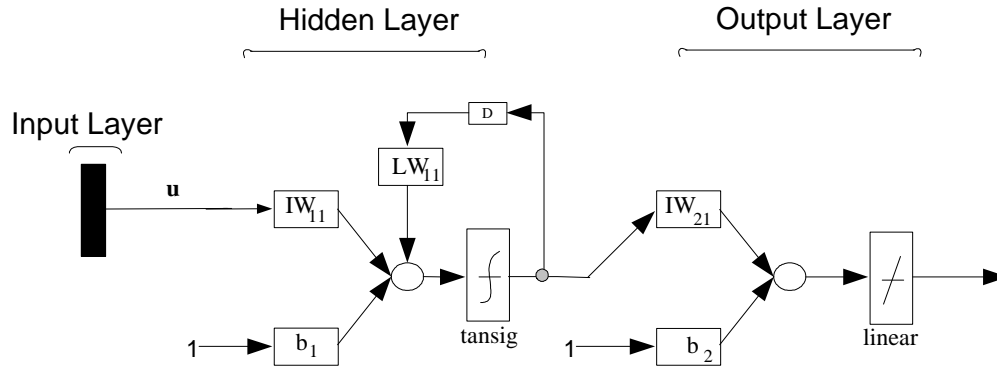


Figure 5.7: Structure of the selected Elman neural network adapted from Neural Network Toolbox of Matlab

any temporary and sudden patterns in the images which are reflected in our inputs can be detected and eliminated in the clad height prediction if the networks well-trained so that it can distinguish these temporary patterns are generated due to undesired noise.

In Figure 5.7, \mathbf{u} and \mathbf{y} are the input and output matrices, respectively, \mathbf{IW} are the network's weights, \mathbf{LW} is the feedback weight, D is the delay and b is the bias matrix. The only requirement is that the hidden layer must have a suitable number of neurons. Although more hidden neurons are needed as the complexity of the function being fit increases, increasing the number of hidden neurons causes noise identification instead of process identification in a noisy environment. In this study trial and error procedure were performed to obtain the RNN proper parameters. As a result, the delay D was selected as 2 samples due to the observed delay between the input signal and the real process response. The number of neurons was 10 and 1 for hidden and output layers, respectively.

5.4 Experimental Verification

To investigate the performance of the aforementioned algorithms, several experiments were conducted using the apparatus shown in Figure 3.10. Two cameras of the proposed trinocular CCD-based optical detectors were installed into the processing head with 120° degrees apart from each other, as explained in Chapter 3. Images of the melt pool were captured

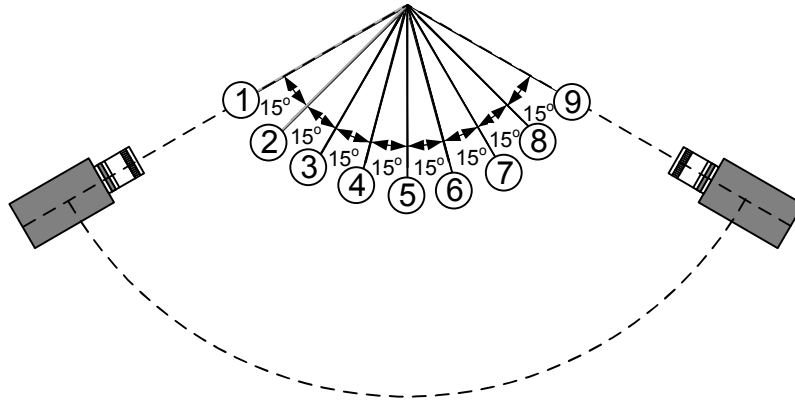


Figure 5.8: Top view of direction of conducted tests for collecting data

by UNIQU UP-600CL digital cameras at a rate of 10Hz on a QNX 6.3 platform (Pentium 4, 2.6 GHz processor). A Band pass filter centered at 700 nm and a number 4 neutral intensity filter were added to each camera. During the course of the experiments, all process parameters except the velocity were kept constant as the laser frequency was set to 90 Hz, laser pulse duration to 3.0 ms , and laser pulse energy to 4 J/pulse. Stainless steel powder (303L) was fed at a rate of 2 g/min through the powder feeder's lateral nozzle on a mild steel substrate. The velocity of the substrate was being changed between 0.5 mm/sec to 3 mm/sec in order to get different clad height. The ground truth comes from the process constraints related to mechanical and metallurgical properties of clad. In fact, the proposed ranges of the process parameters lead to high quality clad in terms of physical properties.

In order to obtain rich data, 9 clad tracks with 15° incremental angle were generated in order to cover 120° degrees between each two cameras as shown in Figure 5.8. Table 5.1 shows the specification of these clad tracks. One of the generated tracks is shown in Figure 5.9. Using the proposed algorithm and procedures, 2284 sets of data were extracted from images. Figure 20 shows deviation of each of four parameters for test 3.

Table 5.1: Specification of the conducted tests

| Test number | θ | Number of frames |
|-------------|-------------|------------------|
| Test 1 | 0° | 180 |
| Test 2 | 15° | 180 |
| Test 3 | 30° | 180 |
| Test 4 | 45° | 180 |
| Test 5 | 60° | 493 |
| Test 6 | 75° | 256 |
| Test 7 | 90° | 270 |
| Test 8 | 105° | 273 |
| Test 9 | 120° | 272 |

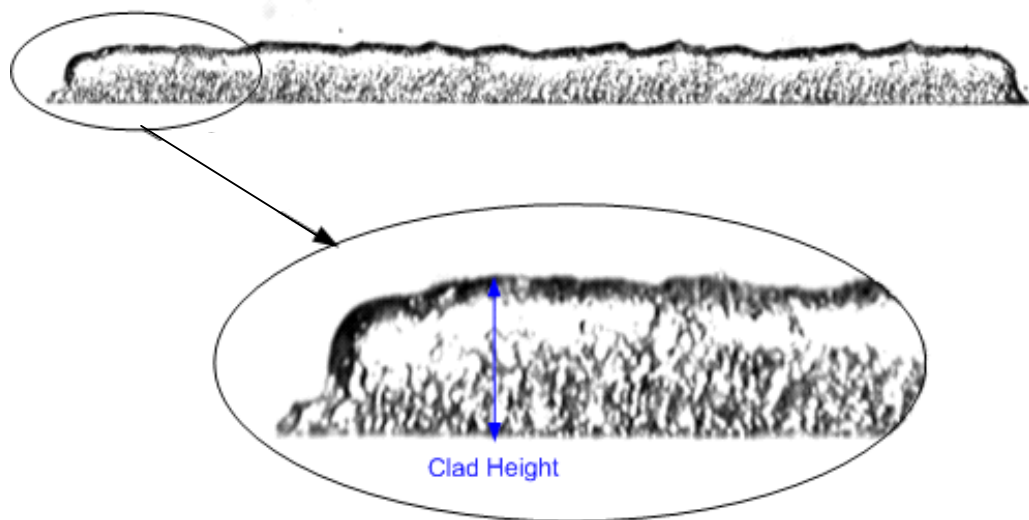


Figure 5.9: Offline picture of the clad track of test 7

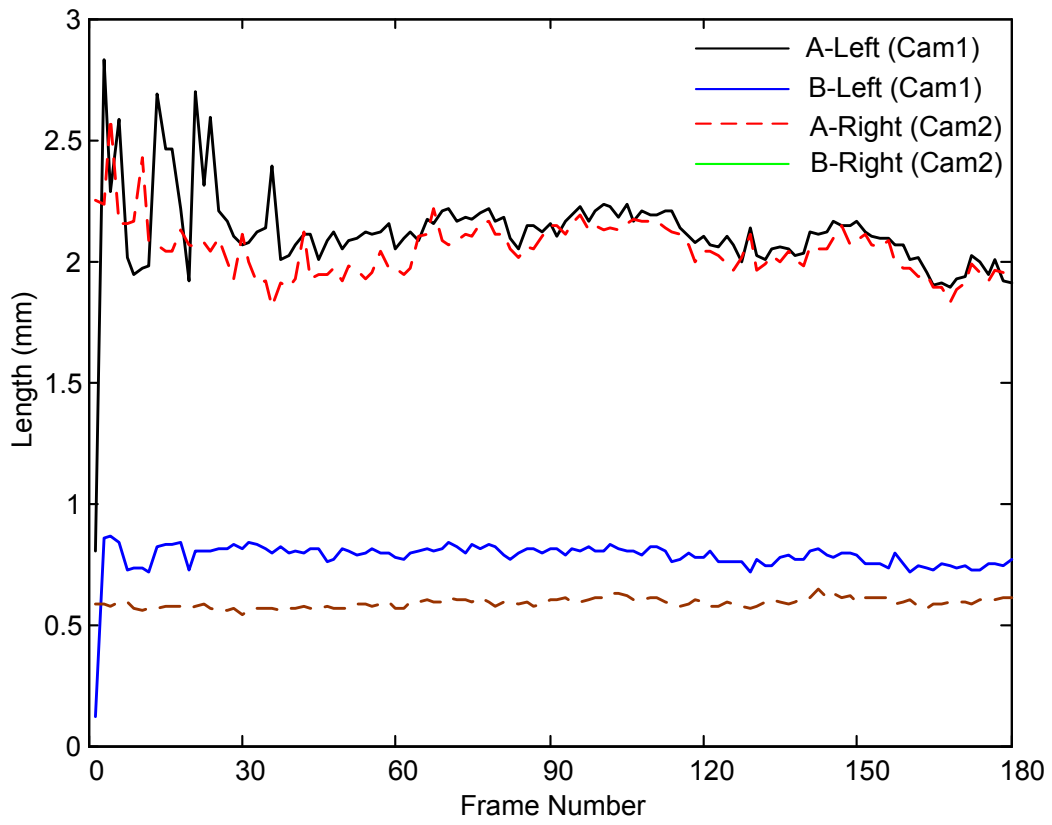


Figure 5.10: Deviation of elliptical features during the test 3

5.4.1 Training and Simulation of RNN

To train the network, backpropagation through the time technique [66, 67] with 2284 sets of extracted data from previous step was used. As mentioned earlier for each test, θ was constant; hence there were 9 various θ among our data sets. For the target, the real height corresponding to each frame was extracted offline. The training was performed and the model converged with the error of less than 0.0001.

5.4.2 Verification of RNN and Discussion

For verification, one clad with the same angle of test 5 generated (i.e., $\theta = 60^\circ$), which was not used in the training. Figure 5.11 shows the comparison between the network and the actual height. As seen in the figure, network can reasonably predict the clad height, in which the precision of data is about ± 0.15 mm translated to an average error of 12%. The figure indicates that the developed algorithm can effectively predict the clad height at various amplitudes and frequencies. The algorithm properly works at a wide range of clad amplitude (i.e., 1 to 2.5 mm). There are several sources of error such as discrepancies between the detected and the actual melt pool image originated from thresholding or light dissipation/reflection, lens distortion, nonlinear effects in projection approach and finally possible shrinkage in the produced clads after being cooled down.

It was evaluated that the developed algorithm is not computationally intensive with the used hardware and software (i.e., IPPL library over the C++ code). Since the rate of simultaneous frame grabbing through the cameras was 10Hz, the required computational time did not alter the above mentioned frequency. This computation timing is an ideal platform for the use of this system for real-time detection of the clad height independent of the path.

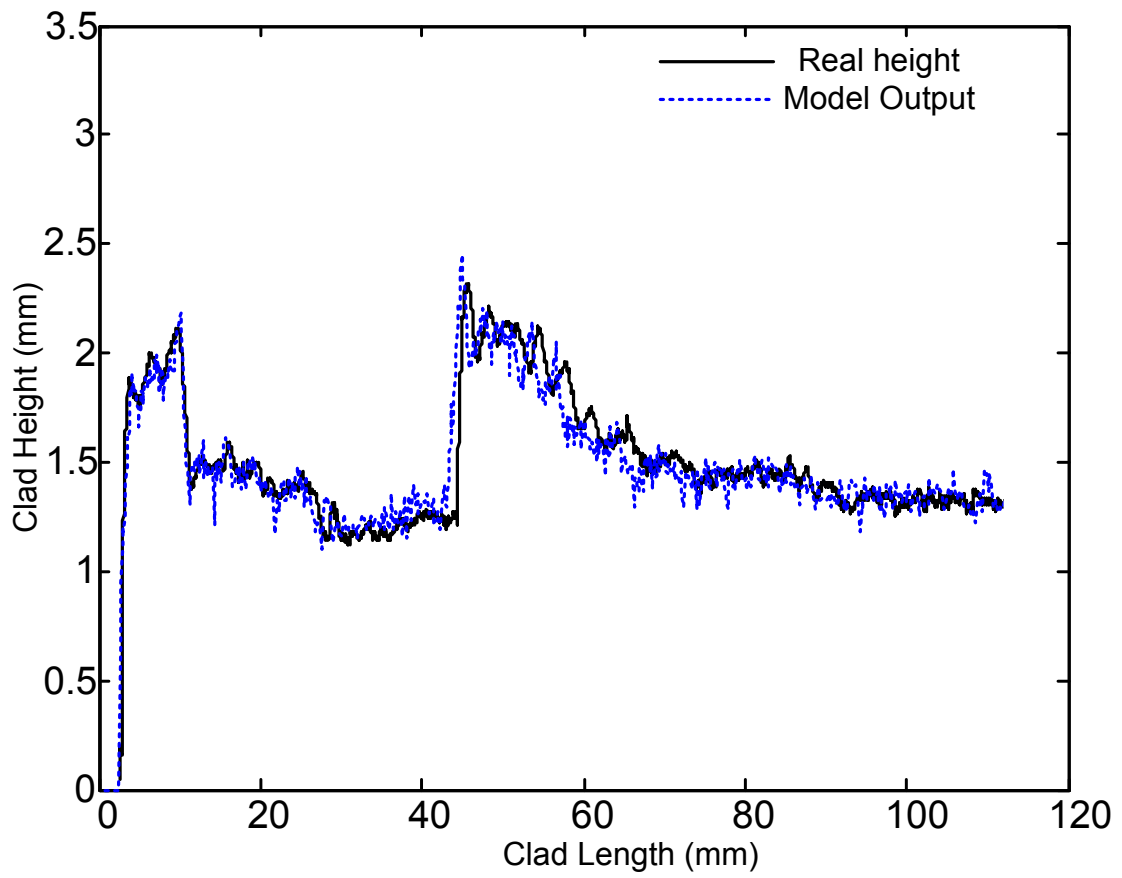


Figure 5.11: Clad height predicted by model versus real height for $\theta = 60^\circ$

Chapter 6

Conclusion and Recommendations

6.1 Conclusion

This thesis presented novel algorithms for real-time detection of clad height in laser cladding. Figure 6.1 illustrates a summary of the developed algorithms in order to measure the clad height in real-time. This was accomplished by the following:

Tackling the issues pertinent to image acquisition in the presence of harsh and intensive light was scrutinized in Chapter 3. Important parameters of digital cameras related to selection of proper type of CCD cameras in order to overcome the existent harsh condition were presented. Also, the existent light in laser cladding arisen from different sources was analyzed and based upon that proper bandpass filters and neutral filters were selected. All these lead to capture relatively sharp and clear images of the melt pool. Capturing good quality pictures potentially would provide valuable information about the process. This information could include, but is not limited to, melt pool geometry (i.e., melt pool height, width, melt pool profile, and wet angle), angle of solidification, melt pool temperature, and melt pool temperature distribution. Furthermore, the issues regarding path dependency of the melt pool image were addressed by using a trinocular cameras configuration. By utilizing this, always two cameras monitor the front end of the melt pool regardless of the direction of the clad.

Image analysis of the grabbed images was discussed in Chapter 4. Image thresholding

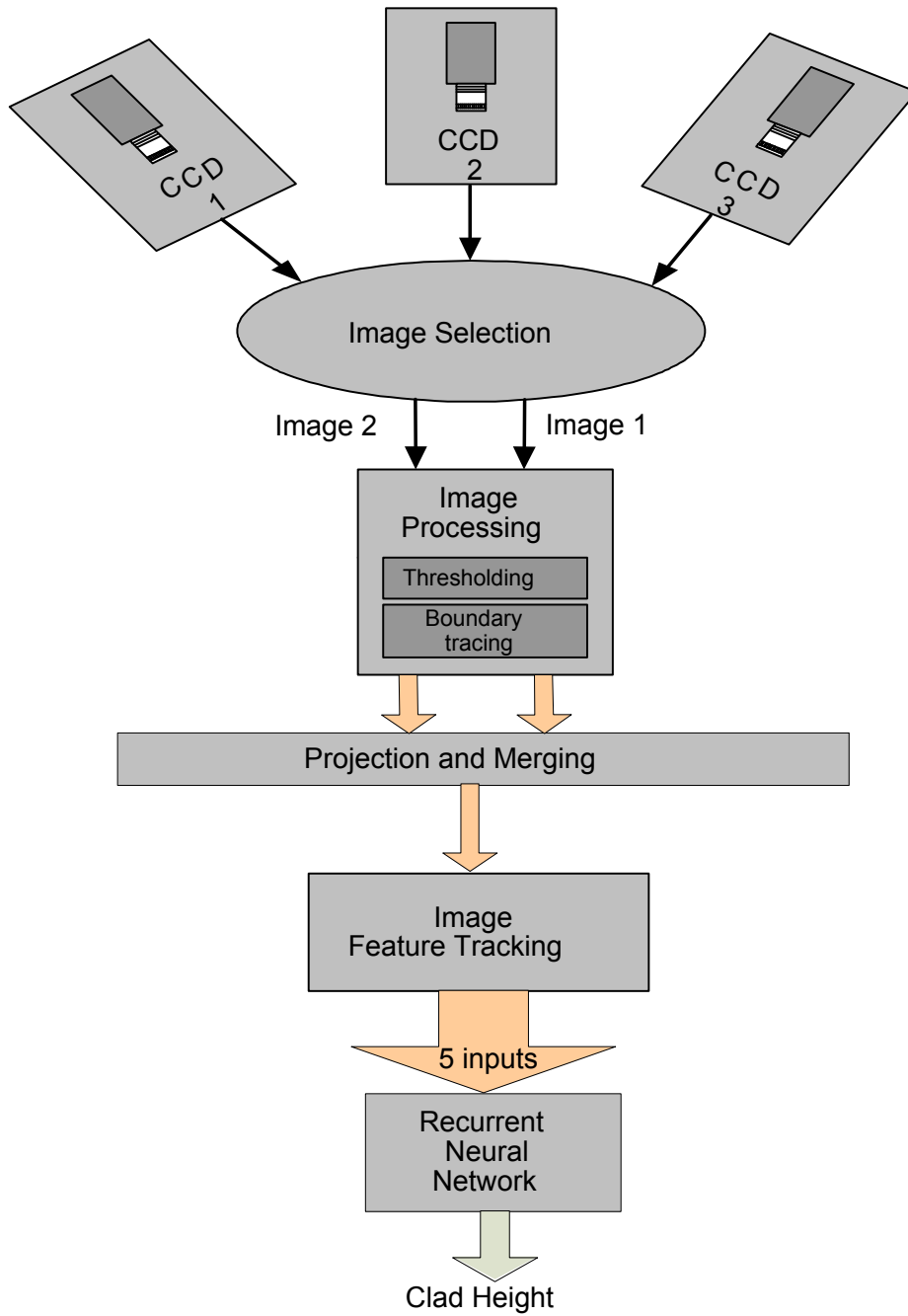


Figure 6.1: A Pattern recognition algorithm

is one of the most formidable tasks in image processing and this difficulty is intensified due to characteristics of the grabbed images of the melt pool (e.g., surrounding hazy area around the melt pool). Applying hard partitioning thresholding methods did not lead to the accurate detection of the melt pool. Therefore, a method based on fuzzy thresholding by minimizing of the measure of fuzziness was developed and its performance was investigated. The effect of three important membership functions, triangular, Gaussian, and generalized Bell on the performance of the thresholding method was investigated. Also, an image thresholding method by utilizing fuzzy c-means clustering was developed. Applying the developed thresholding methods shows promising results. Among the developed thresholding methods, fuzzy thresholding with minimizing the measure of fuzziness with Gaussian membership function was selected for the implementation in the algorithm due to its good results and its fast processing speed.

In Chapter 5, Image feature tracking module was presented. The detected borders of the melt pool images are transformed from image plane to the world plane by using a perspective transformation. Four features of the elliptical features of the projected melt pool borders are selected. These four features along with the angle of tangential path vector with respect to the corresponding right hand side camera's axis are fed into an Elman recurrent neural network. The proposed algorithms and the trained neural network were utilized in the process resulting in acceptable detection of the clad height in deposition of straight clads for a specific direction. It is concluded that the system can detect the clad height with about $\pm 0.15\text{ mm}$ maximum error. The processing speed of the algorithms made them a good platform for the use in the system for real-time detection of clad height.

However, the promising results are limited to the direction of a straight line equidistant to the both camera's axis (i.e., $\theta = 60^\circ$). By moving the direction of the straight line toward each camera's axis the results of the model are downgraded. The average error for direction of each camera's axis (i.e., $\theta = 60^\circ$ or $\theta = 120^\circ$) reaches up to 40 percent. Furthermore, the performance of the model is demoted when the height of clad becomes less than 1 mm. In fact the algorithm does not provide reliable results for the height of less than 0.5 mm.

These increasing errors could arise from many sources such as:

- Image thresholding does not lead to extract the exact melt pool shape in some cases which conduces to some errors.
- The algorithm works based on the measuring of the perimeter of the area which is white in the binary image which is not always representing the existence of clad height, For example when laser just by itself radiates on the substrate, a shiny spot is formed on the substrate which the algorithm considers it as a clad with a small height, however there is no real clad in this case. In other words a threshold value should be considered which beyond that value the output of the algorithm is more reliable and below that less reliable. This conduces to greater error in thin clad compare to thick clad.
- Sometimes the area around the melt pool is being lit due to light dissipation and reflection.
- Algorithm by itself like other algorithms gives some percentage of error.

6.2 Recommendations

It is desired to have a vision system which is independent of the kind of material in laser cladding. However, the current filtering system is dependent upon the black body radiation which may differ drastically from one material to another. In addition, when a mixture of a few kinds of materials is used, determination of the proper set of filtering system is difficult. On the other hand, the performed light analysis in Chapter 3, suffers from many assumptions and estimations which might have resulted in capturing the melt pool improperly. In order to address these issues, use of an illumination light with a specific wavelength along with using the proper bandpass filter in front of the camera is recommended. As a result, light only in the narrow band width of illumination light wavelength can reach the camera, which in turn, leads to disposal of harsh and intensive light in the process. Also, use of non intensified CCD cameras with high quantum efficiency in near infrared region is recommended. This may result in capturing images with higher quality and less noise.

Furthermore, more experiments should be conducted to collect more data to be used in the training of RNN and enhancing the performance of the algorithm for angles other than $\theta = 60^\circ$, and curvature trajectories.

References

- [1] L. Sexton, "Laser cladding: Repairing and manufacturing metal parts and tools," in *Optics and Photonics Technologies and Applications* (T. J. Glynn, ed.), vol. 4876, LaserAge Ltd., 2002.
- [2] E. Toyserkani, A. Khajepour, and S. Corbin, *Laser Cladding*. Boca Raton, Fl. : CRC Press, 2005.
- [3] G. Gnanamuthu, "Surface alloying and transformation haredning using an industrial laser," *JOM*, vol. 27, no. 12, p. A61, 1975.
- [4] F. Seaman, "Using industrial laser to surface harden and alloy," *Metal progress*, vol. 108, no. 3, p. 67, 1975.
- [5] W. M. Steen and C. G. H. Courtney, "Hardfacing of nimonic 75 using 2kw continuous-wave co2 laser," *Metals Technology*, vol. 7, no. pt 6, pp. 232 – 237, 1980.
- [6] V. M. Weerasinghe and W. M. Steen, "Laser cladding with pneumatic powder delivery," in *Lasers in Materials Processing, Conference Proceedings - American Society for Metals.*, (Los Angeles, CA, USA), pp. 166 – 174, 1983.
- [7] R. M. Macintyre, "Laser hard surfacing of gas turbine blade shroud interlocks," in *Proceedings of the 1st International Conference on Lasers in Manufacturing*, (Brighton, East Sussex, Engl), pp. 253 – 261, 1983.
- [8] R. R. Ltd., "Laser application of a hard surface alloy." UK Patent GB 205256A, 1980.

- [9] D. Hu and R. Kovacevic, "Sensing, modeling and control for laser-based additive manufacturing," *International Journal of Machine Tools and Manufacture*, vol. 43, no. 1, pp. 51 – 60, 2003.
- [10] D. Hu, H. Mei, and R. Kovacevic, "Improving solid freeform fabrication by laser-based additive manufacturing," *Proceedings of the Institution of Mechanical Engineers, Part B (Journal of Engineering Manufacture)*, vol. 216, no. 9, pp. 1253 – 64, 2002.
- [11] F. Meriaudeau, F. Truchetet, D. Aluze, and C. Dumont, "Machine vision system applied to the characterization of a powder stream: Application to the laser cladding process," *Proceedings of SPIE - The International Society for Optical Engineering*, vol. 3306, pp. 22 – 31, 1998.
- [12] F. Meriaudeau, D. Aluze, C. Dumont, P. Geveaux, and F. Truchetet, "Artificial vision applied to laser cladding process: particle speed measurements," *QCAV 97. 1997 International Conference on Quality Control by Artificial Vision*, pp. 330 – 5, 1997.
- [13] F. Meriaudeau, C. Dumont, D. Aluze, and F. Truchetet, "Investigations of the particles speed using image processing for the laser cladding process," *Proceedings of the SPIE - The International Society for Optical Engineering*, vol. 3101, pp. 211 – 20, 1997.
- [14] F. Meriaudeau and F. Truchetet, "Control and optimization of the laser cladding process using matrix cameras and image processing," *Journal of Laser Applications*, vol. 8, no. 6, pp. 317 – 324, 1996.
- [15] F. Meriaudeau, F. Truchetet, D. Aluze, S. Bouchard, H. Andrezejewski, and C. Dumont, "Toward a real time control of the laser cladding process through an artificial vision system," *30th International Symposium on Automotive Technology and Automation. Robotics, Motion and Machine Vision in the Automotive Industries*, pp. 339 – 46, 1997.
- [16] M. Doubenskaia, P. Bertrand, and I. Smurov, "Optical monitoring of nd:yag laser cladding," *Thin Solid Films*, vol. 453-454, pp. 477 – 85, 2004.

- [17] M. Doubenskaia, P. Bertrand, and I. Smurov, "Temperature monitoring of nd:yag laser cladding (cw and pp) by advanced pyrometry and ccd-camera-based diagnostic tool," *Proceedings of the SPIE - The International Society for Optical Engineering*, vol. 5399, no. 1, pp. 212 – 19, 2004.
- [18] P. Bertrand, M. Doubenskaia, M. Ignatiev, I. Smurov, F. Campana, J. Janssen, and B. Laget, "Optical diagnostics in thermal spraying and laser cladding," *Proceedings of the International Conference on Advances in Surface Treatment: Research and Applications, ASTRA*, vol. 2004, pp. 527 – 536, 2004.
- [19] M. Doubenskaia, P. Bertrand, and I. Smurov, "Pyrometry in laser surface treatment," *Surface and Coatings Technology*, vol. 201, no. 5, pp. 1955 – 1961, 2006.
- [20] F. Meriaudeau, F. Truchetet, C. Dumont, E. Renier, and P. Bolland, "Acquisition and image processing system able to optimize laser cladding process," *ICSP '96. 1996 3rd International Conference on Signal Processing Proceedings*, vol. vol.2, pp. 1628 – 31, 1996.
- [21] F. Meriaudeau, E. Renier, and F. Truchetet, "Ccd technology applied to laser cladding," *Proceedings of the SPIE - The International Society for Optical Engineering*, vol. 2654, pp. 299 – 309, 1996.
- [22] F. Meriaudeau, F. Truchetet, D. Grevey, and A. Vannes, "Laser cladding process and image processing," *Lasers in Engineering*, vol. 6, no. 3, pp. 161 – 187, 1997.
- [23] F. Meriaudeau, E. Renier, and F. Truchetet, "Temperature imaging and image processing in the steel industry," *Optical Engineering*, vol. 35, pp. 3470 – 81, December 1996.
- [24] A. Legrand, P. Suzeau, E. Renier, F. Truchetet, P. Gorria, and F. Meriaudeau, "Machine vision systems in the metallurgy industry," *Journal of Electronic Imaging*, vol. 10, no. 1, pp. 274 – 82, 2001.
- [25] D. Hu and R. Kovacevic, "Modelling and measuring the thermal behaviour of the molten pool in closed-loop controlled laser-based additive manufacturing," *Proceedings*

- of the Institution of Mechanical Engineers, Part B (Journal of Engineering Manufacture)*, vol. 217, no. B4, pp. 441 – 52, 2003.
- [26] D. Hu, M. Labudovic, and R. Kovacevic, “On-line sensing and estimation of laser surface modification by computer vision,” *Proceedings of the Institution of Mechanical Engineers, Part B (Journal of Engineering Manufacture)*, vol. 215, no. B8, pp. 1081 – 90, 2001.
- [27] D. Hu, Y. Wu, and R. Kovacevic, “Heat input control in 3d laser cladding based on infrared sensing,” *American Society of Mechanical Engineers, Manufacturing Engineering Division, MED*, vol. 12, pp. 333 – 341, 2001. Laser cladding;.
- [28] D. Hu, R. Kovacevic, and M. Valant, “Solid freeform fabrication of metal parts by 3d laser cladding,” *American Society of Mechanical Engineers, Manufacturing Engineering Division, MED*, vol. 11, pp. 365 – 371, 2000.
- [29] J. Fraden, *Handbook of Modern Sensors: Physics, Designs, and Applications*. American Institute of Physics, second ed., 1997.
- [30] W. Pastorius, “Triangulation sensors an overview,” tech. rep., Laser Measurement International Inc. (LMI).
- [31] J. Beersiek, “A cmos camera as a tool for process analysis not only for laser beam welding,” *20th International Congress on ICALEO 2001. Applications of Lasers and Electro-Optics. Congress Proceedings. Laser Materials Processing Conference. Laser Microfabrication Conference*, pp. 1185 – 93, 2001.
- [32] J. Beersiek, “On-line monitoring of keyhole instabilities during laser beam welding,” *Proceedings of the Laser Materials Processing Conference. ICALEO’99. LIA Vol. 87*, vol. vol.2, pp. 49 – 58, 2000.
- [33] J. Beersiek, “New aspects of monitoring with a cmos camera for laser materials processing,” *ICALEO 2002. 21st International Congress on Applications of Lasers and Electro-Optics*, vol. Vol.2, pp. 1181 – 90, 2002.

- [34] J. Beersiek, R. Poprawe, W. Schulz, H. Gu, R. Mueller, and W. Duley, "On-line monitoring of penetration depth in laser beam welding," *Laser Institute of America, Proceedings*, vol. 83, no. Pt 1, pp. 30–39, 1997.
- [35] H. Gu and W. Duley, "Acoustic emission from modulated laser beam welding of materials," *Journal of Laser Applications*, vol. 8, no. 4, pp. 205 – 210, 1996.
- [36] H. Gu, R. Mueller, and W. Duley, "Acoustic monitoring of modulated laser beam processing of metals," *Proceedings of the SPIE - The International Society for Optical Engineering*, vol. 2703, pp. 80 – 90, 1996.
- [37] H. Gu and W. Duley, "Statistical approach to acoustic monitoring of laser welding," *Journal of Physics D: Applied Physics*, vol. 29, no. 3, pp. 556 – 560, 1996.
- [38] H. Gu and W. Duley, "Resonant acoustic emission during laser welding of metals," *Journal of Physics D: Applied Physics*, vol. 29, no. 3, pp. 550 – 555, 1996.
- [39] D. Maischner, A. Drenker, B. Seidel, P. Abels, and E. Beyer, "Process control during laser beam welding," *LIA (Laser Institute of America)*, vol. 74, pp. 150 – 155, 1992.
- [40] H. Haferkamp, F. von Alvensleben, D. Seebaum, and O. Thuerk, "Visualization of dynamic melting pool behavior," *Laser Institute of America, Proceedings*, vol. 83, no. 2, pp. 55–64, 1997.
- [41] H. Haferkamp, J. Gerken, D. Stegemann, and C. Reichert, "In-situ untersuchung des harestofftransportes beim laserstrahl-dispergieren mittels hochgeschwindigkeits-radioskopie," *Metal*, vol. 3, pp. 185–191, 1996.
- [42] D. Voelkel and J. Mazumder, "Visualization of a laser melt pool," *Applied Optics*, vol. 29, no. 12, pp. 1718 – 22, 1990.
- [43] D. Voelkel and J. Mazumder, "Visualization and dimensional measurement of the laser weld pool," *Proceedings of the Laser Materials Processing - ICALEO*, vol. 71, pp. 422 – 429, 1991.

- [44] “available [online] <http://www.photomet.com/>.”
- [45] “available [online] <http://www.andor.com/library/>.”
- [46] M. Asselin, “Optical sensor for real-time measurement of clad height during laser cladding process,” Master’s thesis, University of Waterloo, 2006.
- [47] E. Toyserkani, A. Khajepour, and S. F. Corbin, “System and method for intelligent closed-loop control of laser cladding by powder injection.” US patent number 7043330, May 2006.
- [48] C. Jawahar, P. Biswas, and A. Ray, “Investigations on fuzzy thresholding based on fuzzy clustering,” *Pattern Recognition*, vol. 30, no. 10, pp. 1605 – 1613, 1997.
- [49] C. Jawahar, P. Biswas, and A. Ray, “Analysis of fuzzy thresholding schemes,” *Pattern Recognition*, vol. 33, no. 8, pp. 1339 – 49, 2000.
- [50] M. Sezgin and B. Sankur, “Survey over image thresholding techniques and quantitative performance evaluation,” *Journal of Electronic Imaging*, vol. 13, no. 1, pp. 146 – 168, 2004.
- [51] J. Weszka, “A survey of threshold selection techniques,” *Computer Graphics and Image Processing*, vol. 7, no. 2, pp. 259 – 65, 1978.
- [52] P. Sahoo, S. Soltani, A. Wong, and Y. Chen, “A survey of thresholding techniques,” *Computer Vision, Graphics, & Image Processing*, vol. 41, no. 2, pp. 233 – 260, 1988.
- [53] N. R. Pal and D. Bhandari, “Image thresholding: Some new techniques,” *Signal Processing*, vol. 33, no. 2, pp. 139 – 158, 1993.
- [54] N. Pal and S. Pal, “A review on image segmentation techniques,” *Pattern Recognition*, vol. 26, no. 9, pp. 1277 – 94, 1993.
- [55] R. Haralick and L. Shapiro, “Image segmentation techniques,” *Computer Vision, Graphics, and Image Processing*, vol. 29, no. 1, pp. 100 – 32, 1985.

- [56] N. Otsu, "A threshold selection method from gray-level histograms," *IEEE Transactions on Systems, Man and Cybernetics*, vol. SMC-9, no. 1, pp. 62 – 6, 1979.
- [57] L.-K. Huang and M.-J. J. Wang, "Image thresholding by minimizing the measures of fuzziness," *Pattern Recognition*, vol. 28, no. 1, pp. 41 – 51, 1995.
- [58] A. Deluca and S. Termini, "A definition of a non-probabilistic entropy in the setting of fuzzy sets," *Int. Control*, vol. 20, pp. 301–312, 1972.
- [59] A. R. Webb, *Statistical Pattern Recognition*. Wiley, 2nd ed., 2002.
- [60] W. Pedrycz, *Knowledge-based clustering : from data to information granules*. Hoboken, N.J. : John Wiley, 2005.
- [61] R. I. Hartley and A. Zisserman, *Multiple View Geometry in Computer Vision*. Cambridge University Press, ISBN: 0521540518, second ed., 2004.
- [62] O. Faugeras and T. Luong, Quang-Tuan with contributions from Papadopoulo, *The Geometry of Multiple Images: The Laws that Govern the Formation of Multiple Images of a Scene and Some of Their Applications*. The MIT Press, Cambridge, 2001.
- [63] E. Toyserkani, A. Khajepour, and M. Khadem Sameni, "Development of trinocular optical ccd-based detectors for real-time measurement of clad geometry," *Proceeding of International Congress on the Applications of Lasers and Electro-Optics*, pp. 93–100, 2004.
- [64] R. Halir and J. Flusser, "Numerically stable direct least squares fitting of ellipses," *WSCG'98. The Sixth International Conference in Central Europe on Computer Graphics and Visualization*, vol. vol.1, pp. 125 – 32, 1998.
- [65] J. Elman, "Finding structure in time," *Cognitive Science*, vol. 14, no. 2, pp. 179 – 211, 1990.
- [66] J. Principe, N. Euliano, and W. Lefebvre, *Neural and adaptive systems: fundamentals through simulations*. Wiley, New York, 2000.

- [67] O. Nerrand, P. Roussel-Ragot, D. Urbani, L. Personnaz, and G. Dreyfus, “Training recurrent neural networks: why and how? an illustration in dynamical process modeling,” *IEEE Transactions on Neural Networks*, vol. 5, no. 2, pp. 178 – 184, 1994.